

THESIS

NEOTECTONIC EFFECTS OF GLACIAL EROSION AND DEGLACIATION ON  
THE SANGRE DE CRISTO MOUNTAINS, SOUTHERN COLORADO

Submitted by

Cecilia Hurtado

Department of Geosciences

In partial fulfillment of the requirements

For the Degree of Master of Science

Colorado State University

Fort Collins, Colorado

Fall 2023

Master's Committee:

Advisor: Sean Gallen

John Singleton  
Daniel McGrath  
Scott Denning

Copyright by Cecilia Hurtado 2023

All Rights Reserved

## ABSTRACT

### NEOTECTONIC EFFECTS OF GLACIAL EROSION AND DEGLACIATION ON THE SANGRE DE CRISTO MOUNTAINS, SOUTHERN COLORADO

Interrelations between climate and tectonics are important to the development of active mountain belts, but rarely are there natural examples that lend themselves to studying the effects of climate on tectonics. The Sangre de Cristo Mountains in southern Colorado provide an optimal natural laboratory to explore the effects of alpine valley glaciation on surface uplift of the footwall and on the active extensional normal fault system in the northern Rio Grande rift. This region has experienced changes in surface loads associated with long-term glacial erosion and sedimentation over the course of the Quaternary, as well as shorter-term deglaciation after the Last Glacial Maximum. These changing loads correspond with stress changes that affect the flexural isostatic response of the lithosphere, and further act as clamping or unclamping stresses on the Sangre de Cristo fault that bounds the western margin of the mountain range. This work quantifies the masses and spatial distributions of these various loads and models the associated flexural isostatic response to estimate potential uplift and subsidence patterns in the study area that could be attributed to climate-driven mechanisms. The glacially-scoured footwall material was estimated by using remnants of the fluvial reaches downstream of glaciated drainage basins, reconstructing the paleofluvial topography, and subtracting it from the modern topography. The quantification of the deposited sediment in the San Luis Basin was measured from an interpolated surface tethered by existing drill cores, geophysical data, and geologic maps. Lastly, the glacial extents and thicknesses were constructed using a simple numerical modeling tool,

GlaRe, constrained by preserved depositional and erosional evidence of glaciers. Isostatic responses were calculated using a flexure model with two effective elastic thickness ( $T_e$ ) values, 2 km and 5 km, and stress changes on faults at depth were calculated using an analytical line load model. The results estimate ~29 m of footwall uplift and ~47 m of subsidence in the hanging wall for a realistic  $T_e$  of 5 km, and footwall uplift of ~48 m and a hanging wall subsidence of ~80 m for an independently calibrated  $T_e$  of 2 km. Importantly, while topographic reconstructions indicate an ~50 m reduction in mean footwall elevations, isostatic rebound pushes mountain peaks upward by tens of meters. Footwall uplift due to deglaciation has a response of 4 m and 6 m, for a  $T_e$  of 5 km and a  $T_e$  of 2 km, respectively. The Sangre de Cristo fault trace was mapped to quantify the offset of fault scarps on Quaternary alluvial fans to determine the spatial and temporal patterns of offset along-strike of the fault. Fault offset magnitudes correlate with glacial domains, and fault slip rates correlate with the post-glacial spatial pattern of isostatic uplift, indicating an unambiguous link between deglaciation and elevated fault activity. This work demonstrates that (1) differential glacial erosion reduces mean footwall elevations, but the associated isostatic response drives surface uplift of mountain peaks, and (2) seismicity along normal faults could be amplified by load changes associated with climate-driven mechanisms, which will become increasingly important as we continue in a period of anthropogenic warming and deglaciation.

## ACKNOWLEDGEMENTS

I would like to thank Warner College and my two extra-departmental funding sources: the Four Corners Geological Society and the Geological Society of America for their belief in this project and financial support to complete this work. My deepest thanks to my advisor, Sean Gallen, whose patience, levity, and encouragement allowed me to produce work I did not think myself capable of doing. I am immensely thankful to my committee members: John Singleton, whose enthusiasm and joy in the field or on the scope is a constant reminder of how lucky we are to study geoscience; Dan McGrath, whose classes and projects governed much of the work in this thesis; and Scott Denning, whose infectious verve for earth and atmospheric science launched a newfound sense of purpose in myself and what I want to pursue in my career.

This research additionally owes success to Maddie Schwarz, for collaborating on various mapping techniques and attribution systems, as well as Sam Johnstone, Jessica Thompson-Jobe, and Nadine Reitman at the USGS, all of whom gave invaluable advice and asked integral questions that moved this project in the right direction.

Thank you to Sammy Malavarca, Emily Perman, and Shea Slonkosky for being excellent companions both in and out of the field. Thanks to the Geoscience department at CSU, especially the cohort of graduate students I overlapped with – I've learned so much from my peers and have loved being part of such a supportive and active group of graduate students.

# TABLE OF CONTENTS

ABSTRACT.....	ii
ACKNOWLEDGEMENTS.....	iv
<b>1. Introduction</b> .....	<b>1</b>
2.1 <i>Ancestral Rocky Mountains and Laramide Orogeny</i> .....	8
2.2 <i>Magmatism and Rio Grande rift</i> .....	9
2.3 <i>Glacial history</i> .....	15
2.4 <i>Loads, stress, and flexural isostasy</i> .....	17
<b>3. Methods</b> .....	<b>20</b>
3.1 <i>Overview</i> .....	20
3.2 <i>Glacial reconstruction</i> .....	21
3.3 <i>Quantifying eroded material</i> .....	23
3.4 <i>Estimating deposition in the basin</i> .....	31
3.5 <i>Flexural isostasy modeling</i> .....	32
3.6 <i>Fault stress modeling</i> .....	36
3.7 <i>Surface uplift</i> .....	37
3.8 <i>Fault scarp mapping and offset quantification</i> .....	38
<b>4. Results</b> .....	<b>43</b>
4.1 <i>Glacial reconstruction</i> .....	43
4.2 <i>Erosional reconstructions</i> .....	45
4.3 <i>Deposition interpolation</i> .....	45
4.4 <i>Isostasy model</i> .....	48
4.5 <i>Stress modeling</i> .....	51
4.6 <i>Surface uplift</i> .....	53
4.7 <i>Mapping, scarp offset, and timing</i> .....	53
<b>5. Discussion</b> .....	<b>55</b>
5.1 <i>Glacial reconstruction</i> .....	55
5.2 <i>Isostatic response and surface uplift</i> .....	59
5.3 <i>Slip signal of isostatic response to loading and unloading</i> .....	61
5.4 <i>Glaciers and fault offset – chicken or egg?</i> .....	65
5.5 <i>Study implications</i> .....	66

<i>5.6 Future work</i> .....	67
<b>6. Conclusions</b> .....	68
<b>References</b> .....	70
Appendix A: Supplementary Figures.....	80

## 1. Introduction

The impact of climate on mountain development is undeniable in glaciated settings; however, despite decades of research, how climate affects mountain building and tectonic activity remains a central question in tectonic geomorphology studies. Normal fault-bound mountain ranges affected by Quaternary alpine glaciation can provide a useful natural experiment to assess the impact of climate-modulated glacial erosion and ice loading/unloading on the development of mountains and activity of range bounding-faults. Differential erosion of formerly fluviially dominated valleys by alpine glaciers is hypothesized to reduce mean elevations but drive the uplift of mountain peaks due to isostatic rebound (e.g., Molnar and England, 1990; Stern et al., 2005; Champagnac et al., 2007; and Paxman et al., 2016). When considering the cause or timing of seismic slip in a geologic setting, researchers often attribute tectonic slip to changes in stress regimes, fault propagation, or interactivity or linkage of faults (Hampel et al., 2007). It is less common to consider climate change as a potential catalyst or stimulant for seismicity.

Climate can largely affect the landscape by influencing rates and patterns of erosion (and consequently altering uplift rates via isostasy) and sedimentation, and additionally load or unload mass at the Earth's surface in the form of ice sheets, glaciers, and lakes (Hampel et al., 2007). These loads all affect the spatial and temporal distribution of mass at the Earth's surface, impacting the isostatic equilibrium and the state of lithospheric stress. The Earth's surface compensates for these load changes through the flexure of the Earth's lithosphere in response to isostatically compensated loading or unloading, and along planes of weakness (i.e., faults). These load changes can result in a pronounced shift in slip rate and/or magnitude by altering the local stress state of a fault (Calais et al., 2010; Vernant et al., 2013).

Stresses in both vertical and horizontal directions are affected by this mass redistribution: loading/unloading alters the vertical stress, while the lithospheric flexure and rebound modify the horizontal stress (Hampel and Hetzel, 2006). These changes in both horizontal and vertical stress at the local and regional scale can change stress on a fault system and, therefore, might affect rates and patterns of seismic slip. Part of the reason these effects are not typically considered is the lack of high-quality, natural examples that can be drawn upon to test the possibility of the change in climate on fault activity and perhaps an implicit assumption that any climatic influence on seismicity would be negligible.

Researchers have studied the effect of climate on tectonics along the northeastern Basin and Range extensional system after the Last Glacial Maximum (LGM). Hetzel and Hampel (2005) first identified a potential link between the post-LGM shrinkage of Lake Bonneville, a paleolake in northwestern Utah, and increased seismic activity with their investigation of the Wasatch fault proximal to the lake. Using finite-element modeling to simulate slip on a normal fault in response to lithospheric loading and unloading, it was found that when the model did not incorporate isostatic flexure, postglacial unloading could not resolve an increased fault slip rate. However, when isostatic flexure was incorporated, modeled slip rate increased due to isostatic rebound outpacing any effect solely attributed to unloading (Hetzel and Hampel, 2005). These authors demonstrated that loading of the lithosphere could affect the accumulation of stress on a normal fault, and the resulting activity due to these changes can have a lag time on the order of thousands of years. Further, when comparing the model results to the published slip history of the fault, they could attribute the observed increase in Holocene slip rate to the isostatic rebound resulting from the dissipation of Lake Bonneville (Hetzel and Hampel, 2005).

Additional research has also been centered on quantifying isostatic rebound attributed to

differential erosion due to glaciation within a mountain range. Molnar and England (1990) hypothesized that in mountainous areas that have undergone extensive erosion, the mean elevation of the mountain range should be lower than pre-glaciated mean elevation, and that summit elevations would be higher than the pre-glaciated landscape due to isostatic rebound from the unloading of the eroded material. Summit uplift is enhanced for two reasons. First, summits largely reside along drainage divides that are largely spared from the vast amounts of erosion localized in valleys as a mountain landscape transitions from fluvially dominated to one heavily impacted by alpine glaciers (Pederson and Egholm, 2013). Second, the large quantities of valley erosion facilitate an isostatic response, propelling little- or un-eroded portions of the landscape upward. Molnar and England (1990) further argued that there is the potential for positive feedback with erosion produced by alpine valley glaciers and rising peak and divide elevations in that the isostatic uplift due to erosion could raise elevations further above the equilibrium line altitude (ELA). This process would facilitate continued growth of the glaciers, increasing their erosive power and further increasing the elevation due to isostatic rebound (Molnar and England, 1990).

Small and Anderson (1998) advanced these ideas with their work on summit flats in the Rocky Mountains by quantifying geophysical relief, rock uplift, and summit erosion. They found that within Laramide mountain ranges, surface uplift attributed to the isostatic response to erosion is between 50 and 100 m. Recent work in the Alps from Mey et al. (2016) demonstrates that up to 90% of rock uplift in the mountain range can be attributed to the isostatic rebound from LGM alpine ice cap deglaciation. Although most uplift in the Alps is typically attributed to a synthesis of orogenic shortening, delamination at depth, and both erosional and glacial unloading, the viscoelastic rebound signal reproduced a significant amount of the uplift in their

numerical isostasy model (Mey et al., 2016).

Southern Colorado's Sangre de Cristo Mountains provide an ideal location to study the impact of differential alpine glacial erosion and ice (un)loading on topographic development and fault slip. This mountain range is bounded by an active normal fault that has allowed uplift of the mountainous footwall block. The landscape preserves evidence of Quaternary glaciation in the form of small alpine valley glaciers that allow us to reconstruct the paleoglacial ice volumes. Additionally, preserved fluvial remnants in the footwall downstream of formerly glaciated valleys enable us to reconstruct the paleotopography prior to glaciation throughout much of the footwall.

The northern Sangre de Cristo Mountains form a pronounced NNW-SSE-trending linear range with three distinct sections: the northern section (~25 km), the central (Crestone) section (~60 km), and the southern Blanca Massif section (~30 km) (Figure 1). The range is notable for its relatively narrow (~15 km) width, significant relief (~2 km) (Figure S1), and the active, west-dipping, Sangre de Cristo normal fault on its western margin. This fault structurally divides the mountainous eastern footwall from the western adjacent San Luis sedimentary basin on its hanging wall. The focus of this study centers on the northern segment of this mountain range and the corresponding fault system, which begins just south of Poncha Pass and ends at the Blanca Massif, a prominent structure that demarcates the southernmost end of the study area.

The Sangre de Cristo Mountain record evidence of glaciation during the LGM, and ruptures along the fault coincide with the timeline of deglaciation (McCalpin, 1982). Within the field of tectonic geomorphology, there are a number of examples where tectonics has affected climate at various scales (Zhisheng et al., 2001; Sepulchre et al.,

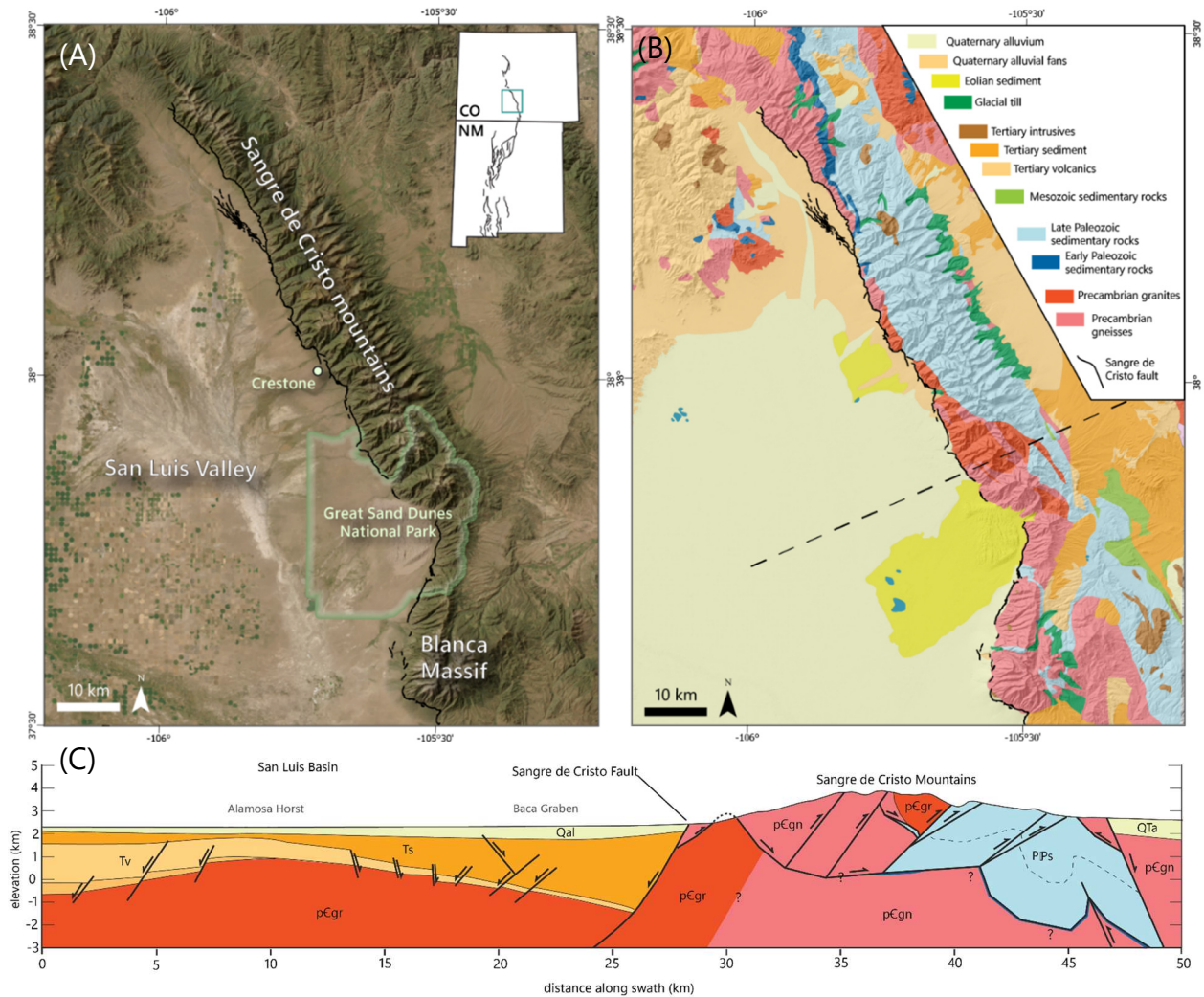


Figure 1. (A) Overview map of the Sangre de Cristo and San Luis Valley study area with hillshade and TerraColor satellite imagery. Index map shows study area outlined in blue with larger Rio Grande rift structures illustrated through Colorado and New Mexico. (B) Simplified geologic map modified from Lindsey (2010). (C) Cross-section modified from Lindsey (2010) and Brister and Gries (1994).

2006; Strecker et al., 2007; Caves et al., 2014; Tada et al., 2016), but it is difficult to find a compelling natural example of where climate has influenced tectonic activity (e.g., Willett, 1999; Whipple, 2009). Due to the proximity of the active Sangre de Cristo normal fault to alpine valley glaciers that occupied the uplifting footwall during the LGM, the Sangre de Cristo Mountains provide the ideal area to study this interaction and determine the extent to which deglaciation and glacial erosion affect fault activity. Because the Sangre de Cristo fault is a normal fault with the

principal stress,  $\sigma_1$ , oriented vertically, it is especially prone to activation or movement due to these changes in stress.

This study hypothesizes that Quaternary alpine glaciation has affected the evolution of the Sangre de Cristo footwall and range bounding normal faults by augmenting surface loads on two different timescales. On  $10^5$ – $10^6$  yr timescales, differential glacial erosion of formerly fluvial-dominant valleys in the footwall and associated sedimentation in the hanging wall is hypothesized to have lowered mean elevations while driving isostatic rise of footwall mountain peaks, while also facilitating long-term fault unclamping. On  $10^3$ – $10^4$  yr timescales, it is hypothesized that deglaciation unloaded the footwall driving small amounts of isostatic uplift but resulting in a significant reduction in fault clamping stress, perhaps facilitating enhanced post-glacial fault slip rates (Figure 2).

To test these hypotheses, I focus on quantifying the mass of material glacially eroded from the footwall, the ice mass lost to deglaciation, the mass of sediment deposited in the San Luis Basin since glaciation, and post-glacial slip magnitudes along the fault to compare the relative patterns of changes in loading from ice and sediment to cumulative post-glacial fault slip. First, I estimate the various erosional, depositional, and glacial loads that act on the system. I then input these loads into a flexural isostatic model to estimate the anticipated magnitudes of deflection due to each load across the fault. I use a simple line-load model to explore the impact of these changing loads on fault clamping stress and calculate stress rates. Finally, I map surface-breaking segments of the fault at a 1:4,400 scale and measure offset along fault strands. By matching fault strands to specific alluvial fans and surficial units, I can calculate the time-averaged slip rate for each scarp and compare the timing of slip before and after glaciation. I

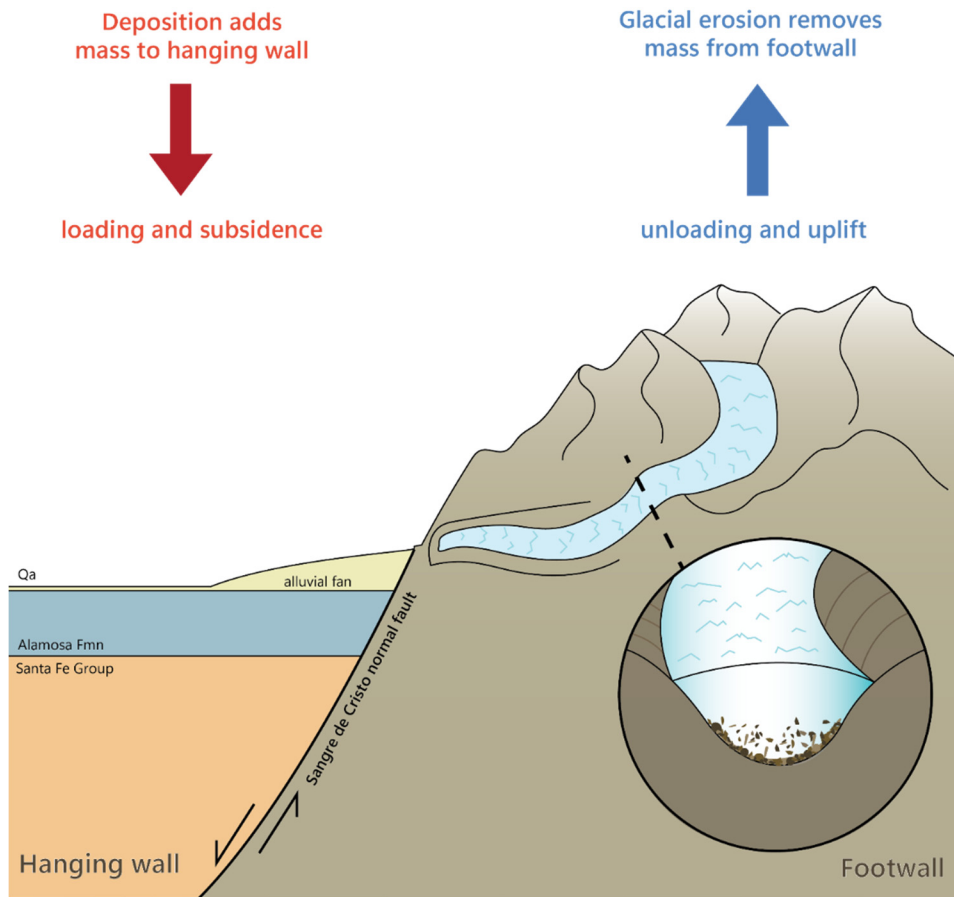


Figure 2. Simplified schematic illustrating the underlying flexural isostatic response concepts with the footwall (right) uplifting due to glacial erosional load removal, and the hanging wall (left) subsiding due to depositional loading.

hypothesize that although the total cumulative slip across the range would not be significantly different from background levels related to extension, glacial periods modulate the timing of slip, causing increased slip rates after deglaciation (Figure 3).

## 2. Background

The Sangre de Cristo Mountains record multiple orogenic events prior to the neotectonics that are the focus of this research. What is preserved in the mountain range today is primarily the result of the contractional deformation associated with the Ancestral Rocky Mountains and Laramide orogeny, which were later overprinted by magmatism and Rio Grande rift (RGR)

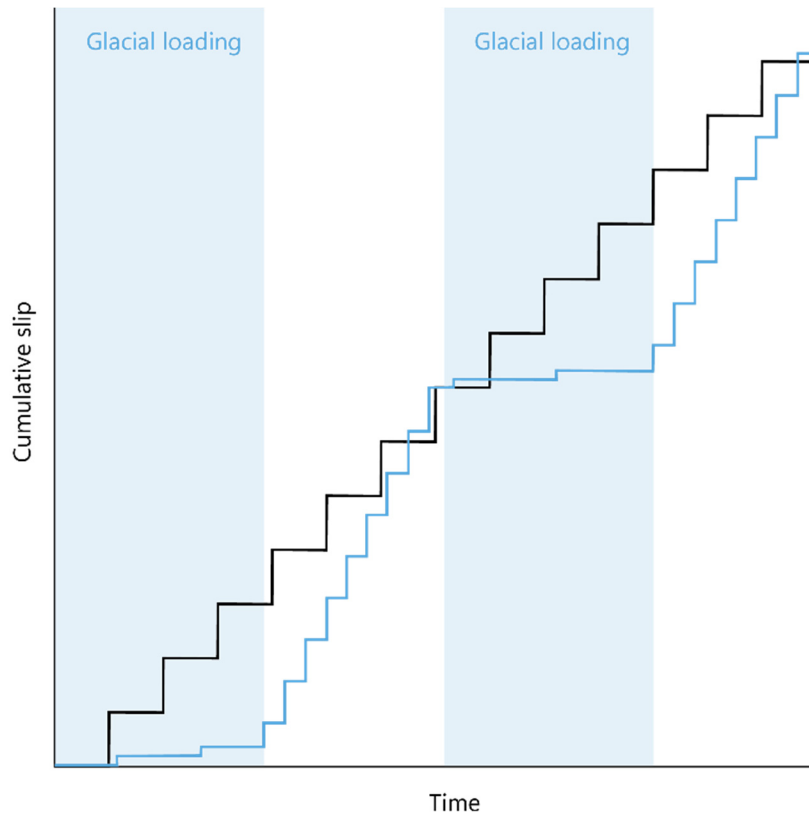


Figure 3. Conceptual model of increased slip rates post-dating glacial periods in an active, normal fault stress regime. Black line indicates an active fault with ongoing slip without glaciation. Blue line indicates a fault with punctuated slip modulated by glacial periods (indicated in blue shading).

extension. The glaciations discussed herein are the most recent events to occur in this area and coincide with RGR tectonism.

### 2.1 Ancestral Rocky Mountains and Laramide Orogeny

The Sangre de Cristo Mountains are primarily composed of Late Paleozoic sedimentary rocks along the center and eastern portions of the range, and Precambrian granites and gneisses in the northern and southern sections and the western flank of the range, including the Blanca Massif. The late Paleozoic geologic units consist of the Pennsylvanian Minturn Formation and the Pennsylvanian-Permian Sangre de Cristo Formation, both deposited during the uplift of the Ancestral Rocky Mountains (Lindsey, 2010). These units, in conjunction with the Precambrian granites and gneisses, were uplifted during the Laramide orogeny ~75–50 Ma (Lindsey et al.,

1998; Cather, 2004; Bush et al., 2016). This orogeny is characterized by ENE-WSW compression between the Colorado Plateau and the eastern North American plate and the associated subduction of the Farallon plate (e.g., Erslev and Koenig, 2009, Weil and Yonkee, 2022). The uplift of the Rocky Mountains is largely attributed to the Laramide orogeny. Many of the NE-verging thrust faults and folds that formed during this orogenic event are still well-preserved in the Pennsylvanian and Permian sedimentary units in the Sangre de Cristo Mountains. Uplift related to Laramide shortening likely did not create significant topography in the study area due to the presence of Oligocene tuff units on the eastern side of the Sangre de Cristo range (Cather, 2004; Bush et al., 2016).

## *2.2 Magmatism and Rio Grande rift*

Between ~40–18 Ma, the area experienced an increase in magmatism, often referenced as an “ignimbrite flare-up” (Lipman, 1989), where it is thought that the sinking of the subducted Farallon slab beneath the Colorado–New Mexico region allowed for melting of the lithospheric mantle via asthenospheric inflowing (Humphreys, 1995; Ricketts et al., 2016). The primary locus of this magmatism is in the San Juan volcanic complex, ~50–200 km west of the Sangre de Cristo Mountains. Interestingly, the presence of (mostly) Oligocene ignimbrites sourced from San Juan calderas (Bonanza, Marshall Pass, Bachelor, and La Garita), including the Fish Canyon Tuff, the Carpenter Ridge Tuff, the Gribbles Park and Bonanza Tuffs, and the Thorn Ranch Tuff, are located up to ~40 km east of the Sangre de Cristo Mountains, suggesting the Sangre de Cristo Mountains did not represent a significant topographic barrier in the Oligocene (McIntosh and Chapin, 2004). To put this another way, the broad extent of these volcanic units on either side of the modern Sangre de Cristo Mountains implies that most of the topography in the Sangre de Cristo Mountains was not inherited from Laramide uplift, but rather is a product of Neogene

tectonic activity associated with the Rio Grande rift.

Due to the convective heating of the lower lithosphere, the Farallon slab is proposed to have detached around 25 Ma, leaving the overlying lithosphere weakened and susceptible to extension. Low-temperature thermochronometry data and the sedimentary record in the San Luis Basin indicate that the onset of rifting began ~28–25 Ma in the northern region (Wallace, 2004; Ricketts et al., 2016; Abbey and Niemi, 2020), with Abbey and Niemi (2018) further proposing that the connection of the entire northern Rio Grande rift (RGR) system occurring around 10 Ma and undergoing post-linkage synchronous extension. Lindsey et al. (1986) estimate that uplift of the Sangre de Cristo Mountains was initiated around 19 Ma, and this rapid uplift accounts for ~2 km of relief. More recent thermochronology studies indicate that cooling rates in the Sangre de Cristo Mountains abruptly increased at ~14 Ma (Ghamedi et al., 2023)

The Sangre de Cristo fault system, which is the focus of this study, is a northern segment of the Rio Grande rift system (Figure 1, inset). The San Luis Valley represents an east-dipping half-graben of the Sangre de Cristo fault system, with the greatest displacement on faults at depth occurring on the eastern side of the basin (McCalpin, 1982), while the western margin of the basin is the hinge of the half-graben. Wallace (2004) further separates the San Luis Basin into two half-grabens: the younger Alamosa graben to the north of the Blanca Massif, and the older Culebra graben to the south. The pre-rift lithology is primarily composed of Oligocene volcanic rocks, Eocene conglomerates, and Proterozoic metamorphic and igneous basement rocks (Wallace, 2004). The basin is infilled with Oligocene to Pliocene Santa Fe Group sediments, the Pliocene-Pleistocene Alamosa Formation, and Quaternary alluvium and glacial deposits (Brister and Gries, 1994; Wallace, 2004; Lindsey, 2010).

The Sangre de Cristo fault is an active, west-dipping normal fault that structurally separates the San Luis Basin hanging wall from the Sangre de Cristo Mountains footwall block, with dips estimated to be a minimum of 45°, but more commonly 60°, as indicated by seismic reflection survey data (Kluth and Schaftenaar, 1994). While the range front fault is the focus of this study, the Sangre de Cristo fault system extends well into the San Luis Basin, and much of the displacement attributed to the fault is associated with these basin faults. It is estimated that the fault segments within the San Luis Basin accommodate up to 8.2–9.2 km of total displacement based on basin fill estimates and gravity surveys (Kluth and Schaftenaar, 1994). Additionally, on the east side of the range, the Alvarado fault bounds the eastern range front. This fault does not have the same evidence for Quaternary slip as the Sangre de Cristo fault, but the Alvarado fault was originally a Laramide thrust fault that was reactivated with normal-sense slip in the Miocene (Hoy and Ridgway, 2002).

The Sangre de Cristo fault system is expressed at the surface with NNE-SSW striking fault scarps both along the range front and in areas of relay ramps and fault splays, typically with SW-side downthrown blocks (Figure 4). According to McCalpin (1994), Holocene fault scarps averaging 1.2–2.9 m exist within the alluvial fan deposits at the range front, constituting the principal evidence for fault movement within the Quaternary. This study focuses on the range front scarps from the northern portion of the Sangre de Cristo Mountains to just south of the Blanca Massif, though there are additional fault scarps that exist in the northern-central portions of the San Luis Valley called the Villa Grove fault zone (VGFZ). The Villa Grove “fault swarm” is a zone of NW-striking fault scarps that have been previously described as an area of local

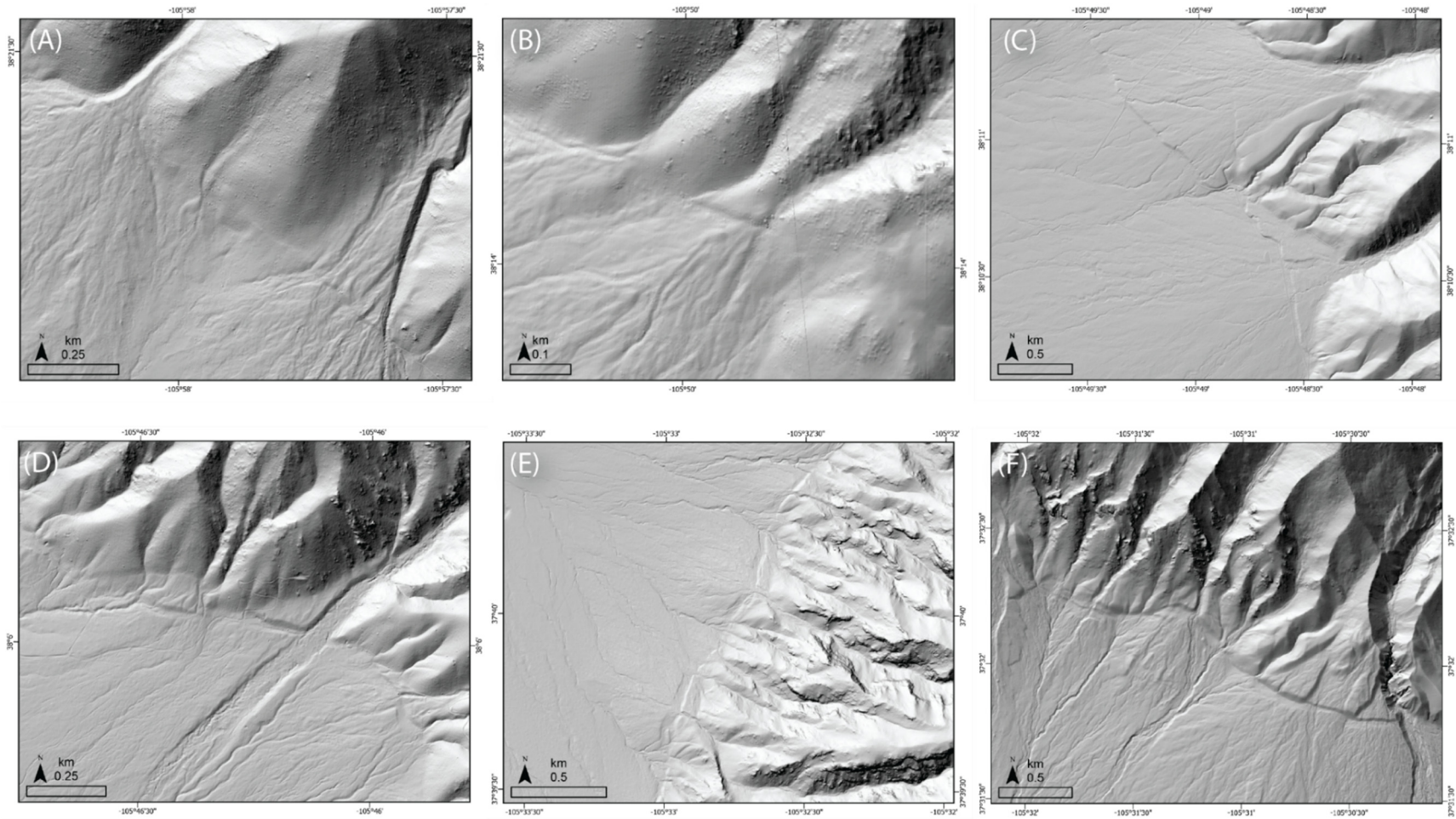


Figure 4. A variety of range front Sangre de Cristo fault scarp morphologies: (A) Nieland Creek to the NW and Butterfly creek to the SE, (B) Lime Canyon, (C) Hot Springs Creek to the N and Garner Creek to the S, (D) Wild Cherry Creek, (E) Zapata Creeks, and (F) Blanca Creek. One meter LiDAR data sourced from USGS 3DEP program.

extension that accommodates most of the displacement of the Sangre de Cristo fault offset from the main fault strand (McCalpin, 1982). The range-bounding fault has distinct alluvial fan displacements in the range fronts of the northern, central, and Blanca Massif sections.

McCalpin (1982) estimated fault scarps average approximately 2.15 m of vertical displacement. During his extensive work, he completed five trench excavations and measured 153 detailed scarp profiles along the Sangre de Cristo fault to constrain the displacement and timing of the fault. His findings suggest that in five surface-breaching faults near the main Crestone section of the fault, approximately 8.9 m of vertical displacement has accumulated since the onset of the LGM, with the number of rupture events varying per location (McCalpin, 1982). Radiocarbon dating was used to constrain recent offset at Major Creek to be around 8 ka and 8–13 ka at two separate fault movements, and optically stimulated luminescence (OSL) dating was utilized at Carr Gulch to constrain movement at 8 ka, 20 ka, and between 22.5 and 27.5 ka (McCalpin, 1982, McCalpin and Kirkham, 2006). Recurrence intervals for the fault have been estimated between 5–50 kyr, dependent on location, and slip rates for the fault are considered to be less than  $0.2 \text{ mm yr}^{-1}$  (McCalpin, 1982; Widmann et al., 1998; Machette, 2000; McCalpin et al., 2011; Personius et al., 1999, and Murray et al., 2019). Long-term horizontal extension rates in the RGR at large have been estimated to be between  $0.1\text{--}1.5 \text{ mm yr}^{-1}$  (Murray et al., 2019), with San Luis Basin-specific estimates between 0.1 and  $1.1 \text{ mm yr}^{-1}$  (Van Wijk et al., 2018), and total extension estimates have been approximated as 8–12% (Kluth and Schaftenaar 1994).

Recent work in the Blanca Massif and the surrounding region has noted increased seismicity within the Sangre de Cristo Mountains as recently as 2019 (Bell, 2020). Over 700 repeating seismic events of  $M_L \sim 0.8$  were recorded by independently-installed seismometers near

the Great Sand Dunes National Park (GSDNP) over a period of 3.5 months, all of which are associated with a W-dipping normal fault with similar geometry to the Sangre de Cristo normal fault system but located ~12 km east of the Sangre de Cristo fault and located 8–10 km deep (Bell, 2020). Due to the repetitiveness of these signals, Bell (2020) suggests that these seismic events could be associated with fluid involvement at depth. Further, the USGS ‘Latest Earthquakes’ application plots ~190 earthquakes in and around the Blanca Massif from 1985–2022 that vary in depth from 1.31–9.89 km and have an average magnitude of 1.5 (USGS ‘Latest Earthquakes’ database, accessed June 2023).

The basin-fill geologic units in the San Luis Valley relevant to this work are the Alamosa Formation and the various Quaternary deposits. The Alamosa Formation is a lacustrine deposit from the ancient Lake Alamosa, an extensive paleolake that formed in the San Luis Basin after 3.7 Ma and drained around 444–385 ka when the lake overtopped its natural dam (Machette et al., 2013; Ruleman, 2021). The top of the Alamosa Formation is well-defined in cores and geophysical data and provides a crude approximation of the lower boundary for the base of the Quaternary units of interest. The clay- and silt-dominant sediments from Lake Alamosa compose much of the Plio-Pleistocene sediment package in the basin; however, alluvium from fluvial systems draining out from glacial basins in the Sangre de Cristo Mountains have contributed significantly to the alluvial fans at the base of the range, with some extending 2.5–4 km into the basin from the foot of the mountains with slopes up to 11°. The Quaternary units in the San Luis Valley predominantly consist of floodplain alluvium, eolian deposits, alluvial fans, and locally preserved glacial moraine deposits at the range front.

### 2.3 *Glacial history*

The prior naming convention for the glacial till and alluvial fan deposits attribute the age of the deposits to previous regional glacial periods. The penultimate glaciation during Marine Isotope Stage (MIS) 6 is referred to as the Bull Lake glaciation, which lasted from approximately 190 ka to 130 ka, and the local last glacial maximum (LGM) during MIS 2 is referred to as the Pinedale glaciation, which occurred between 30 and 13 ka (McCalpin 1982, Schweinsberg et al., 2016). These glacial periods are named for their type localities in the Wind River Range, Wyoming (Pierce, 2003).

The key evidence for glaciation in the northern Sangre de Cristo Mountains consists of both erosional and depositional features (Figure 5). The high elevations of the drainage basins exhibit U-shaped valleys, horns, aretes, and trimlines characteristic of alpine glaciers that were constrained by the topography. With some minor exceptions, the lack of erosional evidence at the drainage divides demonstrates that glaciers did not extend fully to the divides, and it is commonly accepted that there is not sufficient evidence to indicate that there was an ice sheet at this location (Refsnider et al., 2009). The preservation of latero-terminal moraines at the base of these drainages, in some areas with some evidence of nested moraines, are further indicative of short-lived re-advances or temporary standstills in the retreat. Terminal moraine complexes and polished surfaces at the range front in the Sangre de Cristo Mountains were dated by Leonard et al. (2017) using the  $^{10}\text{Be}$  cosmogenic radionuclide surface exposure method. These data demonstrate that the maximum glacial extents occurred from ~21 ka until ~17–16 ka, with swift retreat to almost full deglaciation in the following ~2–3 kyrs within the drainages they investigated (Leonard et al., 2017). Moraine units tend to be more consistently preserved on the east side of the range, whereas the western side of the range only exhibits a handful of well-

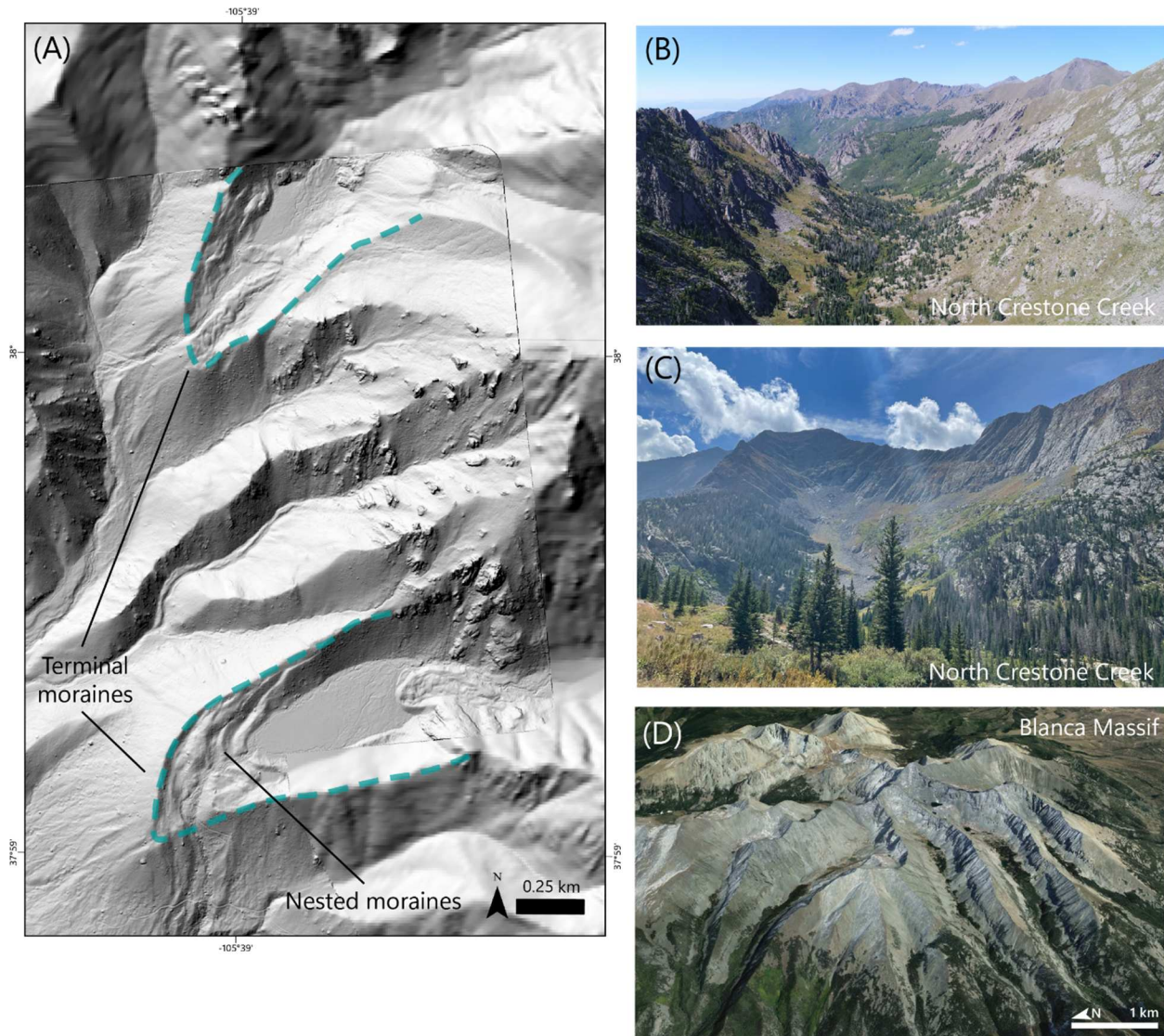


Figure 5. Evidence of glaciers in the Sangre de Cristo Mountains. (A) Composite elevation map of 1 m USGS 3DEP LiDAR and 30 m DEM of South Crestone Creek (to the north) and Willow Creek (to the south) drainage basins with terminal moraines outlined in dotted teal line, and nested moraines in Willow Creek. (B) U-shaped valley in North Crestone Creek looking NNW, note trimlines on either side of the valley. (C) U-shaped valley in North Crestone Creek looking south. (D) Google Earth imagery oblique view of Blanca Massif glacial valleys exhibiting clear trimlines, aretes, and lateral moraines.

preserved terminal moraines. Similar estimates of rapid deglaciation have been supported in the Sawatch Range, ~50 km northwest of the Sangre de Cristo Mountains, with glacial retreat occurring between 16–5.6 ka and full deglaciation by ~14 ka (Tulenکو et al., 2020).

## 2.4 Loads, stress, and flexural isostasy

The changes in stress on the system can be visualized using Mohr circles: with normal stress plotted on the horizontal axis and shear stress plotted on the vertical axis, they can demonstrate the interaction between changes in surface stresses and failure at a fault in the stress regime (Figure 6). Plotting the maximum principal stress ( $\sigma_1$ ) and minimum principal stress ( $\sigma_3$ ) on the horizontal axis, the bounds of the Mohr circle are delineated. Since the Sangre de Cristo fault system is under a normal fault stress regime,  $\sigma_1$  is vertical, and  $\sigma_3$  is horizontal and perpendicular to the fault strike. Because the fault system is already established, stresses acting on the fault are not inducing Mohr-Coulomb failure but instead inducing failure along the frictional sliding envelope for pre-existing fractures where cohesion is assumed to be zero and the coefficient of static friction is assumed to be  $\sim 0.85$  (Byerlee, 1978). Every point along the Mohr circle corresponds to a fault orientation in real space, so when the Mohr circle intersects and passes through the failure envelope, those points that pass through it are representative of individual faults that would fail.

Prior to the load removal, the normal fault system has a setting where the differential stress ( $\sigma_1 - \sigma_3$ ) is large enough to induce failure due to the ongoing extensional tectonism of the Rio Grande rift (Figure 6A). When a surficial load is added, this directly increases the vertical stress,  $\sigma_1$ , but has different effects with  $\sigma_3$ . In the lower crust,  $\sigma_3$  would decrease through lithospheric flexure as the lithosphere accommodates the addition of the load, but in the upper crust,  $\sigma_3$  would increase as the plate bends inward to compensate for the load (Figure 6B). Once the load is removed, there is a simultaneous decrease in  $\sigma_1$  and  $\sigma_3$  due to isostatic rebound that would again induce failure along existing planes of weakness (Figure 6C). With the addition of the load, the state of stress in the upper lithosphere causes the Mohr circle to shift away from the

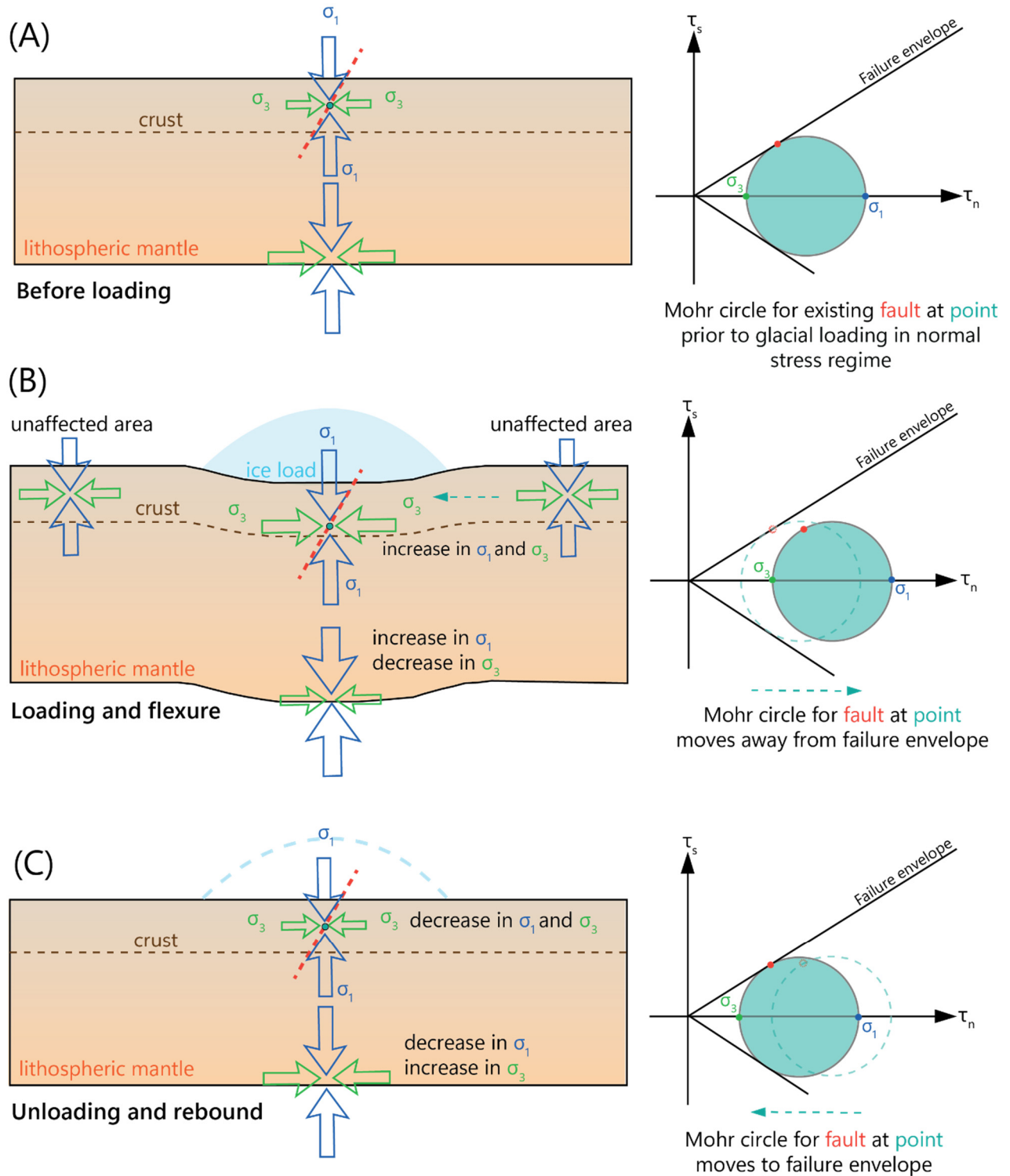


Figure 6. Conceptual model of normal fault stress regime alterations in vertical and horizontal stresses (A) prior to load addition, (B) when glacial ice sheet loads are applied, and (C) when the glacial load is removed, modified from Hampel and Hetzel (2006). Mohr circles showing failure envelope on right with example 60° normal fault shown by red dot on Mohr circle.

failure envelope with higher normal stress on the fault, which would correlate to a period of seismic quiescence. When the load is then removed, a decrease in  $\sigma_1$  and  $\sigma_3$  moves the Mohr circle back to the original stress state and prompts failure once again, correlating to a period of seismic activity. On glacial timescales, the load in question would be that of the glacial mass existing in the drainage basins and would cause fluctuations in the state of stress on 1,000–10,000-yr timescales, modulating seismic activity accordingly (Hetzel and Hampel, 2005). Glacial erosion and deposition, integrated across multiple glacial periods, would change loads and stress interactions on 100,000-yr timescales, and modulate seismic activity across much larger timescales with larger changes in loads (Hetzel and Hampel, 2005).

Molnar and England (1990) sought to define the term ‘uplift’ in their work by mathematically describing the process of various uplift terms relative to a reference frame defined by the geoid. They theorized that if there is a mean elevation  $h$ , depth to the Moho  $H$ , and a crustal thickness of  $T = H + h$ , then by isostatic principles, if valleys were eroded to a reference level (sea level in this case) through fluvial or glacial erosion, then they would expect the mean elevation to lower to approximately  $5h/6$ , assuming Airy isostasy and typical crustal and mantle densities, but the existing topography would rise by  $h$  amount due to isostatic adjustment, making the peaks higher after erosion (Figure 7). They demonstrate that although the mean elevation would lower to  $5h/6$ , the summits would be isostatically raised to  $1.8h$ .

Foster et al. (2010) investigated the relationship between climate, erosion, and tectonics in the Teton Range in Wyoming with the goal of determining if the relief caused by the removal of material from the footwall of the study area isostatically raised peak elevations as theorized by Molnar and England (1990). Removed (eroded) loads of the footwall basins were estimated by fitting an interpolated spline surface across the drainage divides and subtracting the modern

topography from the interpolated surface to yield a removed volume within the catchments (Foster et al., 2010). The Teton Basin deposition volume was estimated to the pre-Cenozoic basement rocks underlying the sediment based on gravity inversion methods based on regional gravity surveys (Foster et al., 2010). Their flexural isostasy model was performed on an elastic plate model but uses the fault geometry as a break in the plate, with the deflection on the western and eastern sides of the fault not affecting one another.

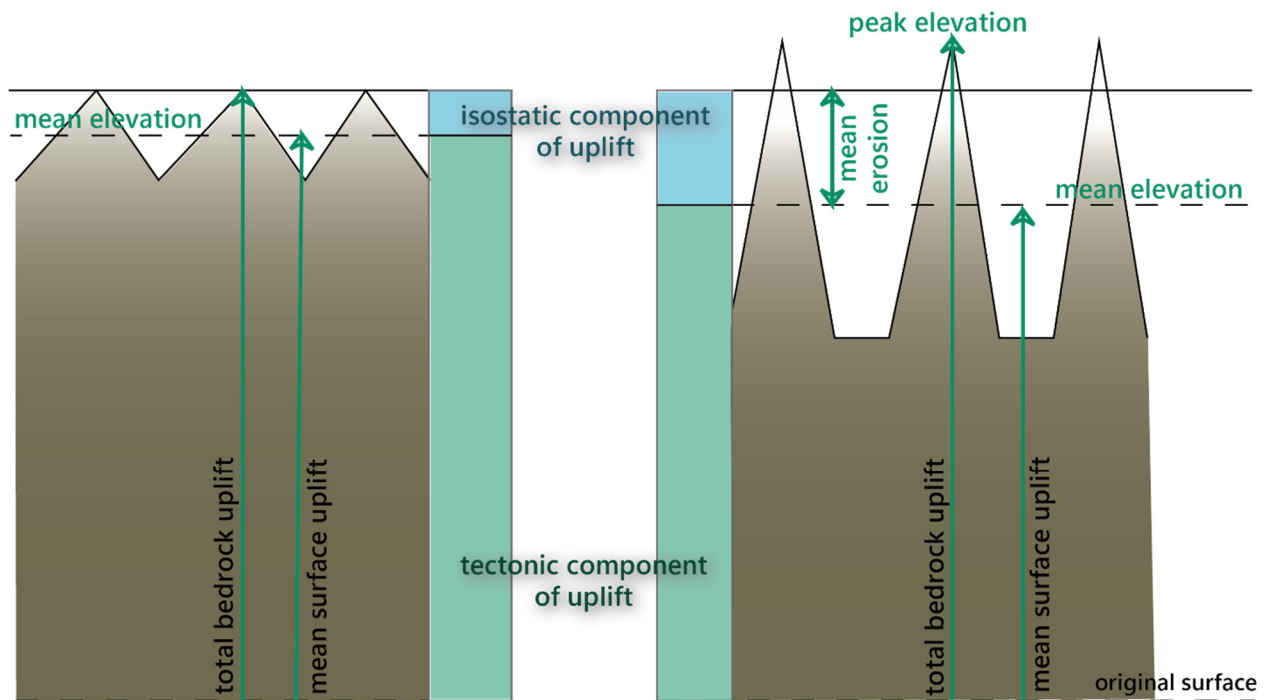


Figure 7. Schematic of Molnar and England (1990) hypothesis regarding isostatic response to erosional removal of a load, modified after Burbank and Anderson (2012). Glacial erosion preferentially erodes formerly fluvial valleys while peaks remain largely unaffected. This erosion reduces mean elevation and the associated isostatic response drives uplift of mountain peaks.

### 3. Methods

#### 3.1 Overview

To calculate the isostatic response to (1) glacial erosion and (2) associated deposition and (3) glacial ice changes in the northern Sangre de Cristo Mountains, I first used methods to establish realistic volume and mass estimates for each quantity. In each of these three

components, I calculated the volume of each through different methods (described below), and assumed a density based on the material of each component to get a mass. Once I was satisfied with the three masses constrained to their respective geographic distributions, I input these into the flexural model to derive an estimate of the isostatic response due to the respective mass changes and associated stresses they place on the fault system. I also used a simple line-load model to assess the impact of these load changes on fault clamping stress. Lastly, once I have the magnitude of isostatic response, I mapped the fault and calculated vertical offsets in Quaternary alluvium, in conjunction with researchers at the USGS, to quantify fault offset patterns to see if these larger offsets correspond to areas of glacial or fluvial dominance.

### *3.2 Glacial reconstruction*

Quantifying the load on the Sangre de Cristo Mountains due to glaciers required reconstruction of glacial extents in the drainage basins of the range. Based on the basin geometries left behind by glacial erosion, it is clear that the glaciers that inhabited the valleys were relatively small alpine glaciers and had large asymmetries between the east and west sides of the range. On the east side of the range, the glaciers tend to be consistently narrow and linear, whereas, on the west side, the glaciers have more varying geometries and tend to cover more area.

The glacial extent reconstruction process was adapted from the Pellitero et al. (2016) ArcMap-based GlaRe toolbox (Figure 8). This toolbox allows the user to recreate the 3D surface of a land-terminating paleoglacier by calculating ice thickness along the main flow lines of the glacier. Using a DEM of the modern topography for the bed slope, a user-defined input for the terminus of the glacier, and a user-defined input identifying the channel head locations, GlaRe uses a derivation of the shear stress equation:

$$\tau = \rho g H \sin(\alpha) \quad (1)$$

where  $\tau$  is the basal shear stress,  $\rho$  is the density of glacial ice,  $g$  is the acceleration due to gravity,  $H$  is the thickness of the glacier in meters, and  $\alpha$  is the surface slope of the glacier. The derivation of this equation to calculate glacier height,  $H$ , at equally-spaced nodes along the main channel of the glacier, GlaRe utilizes an iterative process put forth by Shilling and Hollin (1981):

$$h_{i+1} = h_i + \frac{\tau_{av}}{F_i \rho g} \frac{\Delta x}{H_i} \quad (2)$$

where  $h$  is the elevation of the glacier surface,  $i$  is the iteration number,  $\tau_{av}$  is the basal shear stress,  $F$  is the shape factor, and  $\Delta x$  is the length between nodes to recreate a two-dimensional representation of the glacier profile. Ice typically cannot tolerate shear stresses exceeding 150 kPa, but will not deform under stresses less than 50 kPa, therefore, an average of 100 kPa was used for each glacial reconstruction presented here (Pierce, 1979; Bennett and Glasser, 2010; Pellitero et al., 2016). I used the density of glacial ice,  $900 \text{ kg m}^{-3}$ , an acceleration due to gravity of  $9.81 \text{ m s}^{-2}$ , and a  $\Delta x$  of 30 m. The shape factor,  $F$ , was designed to account for the lateral drag that valley glaciers encounter. The shape factor is calculated by the following equation by Benn and Hulton (2010):

$$F = \frac{A}{Hp} \quad (3)$$

where  $A$  is the cross-sectional area, and  $p$  is the length of the intersection of the cross-sectional area and the underlying glacier bed. The  $F$ -factor decreases with increasing constriction, therefore, an  $F$ -factor of 1 is best suited to an ice field or an ice cap, which is not constrained by the topography, whereas valley glacier  $F$ -factors can vary between 0.7–0.9 (Jiskoot, 2011) (Figure S2). In the reconstructions for this work, the  $F$ -factor values were constrained by both erosional and depositional evidence shown in satellite and LiDAR imagery.

I coded these primary equations in Matlab and used them in tandem with TopoToolbox v2 (Schwanghart and Scherler, 2014) functions to reconstruct glacier profiles for every drainage that had depositional and/or erosional evidence of glaciation (Figure 8). With the glacial profiles and topographic constraints, I interpolated a three-dimensional glacial ice surface using standard *griddata* and *meshgrid* Matlab functions (Figure 8). Glacier termini were approximated using preserved terminal moraines where available or alternatively locations where the valley morphology changes from U-shaped to V-shaped. In total, 24 glacial reconstructions were completed for the west side, and 34 glacial reconstructions were completed for the east side.

### *3.3 Quantifying eroded material*

The objective of the erosion reconstruction is to estimate what the drainage basins would look like prior to any erosion produced by glaciation. Many glaciated valleys in the Sangre de Cristo Mountains preserved fluvial valley segments that were apparently never glaciated, providing some information on what the past fluvial topography might have looked like. Because these are preserved paleofluvial sections, their topographic metrics would be reasonable approximations of what the drainages looked like prior to glaciation, and these metrics can be used to estimate the paleofluvial topography upstream. I can use stream trunk profiles to identify which sections of individual stream profiles are dominated by glaciers and which are dominated by fluvial processes. Fluvial reaches tend to exhibit steeper slopes and occur at lower elevations, and have V-shaped valley cross-section profiles, whereas glacial reaches exist at high elevations, tend to have gentler slopes, and have U-shaped valley cross-section profiles. To quantify the amount of material that has been glacially eroded away from the drainage basins in the footwall, I use river profile analysis to reconstruct the topography of the drainages prior to glaciation. With

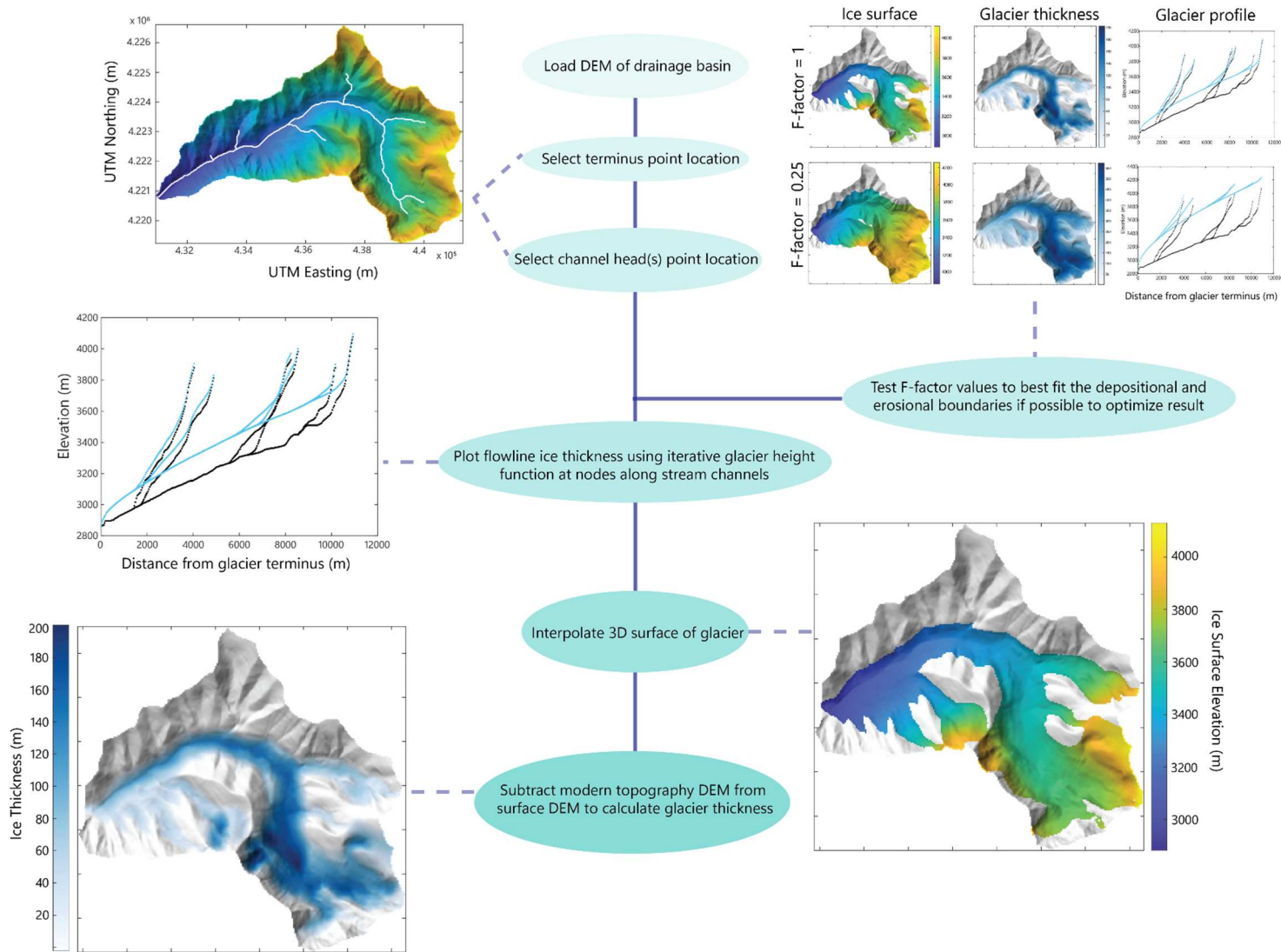


Figure 8. Schematic showing simplified glacial extent reconstruction via GlaRe process in tandem with TopoToolbox v2 functionality in Matlab. For a detailed visualization of the F-factor value rationale, see supplementary figure S2.

the ‘paleofluvial’ topography established, I differenced the present topography from the paleotopography to calculate the volume of material that has been directly eroded by glaciers.

River profile analysis centers around a simple model for bedrock rivers, the detachment-limited stream power equation:

$$\frac{dz}{dt} = U - E = U - KA^mS^n \quad (4)$$

where  $dz/dt$  represents the change in channel bed elevation through time,  $U$  represents the rock uplift rate,  $E$  represents the detachment-limited rate of bedrock incision in the channel;  $K$  is the erodibility coefficient that accounts for various qualities of hydrology, climate, bedrock erodibility, and drainage basin geometry; and both  $m$  and  $n$  are constants that account for drainage basin hydrology, stream geometry, and incision processes (Howard, 1994; Whipple and Tucker, 1999; Whipple et al., 2000; Gallen and Wegmann, 2017). If a given bedrock channel is in steady-state, then uplift and erosion rates are equivalent and  $dz/dt = 0$ ; therefore, the detachment-limited stream power equation can be rewritten in terms of slope,  $S$ , with respect to upstream drainage area,  $A$ :

$$S = \left(\frac{U}{K}\right)^{\frac{1}{n}} A^{-\left(\frac{m}{n}\right)}. \quad (5)$$

This relationship has a parallel form in the empirical Flint’s law (Flint, 1974):

$$S = k_s A^{-\theta} \quad (6)$$

where  $k_s$  represents the channel steepness index, and  $\theta$  is defined as the concavity index of the stream channel. By comparing Eq. 5 and Eq. 6, it is clear that:

$$k_s = \left(\frac{U}{K}\right)^{\frac{1}{n}} \quad (7),$$

and

$$\theta = \frac{m}{n}. \quad (8)$$

This empirical relationship is useful, but problems arise in comparing the steepness index,  $k_s$ , of channels with different concavity indices,  $\theta$ , because these parameters covary (e.g., Kirby and Whipple, 2012). To get around this issue, researchers have demonstrated the utility of using a reference concavity index,  $\theta_{ref}$ , to normalize the steepness index with the term  $k_{sn}$  to enable direct comparisons of channel steepness among river systems (Wobus et al., 2006; Kirby and Whipple, 2012; Gallen and Wegmann, 2017).

Brocklehurst and Whipple (2006) empirically calibrated  $\theta$  for thirteen fluvial drainage basins within the Sangre de Cristo Mountains and averaged a  $\theta$  value of  $0.32 \pm 0.10$ . Within the Rocky Mountain region,  $\theta$  ranges between  $\sim 0.3$  and  $\sim 0.7$ , and researchers typically use a  $\theta_{ref}$  of 0.45 based on empirical studies in steady-state channels, which is the value used for this study (Wobus et al., 2006; DiBiase et al., 2010; Kirby and Whipple, 2012; and Gallen and Wegmann, 2017). Flint's law is advantageous because  $k_{sn}$  and  $\theta$  can be obtained from digital elevation models (DEM) through log-transformation of both  $S$  and  $A$  (Wobus et al., 2006; Kirby and Whipple, 2012):

$$k_{sn} = SA^{-\theta_{ref}} \quad (9)$$

The limitation of this method is that DEMs often have artifacts, errors, and a degree of uncertainty that create noise within the topographic data, which is exacerbated when calculating slope metrics (i.e. the derivative of elevation with respect to distance). Perron and Royden (2013) developed an elegant approach,  $\chi$ -analysis, to solve this issue, substituting elevation for slope as the dependent variable and integrating the upstream drainage area as the independent variable. Separating and integrating the terms in Eq. 5 with the assumption that  $U$  and  $K$  do not vary spatially, we can assemble:

$$z(x) = z(x_b) + \left(\frac{U}{K}\right)^{\frac{1}{n}} \int_{x_b}^x \frac{dx}{A(x)^{\frac{m}{n}}} \quad (10)$$

where  $z(x)$  is the elevation at location  $x$ , and  $x_b$  is the base level of the bedrock channel (Perron and Royden, 2013; Gallen and Wegmann, 2017). Because there is a unitless ending term in the equation above, we can utilize a reference drainage area,  $A_o$ , to substitute in:

$$z(x) = z(x_b) + \left(\frac{U}{K A_o^m}\right)^{\frac{1}{n}} \chi \quad (11)$$

The term  $\chi$  is an integral term proportional to the inverse of the upstream drainage area with length units (Perron and Royden, 2013):

$$\chi = \int_{x_b}^x \left(\frac{A_o}{A(x)}\right)^{\frac{m}{n}} \quad (12)$$

and is especially useful in Eq. 11, where we see the equation is that of a line with  $z$  as the dependent variable,  $z(x_b)$  is the y-intercept,  $\left(\frac{U}{K A_o^m}\right)^{\frac{1}{n}}$  is the slope, which, when  $A_o$  is equal to 1, is the same as the normalized channel steepness index ( $k_{sn}$ ), and  $\chi$  is the independent variable. This relationship is particularly valuable for comparing the stream profiles within the study area as well as reconstructing the paleofluvial topography.

If we use a reference drainage area of 1 tethered to the  $\theta_{ref}$ , we can rewrite the slope term as:

$$z(x) = z(x_b) + k_{sn} \chi. \quad (13)$$

When plotted in both in  $\chi$ -elevation space ( $\chi$  plots) as well as distance-elevation plots, the bedrock channels in the Sangre de Cristo footwall block display a distinct morphology (Figure 9). Glacial profiles are found at high elevations and have characteristic gentle slopes, whereas the fluvial sections are lower in elevation with typically steep slopes (Brocklehurst and Whipple, 2006). By isolating the lower-elevation fluvial reaches, I can calculate the steepness through linear regressions of the fluvial reach in  $\chi$  plots to compute the slope ( $k_{sn}$ ) of that reach,

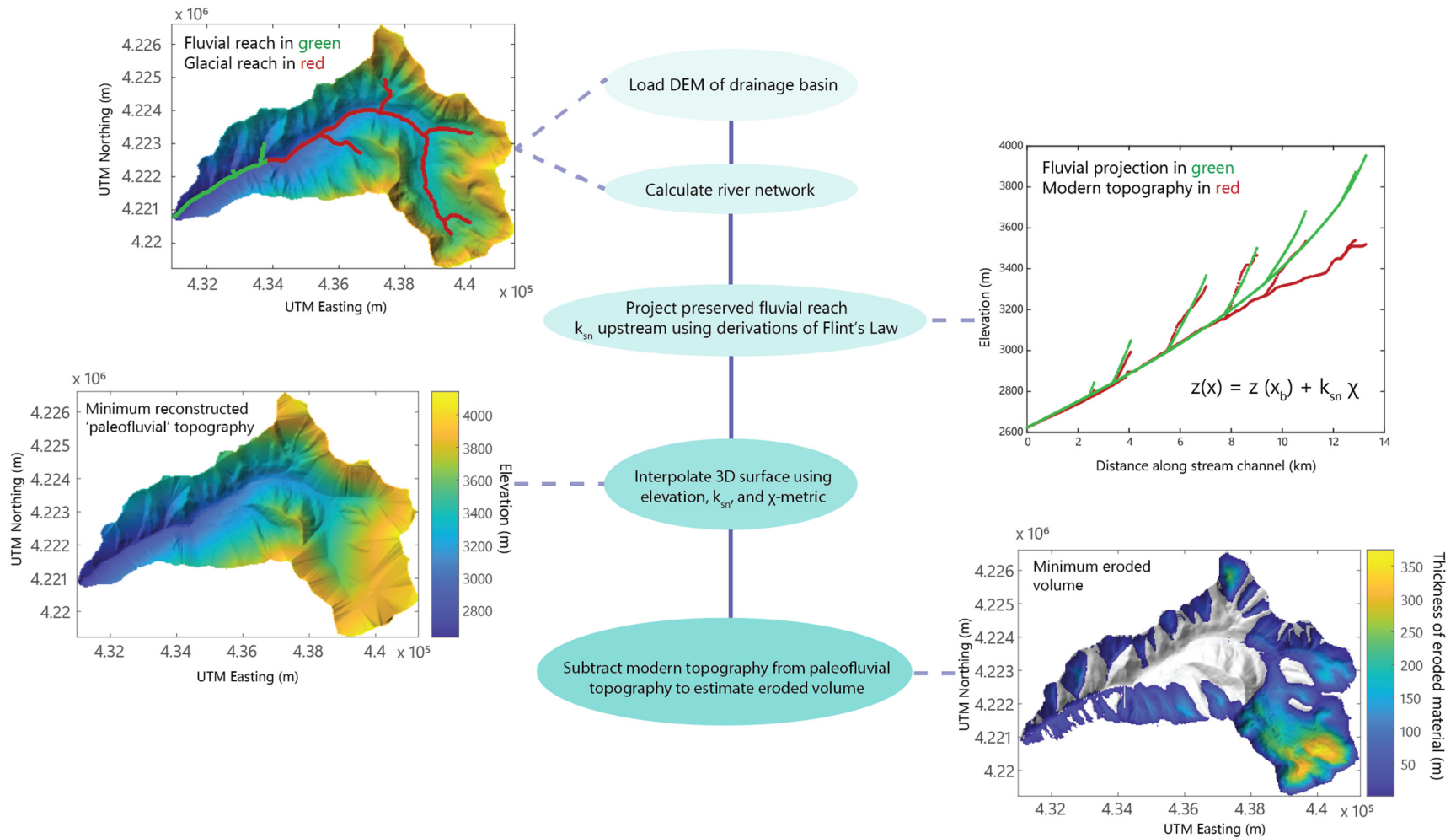


Figure 9. Erosional load reconstruction and volume calculation process flowchart, using the minimum erosional load reconstruction from the preserved fluvial reaches in the lower elevations of the drainages.

and project that steepness upstream from the glacial-fluvial boundary knickpoint to reconstruct the 'paleofluvial' topography (Figure 9).

To reconcile uncertainties in the data, I completed a Monte Carlo simulation for each drainage that consisted of 5000 iterations to calculate the mean and standard deviation of the projected fluvial elevations along the profile. Similar to the glacier reconstruction, I then interpolated the mean profile projection across the DEM surface to get the full paleofluvial reconstruction (Figure 9). Once that topography is interpolated for each basin, I mosaicked all results together in ArcGIS Pro to visualize the range-scale paleofluvial topographic reconstruction. I then subtracted the modern topography from the paleofluvial reconstructed topography to quantify the volume of the minimum eroded material that was removed by glaciers (Figure 9).

I utilized the 30 m Copernicus Global Digital Elevation Models (DEM) to complete initial topographic analyses across the study area. I filled any sinks left as artifacts in the raw DEM, and using TopoToolbox v2 (Schwanghart and Scherler, 2014), I was able to extract a drainage network for the Sangre de Cristo Mountains footwall block with a drainage area threshold of 1 km<sup>2</sup> to capture the streams that reached the drainage divides from the Sangre de Cristo fault boundary at the outlets. I completed the minimum erosion reconstruction on 58 stream channels (24 on the west side, 34 on the east side) using the *ChiProfiler* function (Gallen and Wegmann, 2017) in Matlab. I purposefully excluded drainages that did not show evidence of glaciation and those whose drainages did not reach the main divide. Within the glacially-eroded stream profiles, I selected the knickpoint that demarcated the steeper, lower-elevation fluvial sections from the more gently sloping, high-elevation glacial sections. I then calculated the

preserved fluvial reach  $k_{sn}$ , from the slope of the fluvial reach in  $\chi$ -elevation plots and extrapolated those values upstream.

During reconstructions, 13 drainages grossly over-projected the topography and created interfluves in the reconstructions. This result is likely due to the steepness of the lower fluvial segments not representing past conditions. These were modified to fit a lower and more appropriate  $\chi$ -value per the basin-specific drainage area to avoid over-predicting the amount of erosion for the minimum load volume estimate. In an attempt to make more realistic paleotopographic reconstructions, I determined the channel steepness required for the paleofluvial network to approximate the modern catchment relief so that the reconstruction did not produce anomalously high eroded volumes.

With the minimum eroded material established, it is also necessary to calculate an upper limit of the amount of material eroded from the drainages. For the maximum volume of eroded material, I used TopoToolbox v2 (Schwanghart and Scherler, 2014) functions to interpolate a surface across drainage divides, essentially masking over any eroded topography in between the divides, similar to methods done by Foster et al. (2010) (S3). Although unrealistic in a geologic sense, this would provide the greatest amount of material that could have possibly been removed through glacial and fluvial erosion. Because I am accounting for the maximal quantity of material, I included all drainages that reached the divides, including the fluvial-only drainages, which totaled 75 on the western front and 56 on the eastern side. Subtracting the modern topography from the interpolated maximum topography yields the maximum eroded volume raster.

### *3.4 Estimating deposition in the basin*

To quantify the load on the hanging wall, I estimated the amount of alluvial sediment that has been deposited in the San Luis Basin since the Quaternary, which involves both constraining the spatial extent as well as the depth of Quaternary alluvium. For the spatial distribution, I relied on the surficial geologic mapping after Thompson et al. (2015) and Ruleman and Brandt (2021) to define the boundaries between the Quaternary sediment units relevant for this study, the bedrock of the surrounding Sangre de Cristo and San Juan mountains, and the extraneous igneous units that are present in the central and southern San Luis Basin as well as outcrops of the Santa Fe Group and Lake Alamosa Formation. I verified these boundaries in ArcGIS Pro to determine a final polygon of the Quaternary surficial unit extents.

The depth to the lower boundary of the various Quaternary units proved to be a challenge due to the paucity of peer-reviewed literature that defines the base of the Quaternary alluvium and differentiates it from the underlying Lake Alamosa Formation. Many studies group the Qal and Lake Alamosa formations together or go further to group them with the underlying Santa Fe Group as well, which makes parsing out that boundary much more difficult. Brister and Gries (1994) clearly define the lower boundary of the Quaternary alluvium, and their cross-section provided key positions to constrain the interpolation. Grauch and Ruleman (2013) also provided some constraining boundary points in their cross-section in the northern portion of the San Luis Valley, and Davis et al. (2017) provided constraints near the GSDNP. After iterating over the depth data provided, it became necessary to add additional constraints along the margins of the valley to ensure that I did not estimate an erroneous or unrealistic value (such as a negative amount of material). To further refine the estimate, I added estimates of the depth in Quaternary units based on estimates from geologic maps done by Lindsey et al. (1985), Lindsey et al.

(1986), and Lindsey and Soulliere (1987). The interpolation was completed in ArcGIS with the Spline with Barriers tool using tension and bounding it to the polygon of the surficial unit boundaries with an output cell size of 300 m. I then clipped the spline surface raster to the boundary polygon to complete the depth to the lower Qal boundary volume raster.

### *3.5 Flexural isostasy modeling*

The objective for the flexural isostasy modeling was to estimate the expected deflection of the lithosphere in response to the removal of the eroded loads (both the maximum and the minimum to provide the upper and lower bounds) from the footwall, the removal of the glacial load from the footwall, and the addition of the depositional load on the hanging wall. I chose an elastic model as opposed to a viscoelastic model for the isostatic response estimations to simplify the calculation and retain similar assumptions between the isostasy model and the line load stress modeling. For the erosional unloading, the viscous relaxation time for the asthenosphere is well within the timeline of erosion of the footwall and deposition of the hanging wall ( $\sim 10^4$  yrs), so the elastic model is appropriate over these longer timescales. However, I acknowledge that the glacial unloading period is closer to the asthenospheric viscous relaxation timescale, and thus interpret my ice unloading isostatic rebound estimates as maximum deflection estimates.

I used a 2D flexural isostatic elastic half-space model outfitted with a broken plate to mimic the conditions of a normal fault (Watts, 2001):

$$q = D \frac{d^4 w}{dx^4} + \Delta \rho g w \quad (14)$$

where  $q$  is the surface load,  $D$  is the lithospheric rigidity,  $w$  is the vertical plate deflection,  $\Delta \rho$  is the difference between the mantle density and the eroded material density, and  $g$  is the acceleration due to gravity. The  $D$  parameter is solved by (Watts, 2001):

$$D = \frac{ET_e^3}{(1-\nu^2)} \quad (15)$$

I solved the model in the spectral domain, using inverse and forward Fourier Transforms to alternate between the spatial and spectral domains. I used a locally calibrated effective thickness,  $T_e$ , of 5 km from the gravity and flexure modeling work of Peterson and Roy (2005) and assumed spatially consistent  $T_e$  across the study area. I attempted independently calibrating effective elastic thicknesses for this work by fitting the pattern of footwall topography using a broken-plate flexural approximation, but, through both brute force and Bayesian inversion techniques, found low  $T_e$  values (~2 km) (Figure 10), which would indicate a very low rigidity lithosphere. While values this low have been reported in other extensional settings (Armijo et al., 1996; Goren et al., 2014; Gallen and Fernández-Blanco, 2021), I favor the more conservative values from Peterson and Roy (2005) but used both estimates throughout. The other inputs into the flexural isostatic model consisted of an eroded material density of 2700 kg m<sup>-3</sup>, a depositional sediment density of 2000 kg m<sup>-3</sup>, a mantle density of 3300 kg m<sup>-3</sup>, a glacial ice density of 900 kg m<sup>-3</sup>, a Young's modulus of 10<sup>11</sup> Pa, and a Poisson's ratio of 0.25. Flexural response modeling was completed using Matlab functions after Gallen and Thigpen (2018). To ensure that the model result is not affected by edge effects, I extended the model domain approximately 60 km NW of the study area, ~80 km SE of the study area, and 95 km on either side of the fault.

To mimic a broken plate segment for the fault, I modeled loads on either side of the fault independently and did not allow nodes to communicate across the fault, similar to the approach of Foster et al. (2010); however, I additionally mirrored each load on either side of the fault (Figure 11). By doing this, edge effects at the fault location are eliminated that erroneously dampen the deflection at the fault (Figure 11). While imperfect, this model design enables a reasonable approach to simulate the broken segment of the plate. This procedure was done by

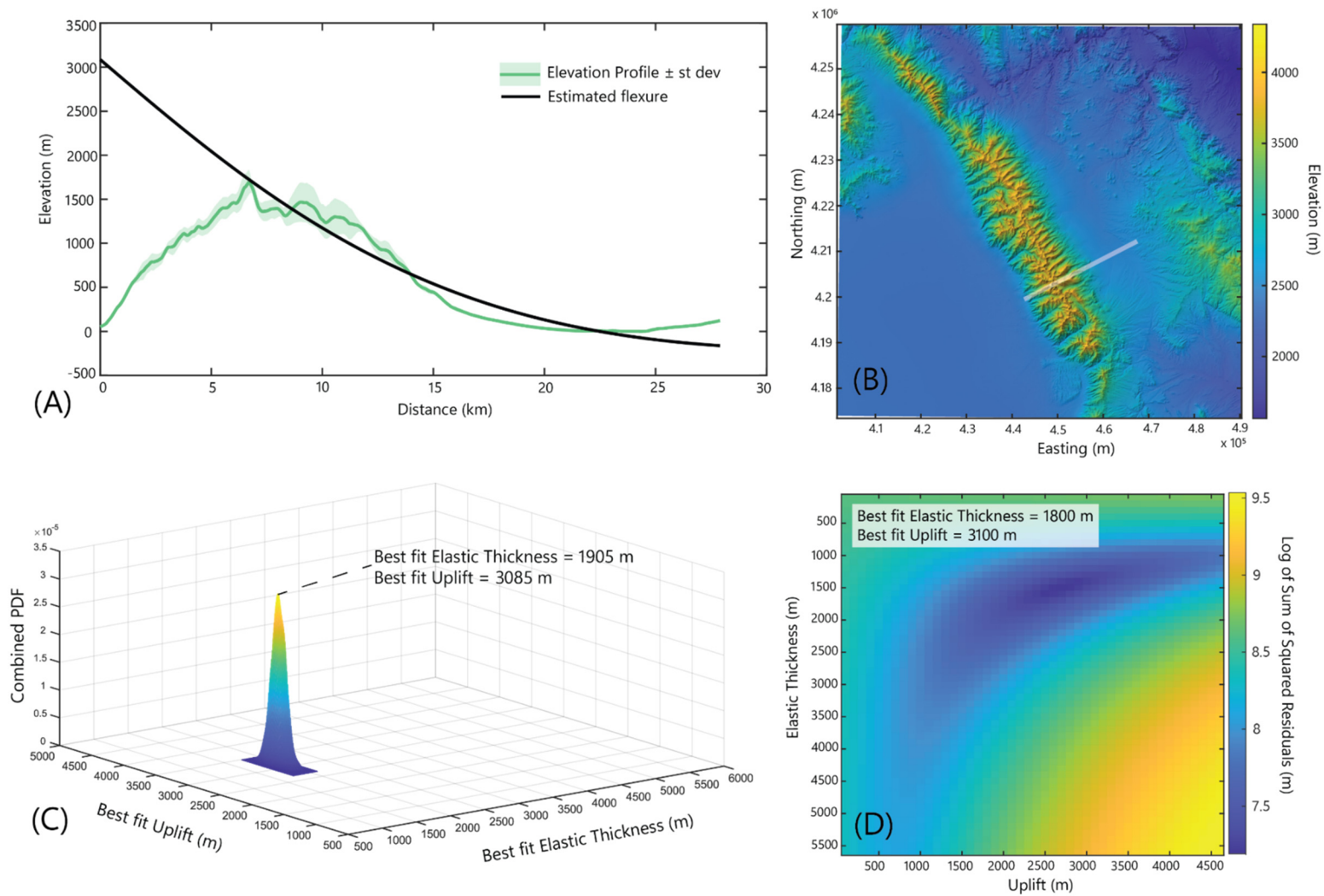


Figure 10. Calculation of calibrated effective elastic thickness ( $T_e$ ) based on topographic flexure. (A) Elevation profile with our estimated flexural profile. (B) Location of elevation swath used for calculations. (C) Results of the best fit  $T_e$  and Uplift magnitudes via Bayesian inversion calculations. (D) Best fit area in dark blue for brute force calculations.

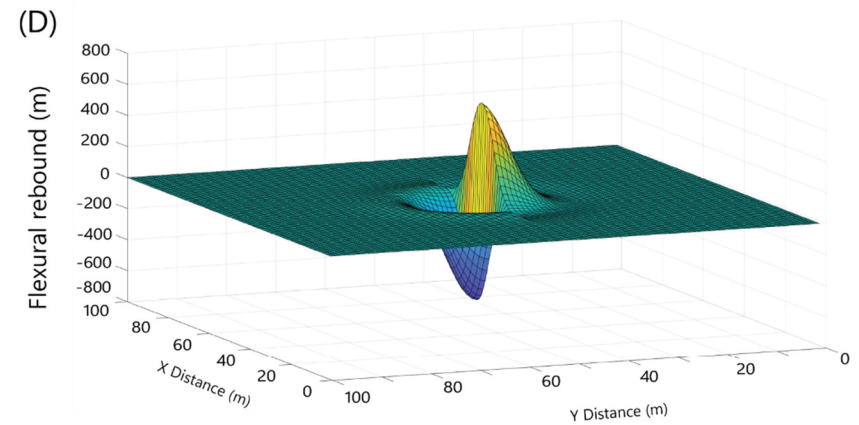
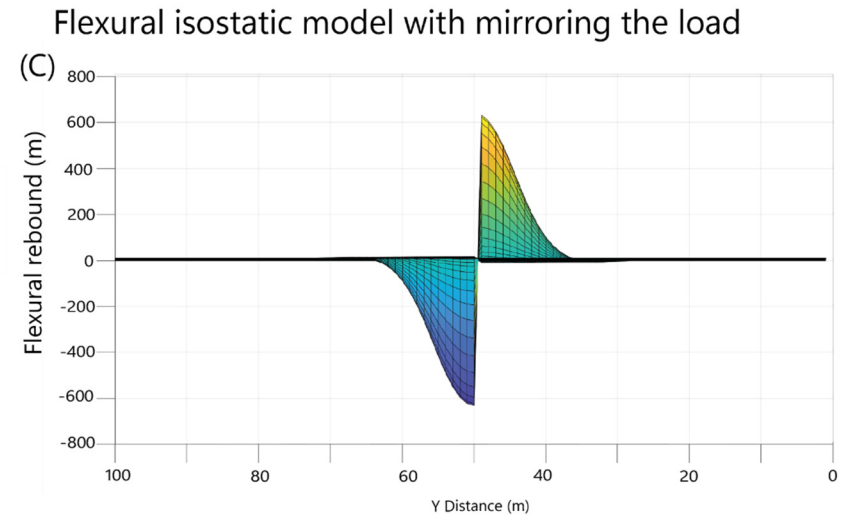
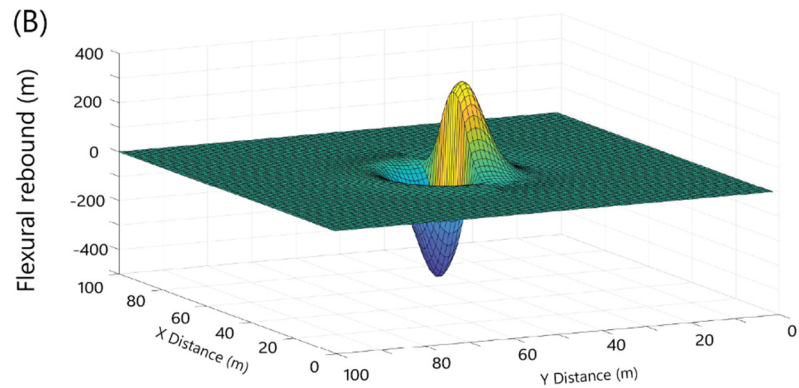
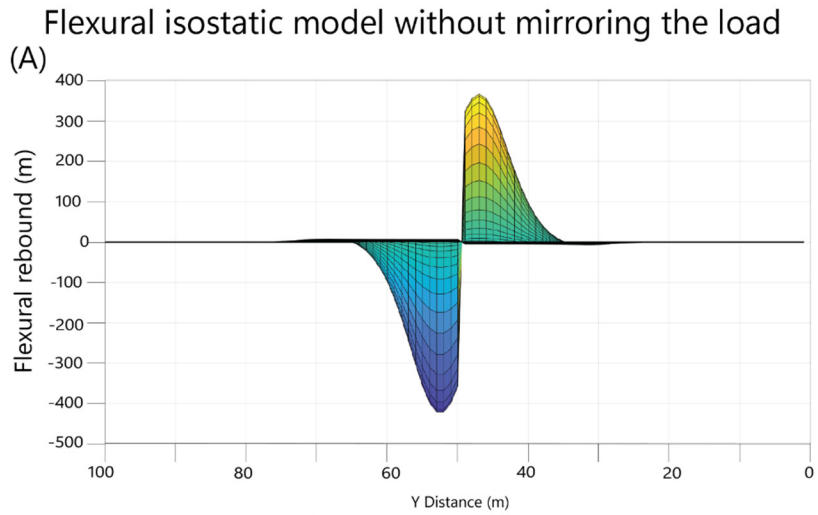


Figure 11. Broken plate isostatic model framework. Elastic half-space model without mirroring the load in (A) and (B), and with mirroring the load in (C) and (D). Note difference in curvature of the rebound at the maxima and minima near the ‘fault’ break.

importing each reconstructed load as a raster into ArcGIS, then creating duplicates of each raster to manipulate its placement in a mirrored reflection across the regional orientation of the Sangre de Cristo fault. Using the Mirror, Rotate, and Shift tools in ArcGIS, I created a reflected raster of each load across the fault, then used the Mosaic to New Raster tool to merge the original volume data raster in its correct location with the corresponding mirrored raster, resulting in a combined raster with both the original and reflected data. This was completed for the glacial, minimum and maximum erosional, and depositional loads. These rasters were then input into the isostasy model, and only record the flexural response on the side of the fault with the original load. For the composite erosion-deposition loads, the flexural responses were combined. This approach serves to eliminate the rounding that occurs when the load is not mirrored (Figure 11A), creating a discontinuous boundary that is expected for a normal fault (Figure 11C).

### 3.6 Fault stress modeling

I quantified the amount of stress at the fault due to the various removal or addition of loads by utilizing a line load model to extract the stress on the flexural model results at depth. Amos et al. (2014) calculated the two-dimensional stress components  $\tau_{xx}$  and  $\tau_{zz}$  at a given point caused by a distributed line load  $N_o$ , referenced to the  $\theta_1$  and  $\theta_2$  angles from the load edges (measured clockwise from the positive  $x$  direction,  $z$  is the positive downward direction):

$$\tau_{xx} = \frac{N_o}{2\pi a} [(\theta_1 - \theta_2) + \sin(\theta_1 - \theta_2) \cos(\theta_1 + \theta_2)] \quad (16)$$

$$\tau_{zz} = \frac{N_o}{2\pi a} [(\theta_1 - \theta_2) - \sin(\theta_1 - \theta_2) \cos(\theta_1 + \theta_2)] \quad (17)$$

$$\tau_{xz} = \frac{N_o}{2\pi a} [\sin(\theta_1 - \theta_2) \sin(\theta_1 + \theta_2)] \quad (18)$$

where  $a$  is half of the width of the load. The shear stress,  $\tau_s$ , and normal stress,  $\tau_n$ , elements on the fault plane can then be solved for, with dip angle  $\varphi$  on a strike perpendicular to the  $xz$  plane:

$$\tau_s = (\tau_{zz} - \tau_{xx}) \sin(\varphi) \cos(\varphi) + \tau_{xz}(\cos^2(\varphi) - \sin^2(\varphi)) \quad (19)$$

$$\tau_n = \tau_{zz}\cos^2(\varphi) - 2\tau_{xz}\sin(\varphi)\cos(\varphi) + \tau_{xx}\sin^2(\varphi) \quad (20)$$

If a line perpendicular to the general strike of the Sangre de Cristo fault is chosen, I can calculate the normal and shear stresses by assuming a dip angle of  $60^\circ$  for the fault if the coefficient of friction, pore-fluid pressure, and cohesion do not vary significantly over time:

$$\Delta\sigma_c = \Delta|\tau_s| + \mu\Delta\tau_n \quad (21)$$

where  $\Delta\sigma_c$  is the change in Coulomb stress, and  $\mu$  is the coefficient of friction. Using techniques put forth by Jaeger et al. (2009) and Amos et al. (2014), I can model the stress changes with line load distributions reproducing the elastic response of the lithosphere to the various loads (Figure 12). I calculate the change in stress at a depth of 8, 10, and 12 km based on estimates of earthquake nucleation for historic Basin and Range earthquakes (Doser and Smith, 1989) and recent seismicity work near the Blanca Massif (Bell, 2020).

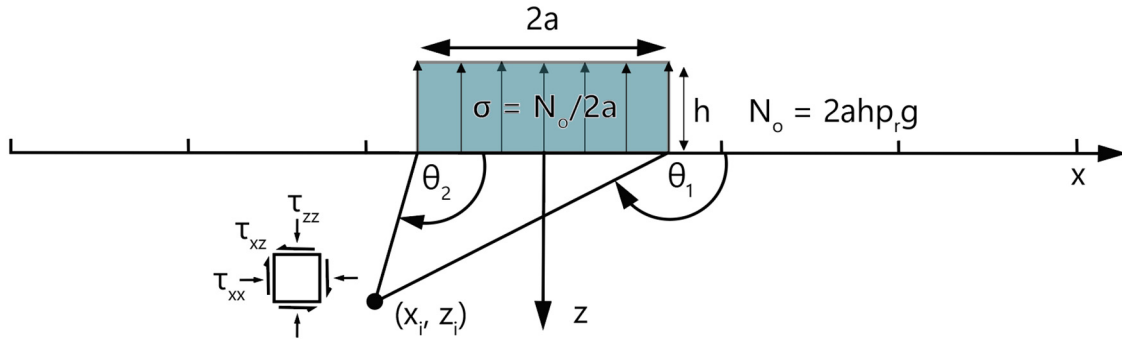


Figure 12. Diagram of the stress modeling using line loads for stress change estimation. Modified from Jaeger et al. (2009).

### 3.7 Surface uplift

The surface uplift in the area was calculated by running the minimum eroded load through the flexural isostasy model as a loading stress instead of an unloading stress, as done

before. I then added the paleofluvial topography raster to the resulting raster of the loading in ArcGIS Pro using raster math functionality to yield the isostatically adjusted paleofluvial topography. I subtracted the modern topography raster from the paleofluvial topography raster in ArcGIS Pro to visualize the surface uplift of the study area.

### *3.8 Fault scarp mapping and offset quantification*

I mapped the fault at a scale of 1:4,400 in conjunction with efforts with USGS researchers to map surface-breaching fault scarps at a scale finer than currently available. I utilized the USGS 3DEP LiDAR product, which was available at a 1 m-resolution for the study area. I additionally created slope and profile curvature maps to further enhance any signature of a fault scarp not visible solely through the LiDAR. Each identified fault strand was mapped in ArcGIS Pro, and given seven attributes: an identifier, a type (fault or lineament), an origin (tectonic, fluvial, questionable), identification confidence (certain, questionable, uncertain), measurability (measurable or unmeasurable), mapping confidence (certain, inferred, concealed), and any relevant notes (such as fluvially or anthropogenically modified). In total, 980 fault strands were identified throughout the mapping process, including the Villa Grove Fault Zone group of fault scarps (Figure 13).

I additionally conducted two field surveys in August and October of 2022 to determine if using a kinematic GPS would further refine the fault scarp profiles. I completed 27 transects across 14 scarps in August. When reviewing the data, it was clear that due to the increased vegetation in the central and southern parts of the study area, the high-resolution kinematic GPS could not adequately penetrate the vegetative cover and resulted in erroneous transect data (Figure 14). To further determine the accuracy of this reasoning, I conducted a follow-up field visit in October to verify that vegetation was causing issues and not human error. During this excursion, I completed

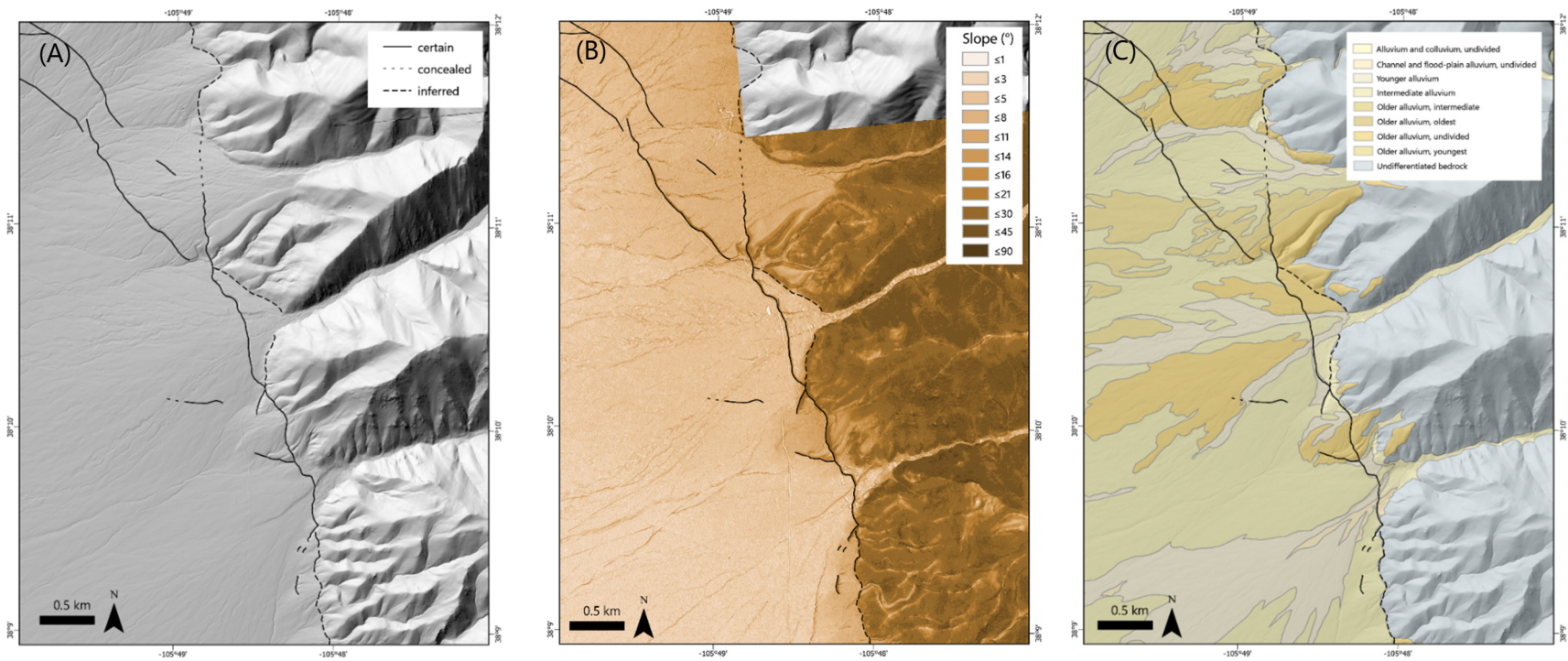


Figure 13. Example of mapping the Sangre de Cristo fault scarps using (A) the 3DEP 1 m resolution DEM product and (B) a slope map derived from 3DEP data. Ruleman and Brandt (2021) surficial mapping associations shown in (C).

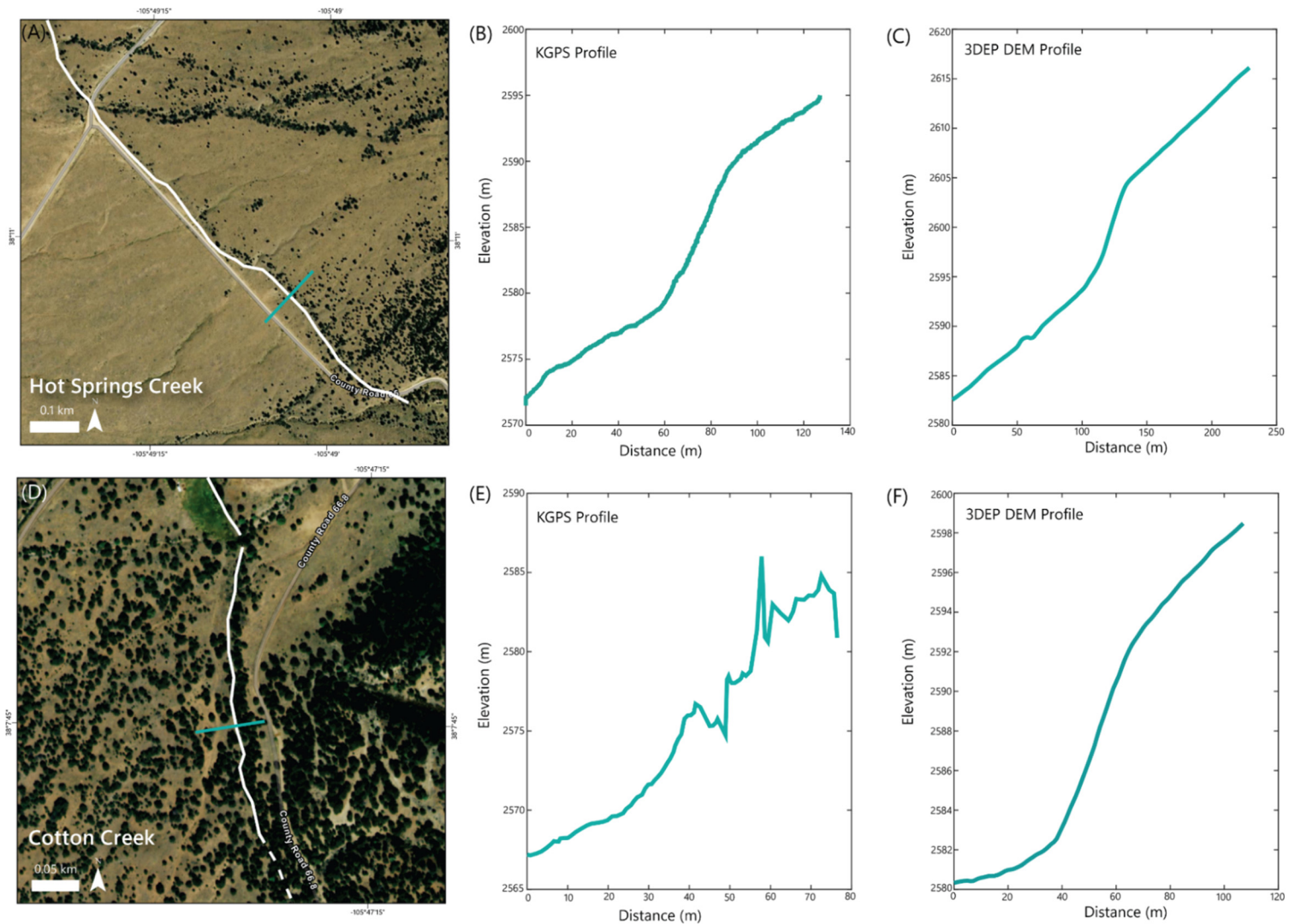


Figure 14. Comparison of scarp profile processes with Hot Springs Creek (A) as a less heavily vegetated scarp and Cotton Creek (D) as a more heavily vegetated scarp. (B) Scarp profile near Hot Springs Creek with the kinematic GPS profile taken in the field and (C) the 1 m-resolution 3DEP digital elevation model profile done in Matlab. (E) Scarp profile near Cotton Creek with the kinematic GPS profile taken in the field and (F) the 1m-resolution 3DEP digital elevation model profile done in Matlab.

14 transects across 7 scarps. Based on the results from this field excursion, it was clear that the vegetation was inhibiting the accuracy of the readings, and that this method of data collection would not be as accurate as using the USGS 3DEP LiDAR data. Although this was a helpful set of trips to the field site to get a sense of the size of the scarps and the state of diffusion they exhibited, this method did not produce fruitful results for the purposes of this analysis.

I developed a Matlab tool to measure the fault offsets along perpendicular profiles in the 1 m LiDAR data (Figure 15). The tool allows us to first load in the raster of the area of interest and draw transect profiles normal to the fault scarp strike. With the profile drawn, I can fit linear regressions through the upper and lower ramps of the scarp, then identify the midpoint of the scarp to calculate the offset at that point with 95% uncertainty. After the offset is calculated, the user can input a quality ranking. I used a scale of 1–5 to rank the quality of the offset measurements recorded. The tool saves the location data, offset data, quality ranking, and linear regression data into an excel file for future reference. To further evaluate the data, I averaged the offset data to calculate the mean for each fault strand and only used offset data that were ranked a 4 or 5 for the quality ranking to ensure only the most accurate data were used. The final dataset for the analysis of the fault scarp offset included 579 profiles on 180 individual fault scarps.

To associate the age of the fault scarps, I attributed each fault scarp to a specific alluvial fan, as mapped by Ruleman and Brandt (2021) (Figure 13c). This map specifies the surficial geology at a scale of 1:75,000, which is considerably larger than the scale of the fault mapping, which could introduce a degree of inaccuracy in the age estimates. Although the scale is not ideal for my analysis, this is the most accurate and up-to-date map of the area at the time of this research. The relevant units for the purposes of this study included: Qa, Qey, Qac, and Qls units that spanned the Holocene (0–11.7 ka); Qay and Qtb units that were associated with the late Pleistocene

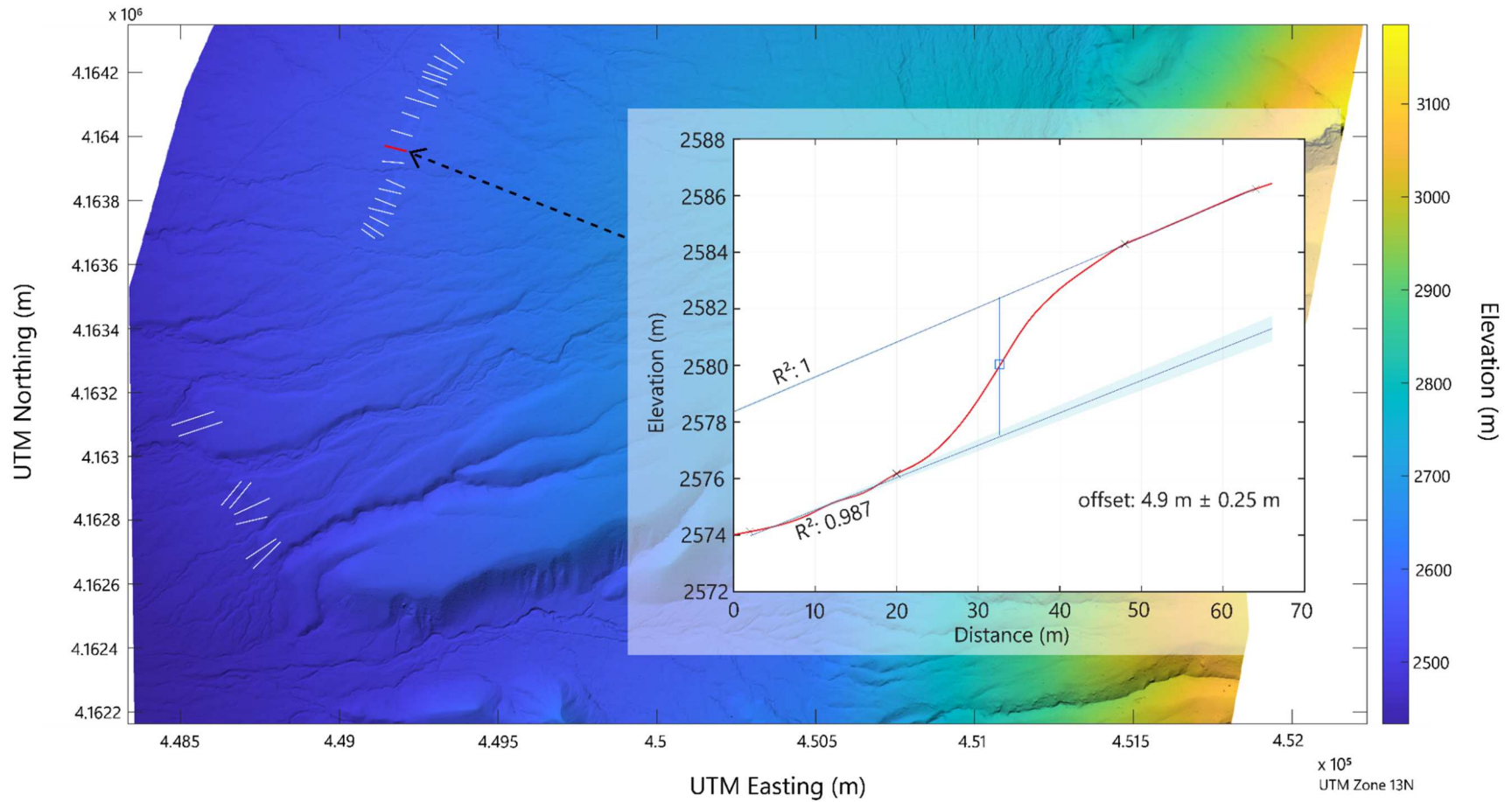


Figure 15. Example of offset measuring tool. Background: DEM overview map showing selected profiles for a round of profile measurements. Inset: scarp profile example with linear regressions on upper and lower ramps of scarp, midpoint selected at the center of the scarp, and the offset calculation with uncertainty shaded.

(11.7 ka–129 ka); Qai and Qtb units that were associated with mid-Pleistocene (129 ka–774 ka); and Qao3, Qao2, Qao, and Qtpb that spanned the early Pleistocene (774 ka–2.58 Ma). To calculate conservative estimates of fault slip rates, I divided the average offset magnitudes by the age associated with the alluvial unit that the fault scarp was mapped in. I used 11.7 ka for faults found in Holocene units, 60 ka for the late Pleistocene offsets, 129 ka for mid-Pleistocene offsets, and 774 ka for the early Pleistocene offsets. These values were chosen to estimate the slowest possible rates for the Holocene to compare to the highest possible rates for the Pleistocene in an effort to conservatively explore the idea of faster slip during the post-glacial period during the Holocene.

## **4. Results**

### *4.1 Glacial reconstruction*

Using trimlines, U-shaped valleys, and terminal moraines in both DEM and satellite imagery to constrain the glacial model, the outputs of the glacial reconstruction demonstrate a concentration of glaciation in three areas: in the north, along the central section of the mountain range, and on the Blanca Massif in the southernmost extent of the study area (Figure 16). Interspersing these regions are two stretches of unglaciated (fluvial-only) drainages. *F*-factors for the reconstructions varied between 0.75 and 1 based on the erosional and depositional constraints in the drainages, coincident with values typical for valley glaciers (Jiskoot, 2011). There is a distinct difference in the morphology of the glaciers between the western and eastern sides of the range: the west side demonstrates generally more complex morphologies, with the channel heads often initiating in orientations normal to or oblique to the trunk of the drainage and curving their way to the main channel (Figure 16). The western drainages typically have multiple channel heads and tributaries (Figure 16). The western glaciers rarely exhibit preserved terminal moraine complexes, so the terminus in the reconstructions was input by changes from U-shaped to

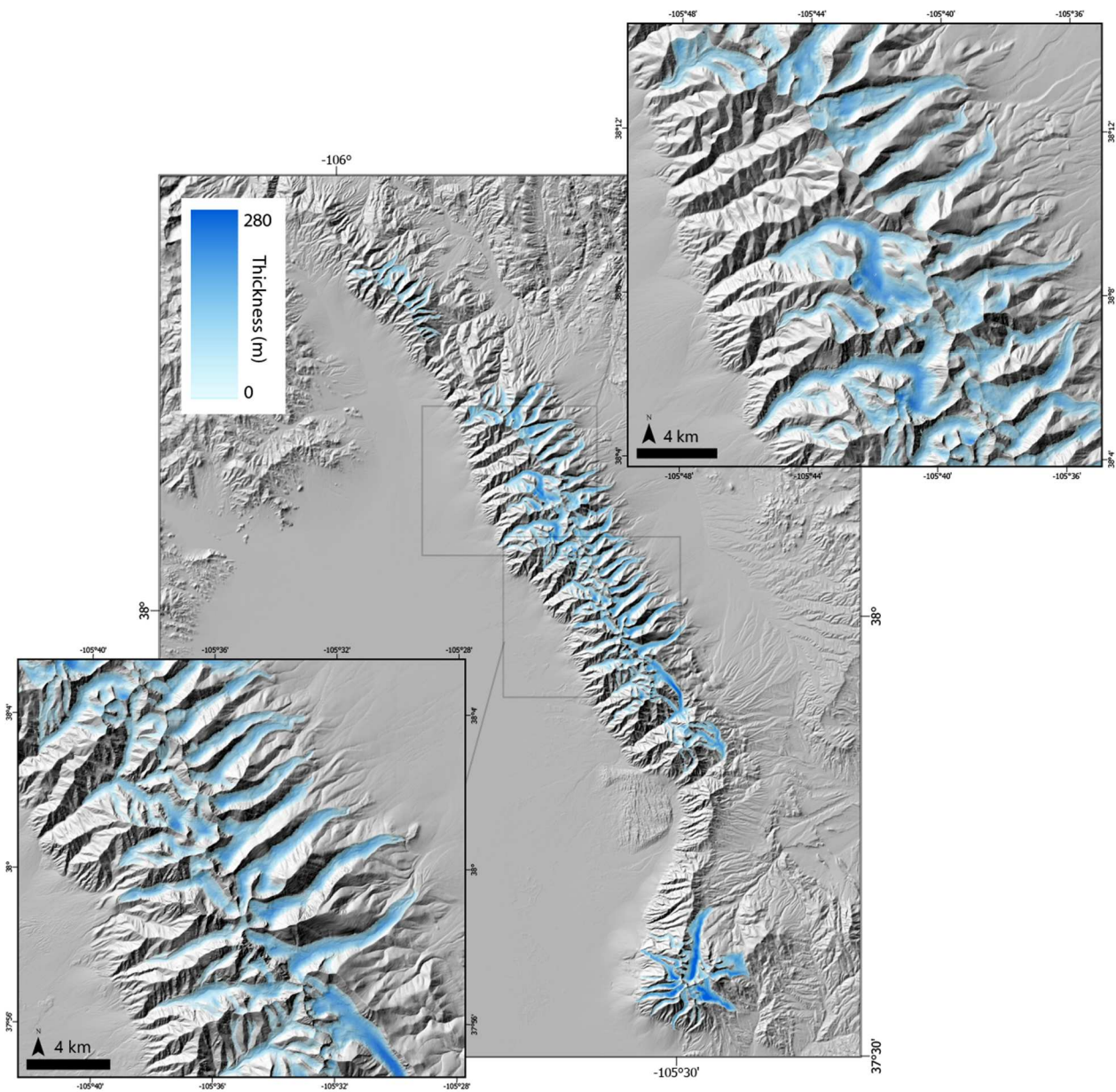


Figure 16. Compiled glacier extent and thickness reconstructions. Note the three dominant sections in the north, the center, and on the Blanca Massif. Detailed view of reconstructions added on margins.

V-shaped valleys when no moraine deposit was present. Furthermore, many western glaciers did not have evidence of extending across the range front fault. In contrast, the eastern side of the range has consistently linear valleys that trend ENE-WSW and typically exhibit one straight

main trunk with fewer tributaries (Figure 16). The eastern drainages often had well-preserved lateral and terminal moraines that provided precise terminus locations for the glacier reconstructions. The differences in moraine preservation are perhaps due to differences in valley constriction. Western drainages tend to have larger drainage areas that are more constricted at the outlet, which in turn might have more easily eroded than the eastern drainages once fluvial systems were re-established in the post-glacial period.

#### *4.2 Erosional reconstructions*

The minimum eroded reconstructions demonstrate a clear alteration from the characteristic U-shaped valleys in the modern topography to V-shaped valleys characteristic of fluvially eroded drainages (Figure 17). The bulk of the eroded material was concentrated near the drainage divides and higher elevations. The total volume of the minimum eroded material from the footwall block through glacial erosion is  $\sim 4,503,990 \text{ m}^3$ . The volume of the maximum eroded material through both glacial and fluvial erosion is  $\sim 10,085,850 \text{ m}^3$ .

#### *4.3 Deposition interpolation*

The deposition interpolation results indicate a spatial pattern with the deepest Qal accumulation under the GSDNP area, with depths reaching a maximum of almost 265 m (Figure 18). Deeper sediment accumulation also occurs along range front areas with well-developed alluvial fans and eolian dunes. Central areas have thinner coverage of Qal due to prominent surface outcrops of the Lake Alamosa Formation, and the southern region just beyond the study area has surface outcrops of Early Pliocene Santa Fe Group and volcanics (Figure 18).

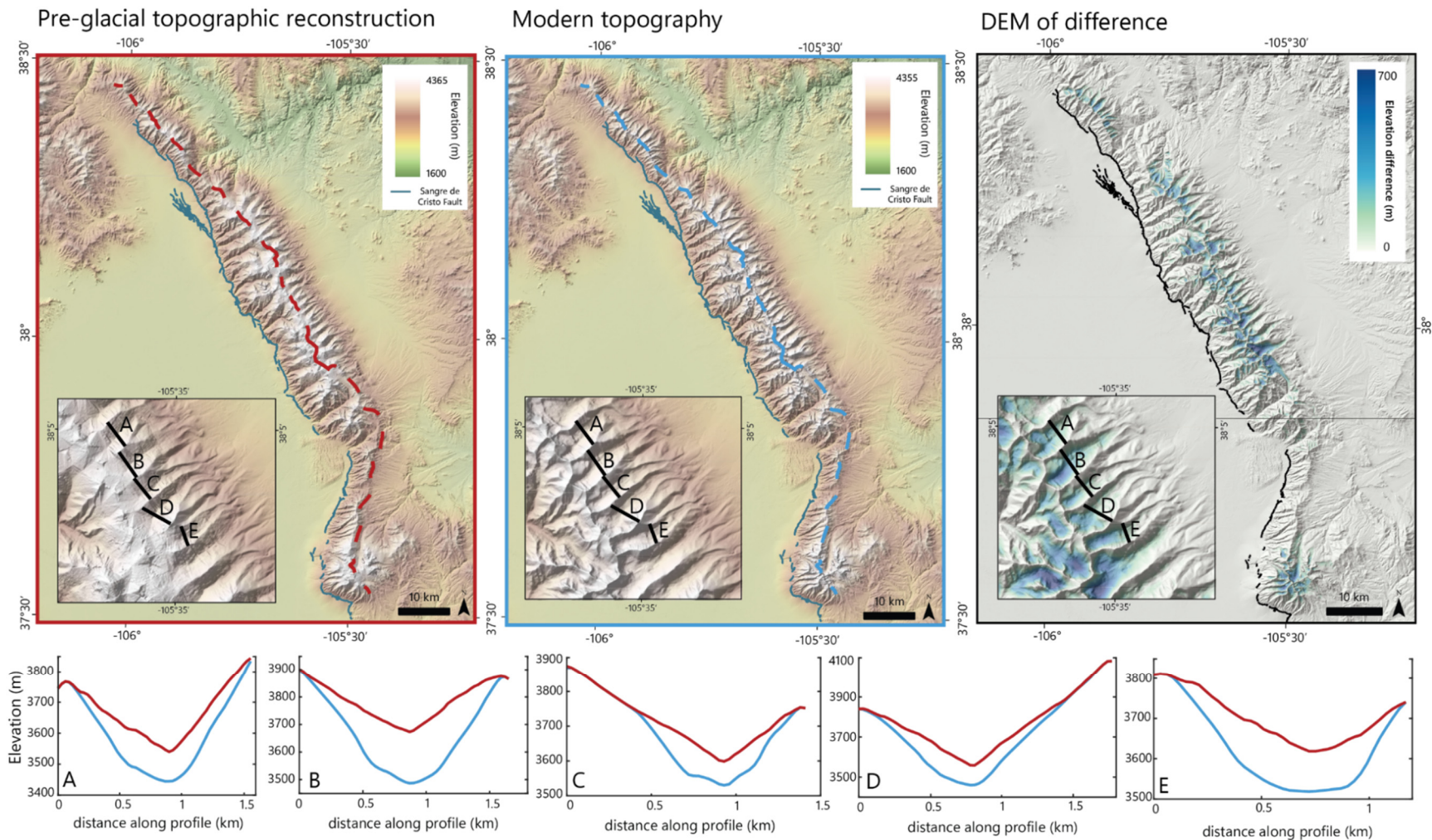


Figure 17. DEMs showing pre-glacial (paleofluvial) topographic reconstruction based on the minimum erosional load constraints, the modern topography DEM, and the DEM of difference showing the modern topography subtracted from the paleofluvial topographic reconstruction. Sangre de Cristo fault indicated along range front. Profiles of five valleys shown in bottom panel with modern topography in blue and paleofluvial topography in red. Location of each profile shown in zoomed-in insets for each map. Central dotted line in the pre-glacial and modern DEMs indicates location of swaths with a 2 km width shown in Figure 22.

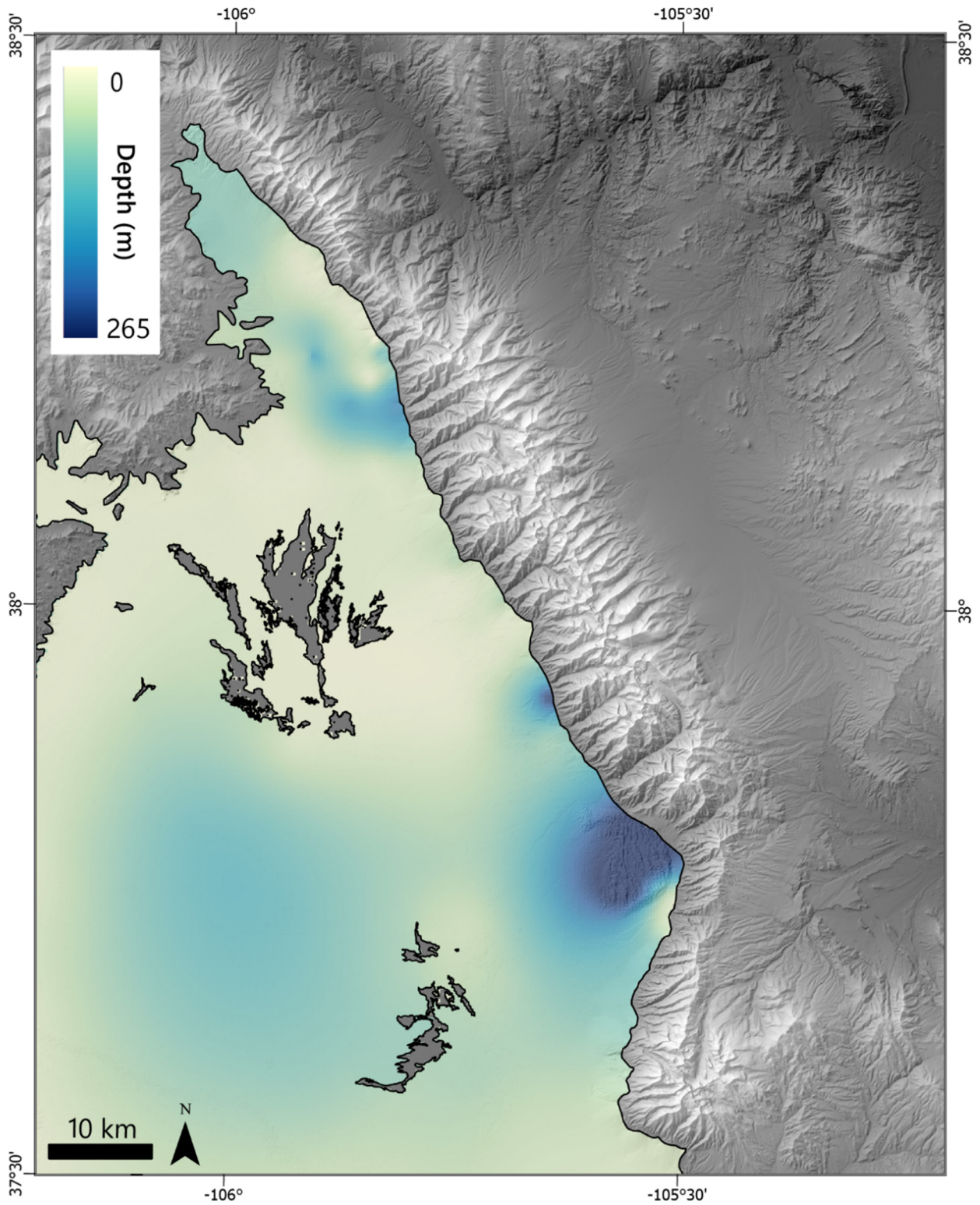


Figure 18. Depth to lower Quaternary alluvium boundary. Note that center polygons are outcrops of the Lake Alamosa Formation according to Ruleman and Brandt (2021) and therefore excluded from the depth interpolation. SRTM 30m DEM with hillshade is displayed in the surrounding units.

The deposition interpolation was extended beyond the boundaries of the study area to account for any edge effects when input into the flexural isostasy model.

#### *4.4 Isostasy model*

The outputs of the isostasy model are separated into four components based on the reconstructions I estimated: the minimum erosion deflection due to unloading, the maximum erosion deflection due to unloading, the glacier deflection due to unloading, and the depositional deflection due to loading. For a  $T_e$  of 5 km, the highest deflection due to the minimum erosional load is 29 m, centering around the main section of the Sangre de Cristo Mountains (Figure 19). The highest deflection in the footwall due to the maximum erosional load is 113 m, with the spatial extent of the deflection extending down into the GSDNP area (Figure 19). The maximum deflection of the depositional loading is -47 m centered around the GSDNP area and ~35 km WSW of the GSDNP. The load amount for the surface uplift construction was the inverse of the unloading, with a maximum of -29 m (Figure 19). The maximum footwall deflection of the glacial unloading is ~4 m, centered around Rito Alto and San Isabel creeks in the center of the mountain range (Figure 20).

For the  $T_e$  of 2 km to estimate the independently calibrated elastic thickness based on the flexure of the topography, the spatial distributions of deflection are similar to that of  $T_e = 5$  km, but due to the lower rigidity, the magnitudes of deflection are much larger. The highest deflection due to the minimum erosional load is ~48 m, the highest deflection in the footwall due to the maximum erosional load is ~170 m, the maximum deflection of the depositional loading is -80 m, and the maximum footwall deflection of the glacial unloading is ~6 m (Figures 19, 20).

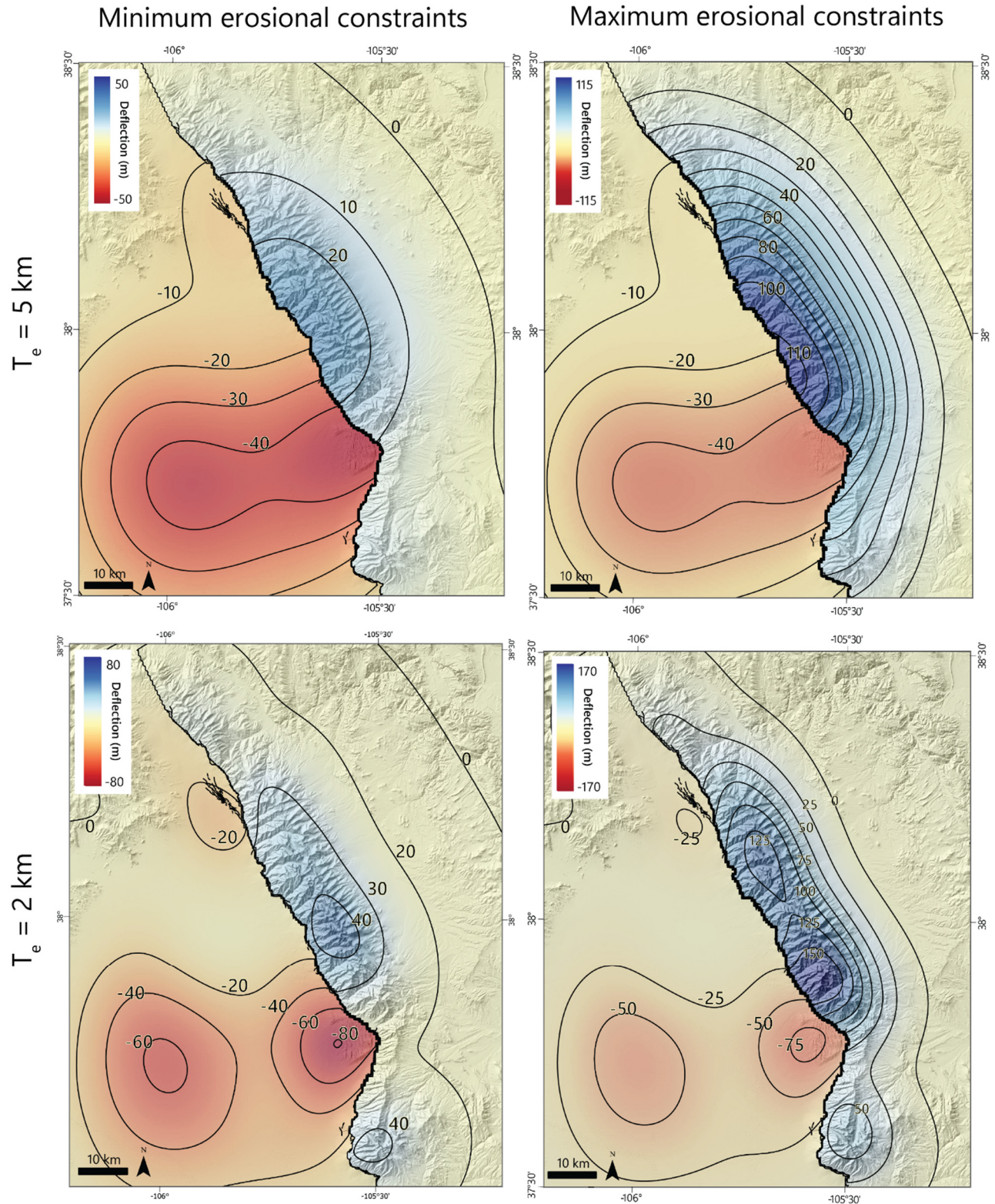


Figure 19. Erosional isostatic rebound results with a  $T_e = 5 \text{ km}$  based on Peterson and Roy (2005) calibrations (top row) and independently calibrated  $T_e = 2 \text{ km}$  (bottom row). Minimum erosional load + depositional load on left and maximum erosional load + depositional load on right. Note that the contour pattern changes with lower rigidity of the lithosphere.

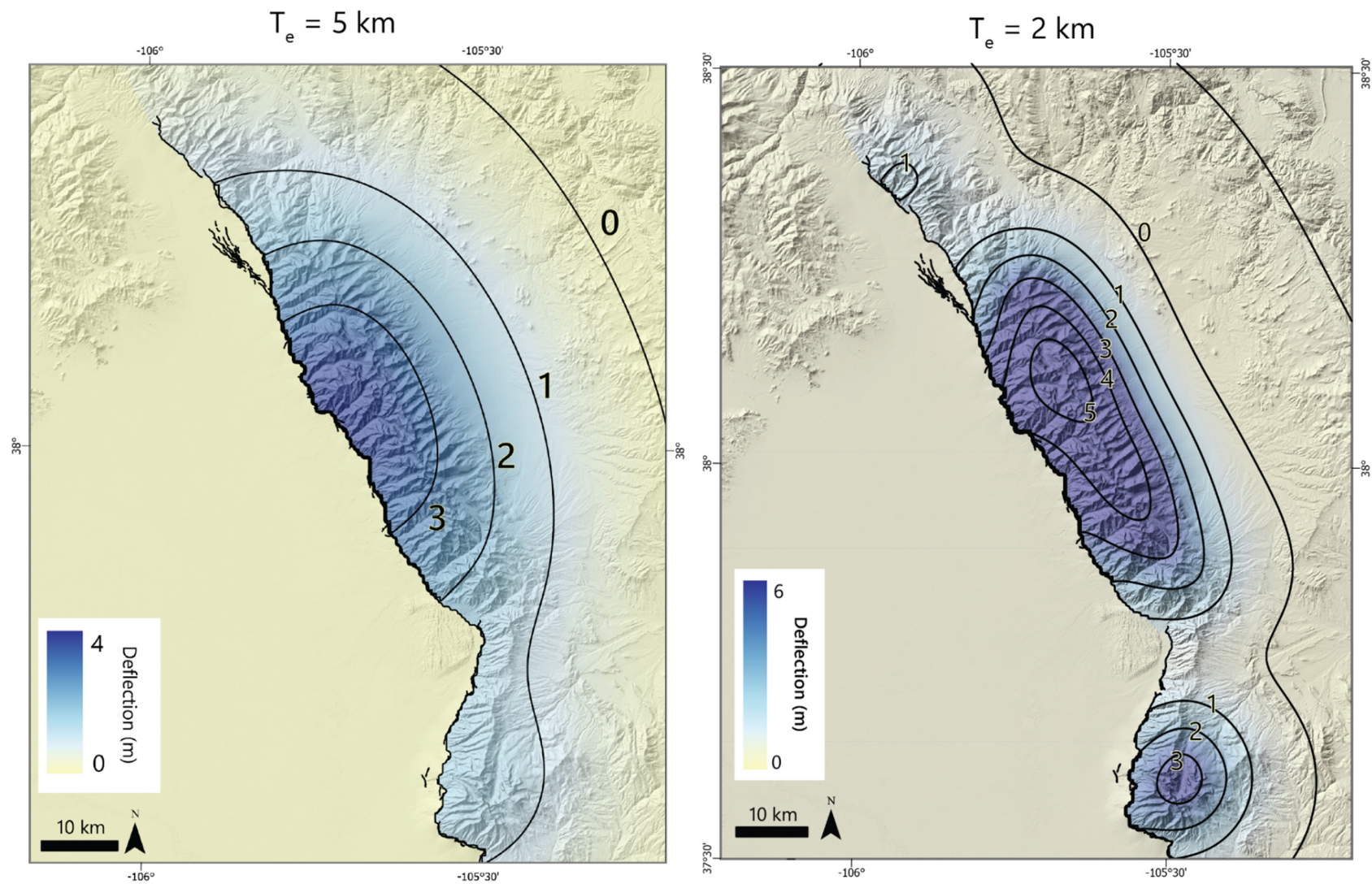


Figure 20. Glacial isostatic rebound results. Left: Isostatic response due glacial load removal in the footwall with an effective elastic thickness of 5 km, reflecting the locally calibrated Peterson and Roy (2005)  $T_e$  estimate. Right: Isostatic response due glacial load removal in the footwall with an effective elastic thickness of 2 km, a conservative estimate of our own attempts to calibrate  $T_e$  through brute force and Bayesian inversion methods.

#### 4.5 Stress modeling

To estimate the stress change at the fault at given depths of 8, 10, and 12 km based on previous Basin and Range earthquake depth estimates and recent seismicity estimates (see discussion in section 2.2), I modeled the stress along a swath perpendicular to the strike of the fault (Figure 21). Using an average estimate of the eroded thicknesses and the approximate distribution of each load, stress changes are significant for each respective load (Table 1). The profile of the stress change displays the stress change at every position along the swath, but the relevant location for this study is at the Sangre de Cristo fault location at depth, indicated with the dotted lines (Figure 21).

Table 1. Stress changes (kPa) of each respective load at 8, 10, and 12 km earthquake nucleation depths.

	Stress change (kPa) of fault for earthquakes at <b>8 km</b> nucleation depth	Stress change (kPa) of fault for earthquakes at <b>10 km</b> nucleation depth	Stress change (kPa) of fault for earthquakes at <b>12 km</b> nucleation depth
Depositional load	37	43	44
Glacial load	2.7	1.5	0.37
Minimum erosional load	25	6.3	15
Maximum erosional load	100	43	13

Table 2. Stress rate (Pa yr<sup>-1</sup>) of each respective load at 8, 10, and 12 km earthquake nucleation depths.

	Stress rate of fault for earthquakes at <b>8 km</b> nucleation depth (Pa yr <sup>-1</sup> )	Stress rate of fault for earthquakes at <b>10 km</b> nucleation depth (Pa yr <sup>-1</sup> )	Stress rate of fault for earthquakes at <b>12 km</b> nucleation depth (Pa yr <sup>-1</sup> )
Depositional load	0.015	0.017	0.018
Glacial load	0.23	0.13	0.032
Minimum erosional load	0.010	0.0025	0.0060
Maximum erosional load	0.040	0.017	0.0052

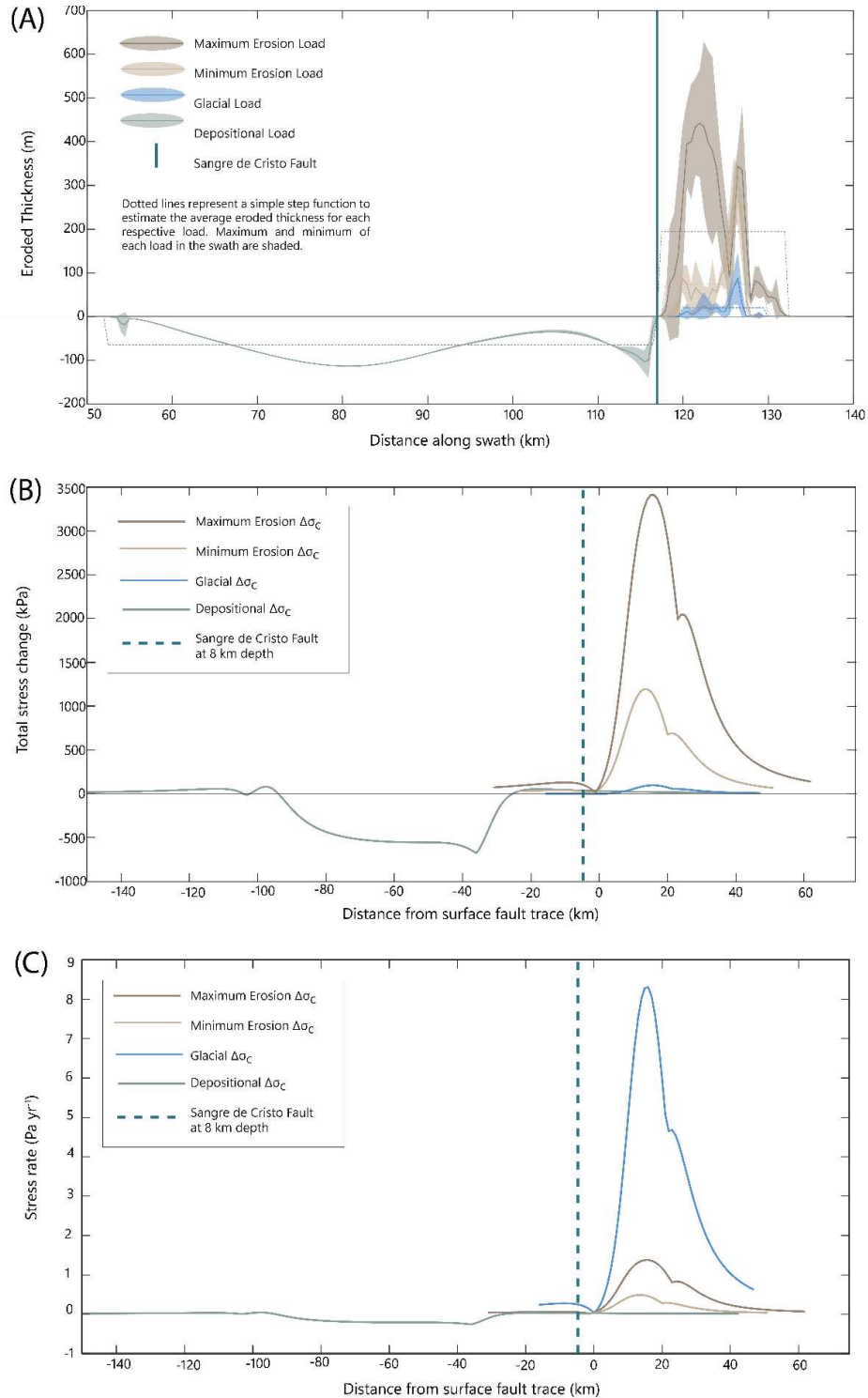


Figure 21. (A) Swath profiles estimating the average eroded thicknesses of the different loads in the system. Average maximum erosion load thickness was approximately 194m, average minimum erosional load thickness was around 73m, average glacial load thickness was approximately 20m, and the depositional load had an average thickness of around -65m. The dotted step-function lines represent the  $h$ -values and  $l$ -values to mimic the stress clamping of the system. (B) Stress changes for 8 km fault depth based on average eroded material. (C) Stress rates for 8 km fault depth. See figure S4 for stress changes and rates for 10 and 12 km fault depths.

#### *4.6 Surface uplift*

The surface uplift results demonstrate that most of the surface uplift occurs near the Sangre de Cristo fault in the unglaciated regions with a maximum of nearly 30 m of positive uplift, and the majority of down drop occurs in the glacially eroded basins near the peaks with a minimum uplift value of approximately  $-690$  m (Figure 22). The drainage divides indicate positive surface uplift in contrast to the basins. A swath profile of the surface uplift shows a pronounced high at the central portion of the range with another subdued high at the Blanca Massif (Figure 22B). Comparing the topographic elevations of the modern and the paleofluvial topography, the mean modern topography lower than the mean paleotopography by an average of 50 m, yet modern peak elevations are several tens of meters higher than the modeled paleopeaks (Figure 22C).

#### *4.7 Mapping, scarp offset, and timing*

The map pattern of the Sangre de Cristo fault has the most prominent scarps occurring within alluvial fans at the outlets of major drainages. Concentrations of fault scarps occurred at the VGFZ that were preferentially preserved in the Qao alluvial fan unit, an area south of Mosca Creek preserved in the Qay alluvial unit, and near Tobin and Blanca creeks on the southern flank of the Blanca Massif. There is a significant gap in the preservation of surface-rupturing fault scarps at the GSDNP area due to the influx of eolian sediment likely covering any remaining fault scarps. There were also gaps in visible fault scarps at the range front where the VGFZ occurred along strike but offset into the valley. The fault appears to have significant spurs, ramps, and relay zones at South Rock Creek, Brook Creek, Hayden Pass Creek, Hot Springs Creek, Wild Cherry Creek, San Isabel Creek, Willow Creek, Spanish Creek, Deadman Creek, around GSDNP, at the Zapata Creeks, and south of Barbara Creek.

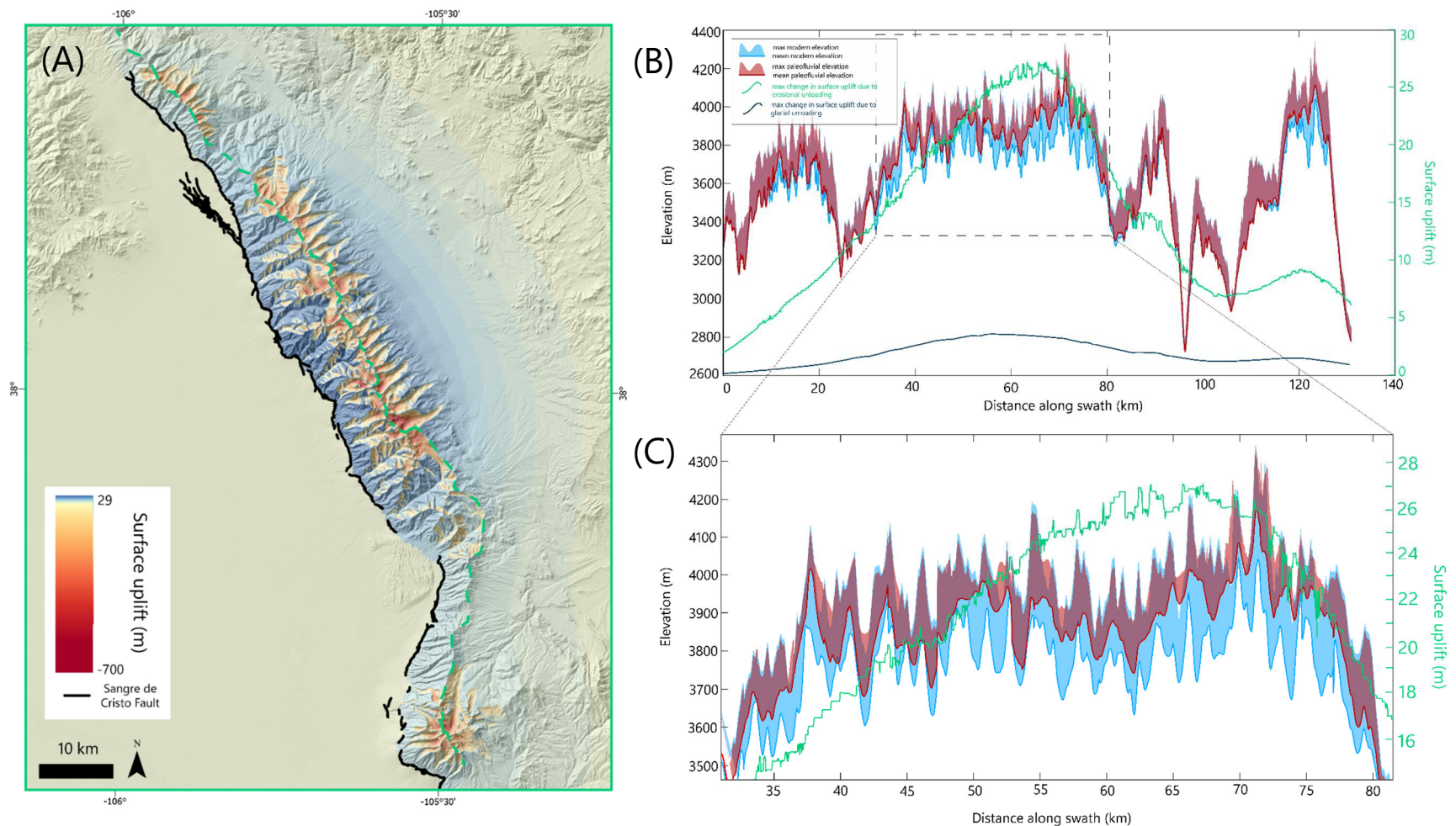


Figure 22. (A) Estimation of surface uplift created by differencing the modern topography from the isostatically-adjusted paleofluvial topographic reconstruction. Swath pattern shown with dotted black line along range divide with dotted green line indicating surface uplift swath in (B) and (C). (B) Topographic swaths showing the modern topography elevation profile in blue and the isostatically-adjusted paleofluvial topographic reconstruction elevation in red, from maps in Figure 17. Thick lines indicate the mean elevations and are shaded up to the maximum elevations. Green line indicates the maximum surface uplift due to the minimum erosional load isostatic response across the same swath, and surface uplift due to the glacial load in dark blue. (C) Zoomed in view of the maximum elevations to show modern peaks surpassing the paleofluvial reconstruction peaks.

Mapping the fault identified 350 potentially measurable portions of the Sangre de Cristo fault to be candidates for offset analysis. Of these, 579 profiles were drawn across these fault portions that were defined as ‘high-quality’ profiles with quality rankings of 4 or 5, and these profiles were distributed across 180 individual fault scarp strands. The total average from the high-quality fault scarps is  $4.58 \text{ m} \pm 3.51 \text{ m}$ . When compared to the pattern of glaciation along-strike (Figure 23a), a distinct difference between the offset in areas of glaciation and those that are in fluvial-only portions of the range is apparent. The glaciated sections appear to have much larger offset magnitudes than the fluvial sections. To confirm whether there is a significant difference in the offsets between these two sections, I performed an unpaired two-sample T-test assuming unequal variances on the offset data. I yielded a P-value  $< 1e^{-4}$ , indicating that the difference in offset magnitude between the glacial and fluvial domains is statistically significant.

To correlate these offsets to a time-averaged fault slip rate, I use the alluvial fan age associations as mapped by Ruleman and Brandt (2021): Holocene (0–11.7 ka), late Pleistocene (11.7 ka–129 ka), mid-Pleistocene (129 ka–774 ka), and early Pleistocene (774 ka–2.58 Ma). The Holocene-associated fault scarps average slip rates of  $0.342 \text{ mm yr}^{-1} \pm 0.192 \text{ mm yr}^{-1}$ , late Pleistocene-associated fault scarps have a mean of  $0.061 \text{ mm yr}^{-1} \pm 0.033 \text{ mm yr}^{-1}$ , middle Pleistocene fault scarps had a mean slip rate of  $0.039 \text{ mm yr}^{-1} \pm 0.032 \text{ mm yr}^{-1}$ , and the early Pleistocene-associated scarps had average slip rates of  $0.0065 \text{ mm yr}^{-1} \pm 0.0051 \text{ mm yr}^{-1}$  (Figure 23B).

## **5. Discussion**

### *5.1 Glacial reconstruction*

Previous researchers have reconstructed glacial extents with field mapping, topographic, geologic, and surficial map examination, satellite imagery observations, and mass-balance flow

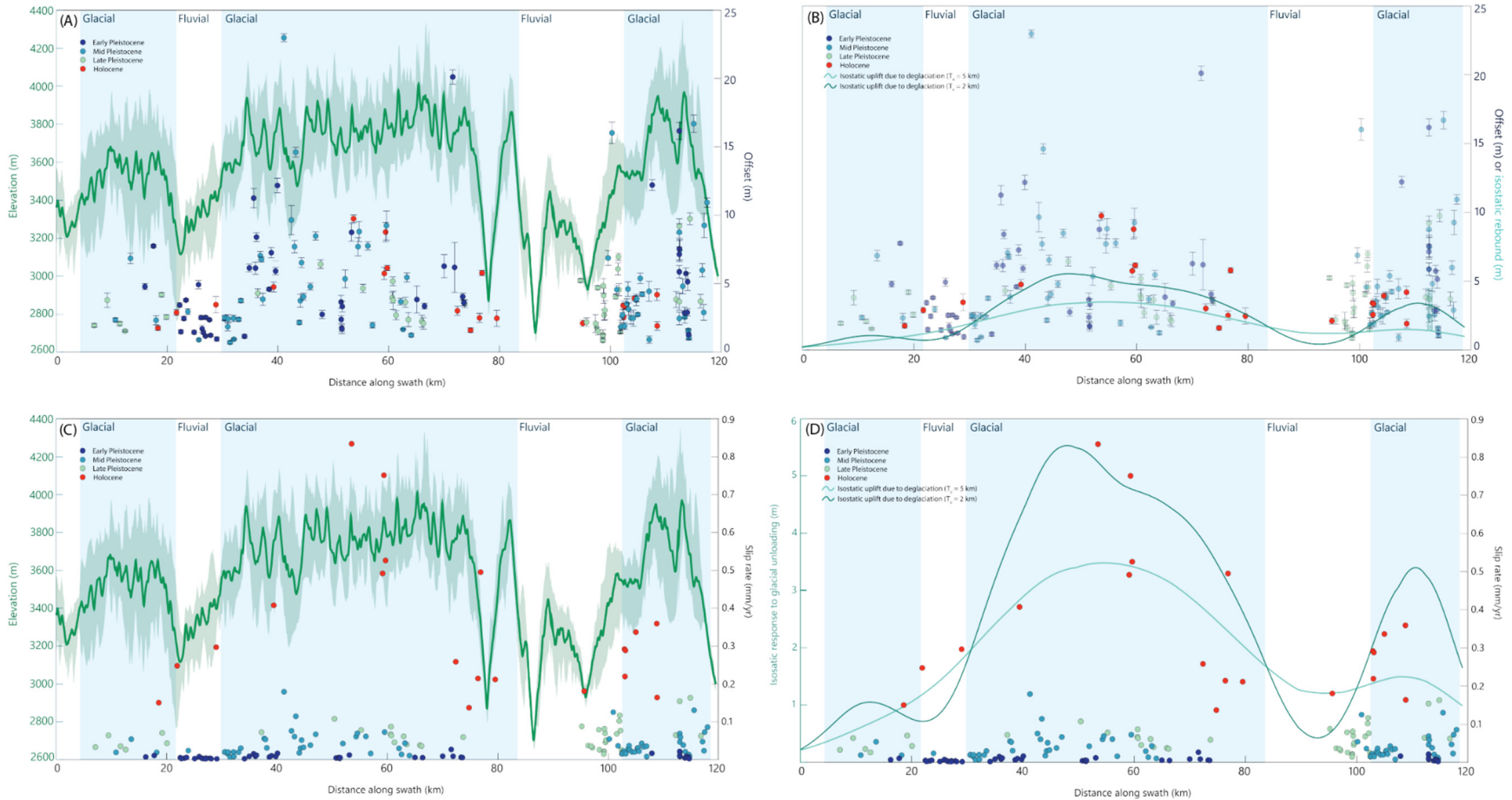


Figure 23. (A) Fault offset measurements with uncertainties plotted along-strike and colored by the associated alluvial fan age. Mean topographic elevations along the divide shown in the background in green, shading indicating maximum and minimum elevations. Glacial and fluvial domains are indicated with the blue and white backgrounds, respectively. (B) Fault slip rates plotted along-strike and colored by the associated alluvial fan age overlain on elevation swath profile. (C) Fault offset measurements with uncertainties overlain on isostatic response signal of deglaciation with  $T_e = 5$  km in light blue and  $T_e = 2$  km in dark blue. (D) Fault slip rates plotted against isostatic response signal of deglaciation with  $T_e = 5$  km in light blue and  $T_e = 2$  km in dark blue. Note that in (D) the focus of the figure is to compare the spatial patterns between slip rates and the isostatic response to deglaciation.

modeling (Refsnider et al., 2009; Leonard et al., 2017; Brugger et al., 2021). In this study, I use a relatively simple approach based on assuming equilibrium with an assumed basal shear stress. This method is limited, not only because of the simplifying assumptions made in the calculations, but also because it relies on the depositional and erosional evidence that has remained after at least 19 kyrs of degradation. There could be erosional or depositional evidence removed by denudation, and the remaining features are not the most accurate representation of the paleoglacial extent. In many cases, this is apparent on the western flank of the range, with only a couple of drainages exhibiting well-preserved terminal moraines. In drainages where these are missing, it was necessary to estimate a potential glacier terminus by a change in the valley morphology from U-shaped to V-shaped, which is less accurate than a preserved glacial deposit. While this is a simple method, it appears that these efforts produce meaningful results when compared to more sophisticated methods used in the Blanca Massif portion of the study area (e.g., Brugger et al., 2021, Figure 24). Importantly, the method I use here is computationally efficient, allowing for reconstructions across broad areas, and yielded the most comprehensive glacial reconstruction for the northern Sangre de Cristo Mountains to date (Figure 16).

As one would expect, the pattern of glaciation correlates to the pattern of elevation along-strike, where glacial domains exist in areas of higher elevation. Additionally, there is an unequivocal difference between the morphology of the eastern glaciers versus the western glaciers (Figure 16). The smaller eastern glaciers have linear channel patterns, with typically only the main trunk or one tributary feeding into the main trunk of the glacier, whereas on the western side of the range, there are larger, convoluted glacier morphologies, often with multiple tributaries. This could be due to the sun angle preferentially melting glaciers that strike west or west-southwest, therefore, glacier heads begin in orientations pointing in orientations with north

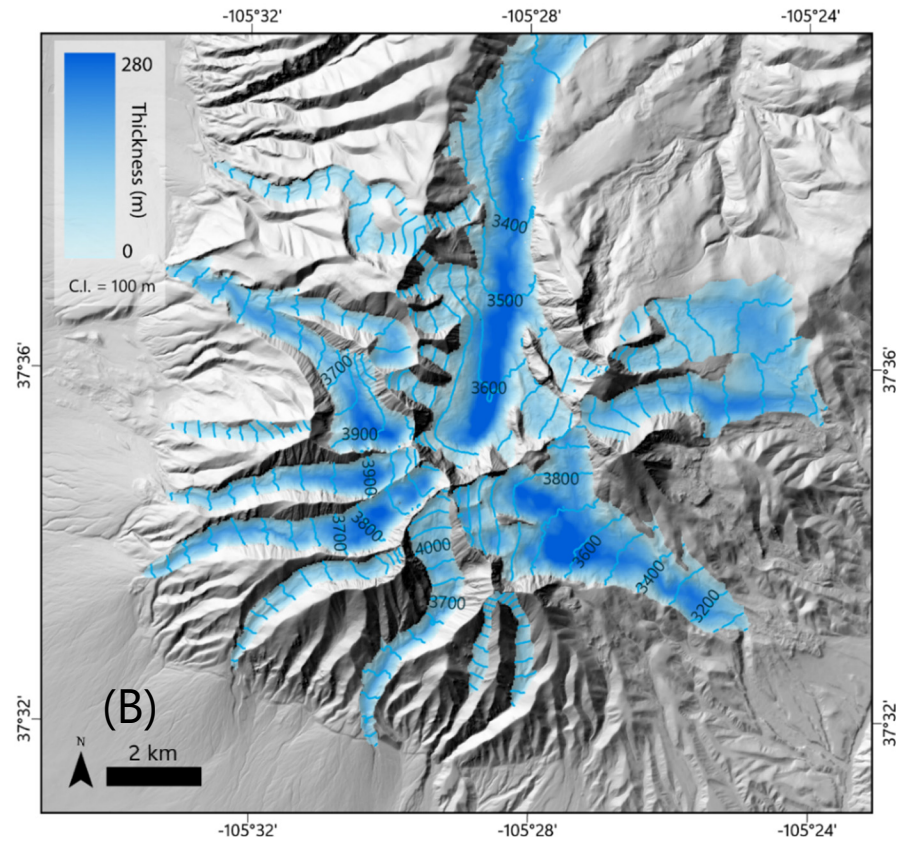
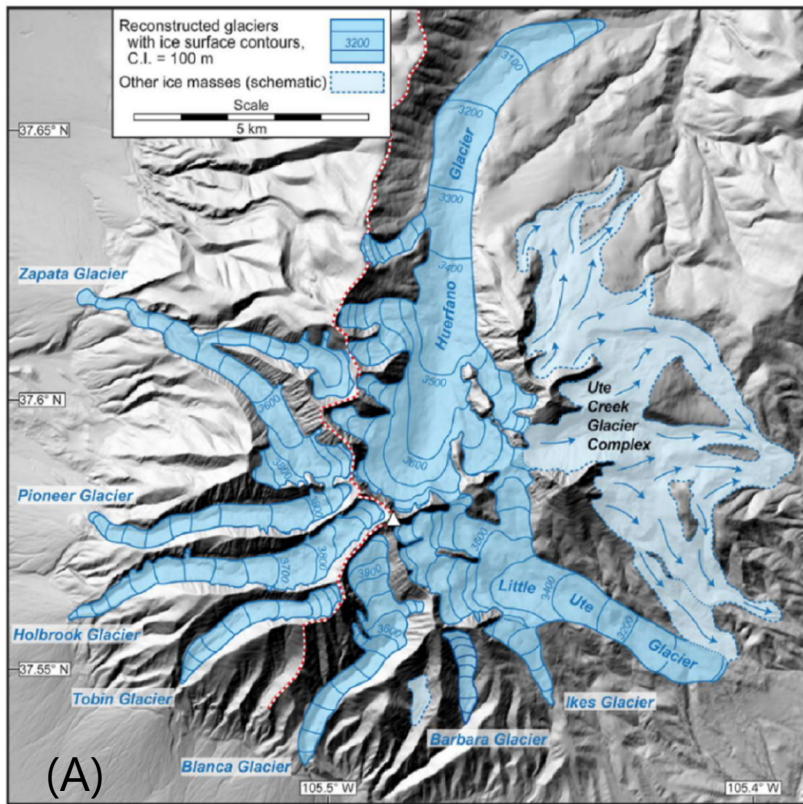


Figure 24. Glacial reconstruction comparison for the Blanca Massif where independent reconstructions are readily available. (A) Brugger et al. (2021) reconstruction using temperature-index modeling and (B) glacial reconstruction from this study using GLaRe.

or east aspects and growing from there (Figure 16). The range strikes NNW-SSE with the eastern side often exhibiting glacier heads that are in the northeasterly aspects, whereas on the western side of the range, any drainage basins that have headwaters with direct southwesterly aspects are void of substantial glacial evidence. Further, Refsnider et al. (2009) also noted that there is a distinct asymmetry in the equilibrium line altitudes (ELAs) between the west and east sides of the range, with systematically lower ELAs on the east, attributing these to precipitation gradients and wind redistribution of snow across the range.

### *5.2 Isostatic response and surface uplift*

Reconstructions of erosional and depositional and glacial ice loads enabled quantification of the flexural isostatic response of the Sangre de Cristo Mountains over two different timescales (Figures 16–20). The flexural response to these various loads is modulated by the effective elastic thickness of the lithosphere. As noted previously, there is some uncertainty about the effective elastic thickness,  $T_e$ , that is appropriate for this location. My independent analysis based on fitting a broken-plate flexural model to the footwall topography yielded a low effective elastic thickness of ~2 km. While a value this low has been reported for normal fault systems in similar ways elsewhere (e.g., Armijo et al., 1996; Goren, 2014; Gallen and Fernández-Blanco, 2021), I consider this to be the lowest possible value for this setting. I additionally test a  $T_e$  of 5 km reported by Peterson and Roy (2005) that was locally calibrated to the San Luis Basin and is more consistent with values they report for other segments of the Rio Grande rift (Peterson and Roy, 2005). I calculate surface uplift based on the 5 km  $T_e$  value to provide a conservative estimate of surface uplift across the range.

The flexural response to glacial erosion and associated deposition are on the order of several tens of meters (Figure 19). The deposition response is generally higher than the erosional

response (Figure 19). This is likely because erosion is only derived from the footwall, but the depositional volumes in my reconstructions include erosion from the Sangre de Cristo Mountains along with other adjacent mountain sources as well as extensive eolian deposition. The flexural isostatic response to reconstructed deglaciation is about an order of magnitude smaller than that of the erosional unloading (Figure 19), but this response is comparable in magnitude to Quaternary fault displacements, which is discussed in detail below. Importantly, the approach used to simulate a broken plate segment by modeling mirrored loads independently across the mapped structure produces a signature consistent with a surface-breaking fault with a discrete offset at the portion of the mapped structure (Figures 19 and 20).

The reconstructed differential erosion and the associated flexural isostatic response were used to calculate surface uplift for the Sangre de Cristo footwall (Figure 22). For this calculation, I use what I think are the most realistic values for  $T_e$  (5 km) and the minimum erosional constraint, which are also conservative in the sense that they result in the smallest amount of surface change in the modeling scenarios I consider in this study. This calculation shows surface uplift associated with differential glacial erosion is at a maximum of 29 m in the footwall, and a maximum lowering of almost 693 m within the glacially-eroded drainage basins in the footwall. Looking at a swath profile of this pattern (Figure 22b, Figure 22c), the mean modern elevation is systematically lower in areas of glaciation than the isostatically-adjusted paleofluvial reconstruction, on average by ~50 m. The peak elevations demonstrate a small but noticeable increase in the maximum elevations at the summits in the modern topography (Figure 22c), with modern peak elevations extending beyond the paleofluvial reconstructions on an ~10 m scale. These observations substantiate the hypothesis of Molnar and England (1990); glacial erosion lowers mean elevations due to preferential valley incision, but peaks rise due to the isostatic

response of the lithosphere. It is important to reemphasize that in this estimation, I only used the minimum erosional load that was calculated, so these estimates should be considered minimum projections of surface uplift, which could be >100 m when considering lower  $T_e$  and higher erosion estimates (e.g., Figure 19).

I consider the flexural response to Holocene deglaciation to largely reflect surface uplift over that timescale (Figure 20). As noted earlier, I acknowledge that this calculation does not include the viscous response of the asthenosphere, so actual magnitudes of isostatic response might be somewhat lower than calculated here. As such, I interpret my results as representing the maximum possible response for the given lithospheric rigidity and ice load. In comparing the isostatic uplift attributed to glaciation to the pattern of Holocene offset along-strike, there is a curious correlation between the two, with a congruent increase until the peak in the central glacial portion of the range, then a decrease in between the central and Blanca portions of the range, then a slight increase in the Blanca portion again. It is not exact, but this spatial similarity does present the possibility that the offset and slip rates strongly reflect the isostatically-induced surface uplift patterns of the range along-strike.

### *5.3 Slip signal of isostatic response to loading and unloading*

Existing tectonics are unequivocally driving the long-term extension, but it is apparent that, based on the results, climate is augmenting this signal. This interpretation is based on the observation that the spatial pattern of Holocene slip, while larger, is of the same order of magnitude and mimics the modeled flexural isostatic response to ice unloading (Figure 23). Furthermore, when considering the time-averaged slip rate of the Sangre de Cristo fault along-strike, there is a pronounced increase in Holocene slip rate, on the scale of an order of magnitude larger than fault slip rates in the time periods preceding the LGM; the Pleistocene rates

calculated here are consistently  $\sim 1e^{-2}$  to  $1e^{-1}$  mm/yr, and the Holocene rates are on the order of  $\sim 1e^{-1}$  to  $1e^0$  mm/yr (Figure 23). As previously stated, these estimates are especially conservative; the inferred timing of the alluvial units to get these rates use the older end of the Holocene and younger ends of the mid and early Pleistocene. This would make these reported rates for the Holocene as slow as possible and make the mid and early Pleistocene rates as fast as possible.

This result is a similar pattern to the modeling work done by Hetzel and Hampel (2005) and Hampel et al. (2007), wherein they observed a period of increased seismic activity in the few thousand years following the removal of a load in the system. I infer that the increased slip rates along the Sangre de Cristo fault system are likely due to the isostatic unloading of the alpine glacial ice, which results in an estimated uplift of  $\sim 4$  m in the footwall block (Figure 20).

Although this is an order of magnitude smaller compared to the almost 30 m response due to the erosional load removal (Figure 19), the post-glacial unloading occurred over a time period ( $\sim 10^4$  yrs) that is two orders of magnitude shorter than the erosional load, which is inferred to integrate erosion over the entirety of the Quaternary ( $\sim 2.6$  Myrs). This is important because as our current climate is changing and glaciers are melting at rapid rates, the removal of these loads can alter the local and regional stress regimes and modulate seismicity at local scales, which is elaborated upon in further detail below. Collectively, these results support the interpretation that the slip rate recently increased on the Sangre de Cristo fault in response to the deglaciation of the footwall. If correct, I infer that the Pleistocene slip rates more accurately represent the long-term slip rate on the fault.

Further support for this interpretation comes from the modeling of changes in clamping stress on the fault as seismic depths due to these changing loads (Figure 21). Regardless of the type of loading or unloading, each either has a negligible effect (i.e., deposition loading of the

hanging wall) or reduces the clamping stress on the fault (i.e., ice unloading) (Figure 21). While this modeling is very simple, it is useful to illustrate that these load changes will promote rather than inhibit slip on the Sangre de Cristo normal fault. Importantly, when considering these changes in clamping stress in terms of rates, ice unloading most rapidly affects clamping stress on the fault (Figure 21, Table 2). This is important because it suggests that the changes in clamping stress on the fault over glacial-interglacial cycles might modulate clamping stress and, by association, slip rate through time. Despite the low-stress changes overall, if a fault system is already in a critically stressed state, which exists here with the active Rio Grande rift system, small changes in the stresses acting on the system could push it into a super- or subcritical state. Further, the rates calculated here (Table 2) are integrated over the entirety of the Holocene (11.7 ka). If the previous studies of Leonard et al. (2017) and Tulenko et al. (2020) are to be considered, then the process of deglaciation would happen over a much shorter period, 2-3 kyrs, which would further increase the rate of stress change due glacial unloading. While speculative, if the fault is close to being critically stressed through time, these small changes in fault clamping stress can elevate and depress fault activity through time.

There exists the possibility that the increase in slip rate with respect to time could be attributed to the Sadler effect; namely, a recency bias wherein more recent sedimentary records register a faster rate of accumulation due to a thinner record as opposed to thicker sections of the sedimentary record which would be integrated across longer time periods (Sadler, 1981). This phenomenon has been observed elsewhere in the natural sciences, from evolutionary biology to tectonics to geomorphology (Gould, 1984; Gardner et al., 1987; Finnegan et al., 2014; Gallen et al., 2015; Harmon et al., 2021). While it is possible that the results could be from a biased record, I think this is unlikely for several reasons. First, the Sadler effect is largely thought to be the

result of an incomplete record with time gaps. In the case of this study, fault scarps represent the cumulative history of fault slip and, absent significant erosion or deposition, represent relatively complete records. Second, it would be a remarkable coincidence that both the temporal and spatial patterns of post-glacial slip are consistent with the timing, patterns, and magnitudes of deglaciation and flexural isostatic rebound (e.g., Figure 23). Third, the changes in post-glacial unloading should act to reduce fault clamping stress, promoting elevated rates of fault slip in the post-glacial period. Finally, in the context of previous studies (Hetzel and Hampel, 2005; Hampel and Hetzel, 2006; Hampel et al., 2007), the post-glacial slip rate increase is expected due to the isostatic rebound of the lithosphere. Within the conceptual model (Figure 3), I anticipate post-glacial slip rate increase to be a likely phenomenon, and while the influence of the Sadler effect could be present here, it is not mutually exclusive with an actual signal of a heightened slip rate during the Holocene.

There could also be an influence of timing on erosion rates: the transition from a fluvial-dominant landscape to a glacial-dominant landscape could cause a pulse of erosion as the topography adjusts morphology to accommodate glaciers (Pederson and Egholm, 2013). Additionally, the transition from the 41 kyr to the 100 kyr Milankovitch cycles around 0.8 to 1 Ma could have influenced a pulse of erosion as well due to the forced change in the pace and size of glaciers (Pederson and Egholm, 2013). Both factors could modulate erosion in this landscape, but regardless of the timing of erosion (whether it is steady or punctuated), the net result would cause a reduction in clamping stress on the fault.

Over the long term, it appears that climate might have an unclamping effect that might result in a longer-term localization of strain, making it easier for the fault to slip. Still, in the

post-glacial timeframe, there is clear evidence that the fault offset mimics the spatial pattern of unloading. The climate could be modulating seismic activity along the fault.

#### *5.4 Glaciers and fault offset – chicken or egg?*

An important question arises when considering the cause and effect of the presence of the glacial domains and the fault offset magnitudes: although they are correlated, which caused the other? An argument can be made for both. My bias entering this work was that the glacial erosion likely caused larger offsets along the fault within their domains due to the larger amount of material being moved from the footwall of the system to the hanging wall, causing a larger imbalance of stresses and therefore accommodating larger offset as a result of that differential stress. Alternatively, it could be argued that the areas of the larger magnitudes of offset accommodated more uplift, thereby lifting those blocks of the footwall above the local ELA and allowing for glaciers to grow given the right climate conditions. In other words, the slip rates in the glaciated segment might be inherently higher and have little to do with the unloading due to glacial erosion and ice melt. It could be that this is the case; however, the stress modeling indicates that the long-term erosion and deposition, in conjunction with the shorter-term ice melting, would reduce clamping stresses on the fault, thereby promoting elevated earthquake activity and slip over the long term, and perhaps localizing strain (e.g., Olive et al., 2014), but resolutely modulate fault slip rates transiently during the post-glacial phase (e.g., Hetzel and Hampel, 2005; Hampel and Hetzel, 2006; Hampel et al., 2007). Additionally, the pattern of post-glacial slip is incredibly spatially consistent with the ice-unloading signal (Figure 23). It would be a remarkable coincidence if the two were not related in space and time but reflected each other so precisely.

If the hypothesis is that the glaciation happened first, it could be expected that the offset patterns correlate to the areas of glaciation due to the greater differential stresses caused by erosional unloading, which is reflected in the topography and offset measurements. Further, one study by Watkins (1996) noted that drill cores along the range front Sangre de Cristo fault near Deadman Creek only show ~60 m of offset, comparable to our isostatic rebound estimates associated with glacial erosion and deposition (Figure 19). It could be possible, based on this work, that the modern expression of the range front strands of the fault are solely accounting for glacial erosion and deglaciation due to the localization of strain at the range front. However, not all studies done in this area have the same interpretation of the subsurface, so this interpretation is highly speculative. Based on the temporal and spatial consistencies between offset and modeled isostatic response and the outputs of the stress modeling, there is an unclamping effect on the fault that is modulated by glacial unloading. Over the long term, the onset of glaciation in this area and differential erosion and deposition would promote conditions that would facilitate fault slip over long timescales. While it is true that glaciers are in these locations because the time-integrated slip must have been higher, this does not preclude climate from having an effect on modulating the fault and how it is slipping through time.

### *5.5 Study implications*

This study shows that it is indeed possible for differential glacial erosion to drive uplift of mountain peaks (e.g., Molnar and England, 1990), but also promotes surface uplift of areas that experience little to no erosion (Figure 22A). Nonetheless, this response is subtle and unlikely to strongly affect glacial mass balance over the long term, as hypothesized by Molnar and England (1990).

As our climate continues to warm at rates much faster than previously observed, we must consider the effect that this has on earth systems, including seismic activity on fault systems. Anthropogenically-induced climate change and anthropogenic activity are affecting the global hydrological cycle and, thus, surface loading of potentially seismic structures (Amos et al., 2014; Johnson et al., 2017; Carlson et al., 2020). Because glaciers and ice sheets are susceptible to significant change from even small temperature increases or seasonality changes, the melting of these glaciers and the subsequent mass loss could result in a marked change in the stresses acting on fault systems in glaciated (and soon to be deglaciated) areas. With glacier retreat hastening due to anthropogenic-driven warming of the atmosphere over the past 70 years and predicting further acceleration to glacial melt (Huss and Hock, 2015; Hock et al., 2019; Hugonnet et al., 2021; Rounce et al., 2023), it is critical that we bolster our understanding of how we are changing local stress regimes and the possibility that we could be potentially increasing seismicity in tandem. Seismic slip events could be considered hazards associated with deglaciation due to the consequential melt rates within our lifetime. More generally, changes in water or ice loads that reflect both climate change and human water extraction need to be considered as mechanisms for evolving seismic hazard levels along faults (e.g., Amos et al., 2014; Johnson et al., 2017; Carlson et al., 2020).

### *5.6 Future work*

This research highlights a number of useful research directions to better understand the Sangre de Cristo fault system and associated seismic hazard. Further work could be done to map the alluvial fans more precisely and obtain better absolute and relative ages for the fan units. The 1:75,000 mapping scale of the Ruleman and Brandt (2021) is much coarser than my fault mapping scale of 1:4,400; therefore, improvements could be made at the map scale to ensure that

the alluvial fan ages are correctly dated to their appropriate time to limit the rather unconstrained uncertainties that exist in my slip rate estimates. Using a surface roughness method and associating those with more precisely mapped alluvial fans, for example, from Nicovich and Schmitt (2017), one could test varying wavelengths of roughness and a maximum likelihood classification to remotely map a more precise age of the alluvial fans at the range front. Alternatively, field mapping and sampling could be done in tandem to further constrain the ages using geochronological techniques such as luminescence geochronology and cosmogenic radionuclides. Enhancing the precision of the ages of the alluvial units could augment the understanding of the relationship between fault slip and relation to glacial periods and would bolster conclusions regarding fault slip and previous periods of glaciation.

The correlation between offset magnitudes and glaciation could be further explored in other regions of areas with climate-related loads, such as former ice sheets, lakes, and glaciers proximal to normal faults, to determine whether changes in ice loads temporally modulate fault slip rates. Examples of areas of application could be the Bitterroot Mountains in Montana, the Sierra Nevada Mountains in California, and the Lemhi Range in Idaho. Investigating additional areas with similar stress regimes and structures is important, as seismic activity due to glacial melt could become another hazard associated with anthropogenic climate change.

## **6. Conclusions**

This study finds that the northern Sangre de Cristo Mountains have experienced significant differential glacial erosion due to alpine glaciation that promoted large changes in topography, substantiating the work of Molnar and England (1990). These topographic changes reduced mean elevations by ~50 m via glacial erosion, and generated peak uplift on a relatively more minor scale,  $\leq 10$  m, due to the isostatic response to erosion.

Additionally, as part of the flexural modeling, this study produces the most comprehensive glacial reconstruction in the area, with techniques not previously utilized in the Sangre de Cristo Mountains. Although these reconstructions are completed through different, simpler means than previous methodologies, the results of the reconstructions are comparable to work done by Refsnider et al. (2009), Leonard et al. (2017), and Brugger et al. (2021) and build on the previous work done by these researchers.

Stress modeling of the various loads demonstrates net unclamping of the normal fault system at depth, which likely encouraged fault slip over longer ( $10^5 - 10^6$  yr) time periods, and increased fault slip on shorter ( $10^3 - 10^4$  yr), glacial time periods, with a distinct spatial correlation between glaciated regions within the Sangre de Cristo Mountains and magnitude of offset along the Sangre de Cristo fault. Based on the assessment of the data produced from this work, there lies the likelihood that climate is contributing to the sustained activity of the fault. It appears more conclusive that deglaciation has had a substantial influence on slip on this structure. Applying these methods to additional areas with both active and ancient faults could prove to be informative, as these perturbations associated with climate change could result in sustained increases in seismic activity. As our climate continues to warm at rates orders of magnitude faster than any point in geologic history, it is imperative that we consider the effect that this has on fault systems. This work demonstrates that the dissipation of surface loads such as glaciers, ice sheets, and lakes that can and will dematerialize due to our warming climate, and the corresponding changes in stress due to the mass change, could modulate seismicity in active fault systems within our lifetime.

## References

- Abbey, A. L., Niemi, N. A., 2018, Low-temperature thermochronometric constraints on fault initiation and growth in the northern Rio Grande rift, upper Arkansas River valley, Colorado, USA: *Geology*, v. 46, p. 627–630. doi.org/10.1130/G40232.1
- Abbey, A. L., Niemi, N. A., 2020, Perspectives on Continental Rifting Processes From Spatiotemporal Patterns of Faulting and Magmatism in the Rio Grande rift, USA: *Tectonics*, v. 39, p. 1-31. doi.org/10.1029/2019TC005635
- Amos, C.B., Audet, P., Hammond, W.C., Bürgmann, R., Johanson, I.A. and Blewitt, G., 2014, Uplift and seismicity driven by groundwater depletion in central California: *Nature*, v. 509, p.483-486.
- Armijo, R., Meyer, B.G.C.P., King, G.C.P., Rigo, A. and Papanastassiou, D., 1996, Quaternary evolution of the Corinth Rift and its implications for the Late Cenozoic evolution of the Aegean: *Geophysical Journal International*, v. 126, p.11-53.
- Bell, J., 2020, Seismic Activity in the Northern Sangre de Cristo Fault Zone [M.S. thesis]: University of Colorado, Boulder, 61 p.
- Benn, D. I., & Hulton, N. R. J., 2010, An Excel (TM) spreadsheet program for reconstructing the surface profile of former mountain glaciers and ice caps: *Computers & Geosciences*, v. 36, p. 605-610. <https://doi.org/10.1016/j.cageo.2009.09.016>
- Bennett and Glasser, 2010, *Glacial Geology: Ice Sheets and Landforms*, 2nd Edition, Wiley Blackwell, 400 pp.
- Brister, B. S., and Gries, R. R., 1994, Tertiary stratigraphy and tectonic development of the Alamosa basin (northern San Luis Basin), Rio Grande rift, south-central Colorado, *in* G. R. Keller & S. M. Cather (Eds.), *Basins of the Rio Grande rift: Structure, Stratigraphy, and Tectonic Setting* (Vol. 291, p. 39-58). Geological Society of America. <https://doi.org/10.1130/SPE291-p39>
- Brocklehurst, S. H., and Whipple, K. X., 2006, Assessing the relative efficiency of fluvial and glacial erosion through simulation of fluvial landscapes: *Geomorphology*, v. 75, p. 283-299, doi:10.1016/j.geomorph.2005.07.028
- Brugger, K. A., Leonard, E. M., Refsnider, K. A., and Dolan, P., 2021, Climate on the Blanca Massif, Sangre de Cristo Mountains, Colorado, USA, during the Last Glacial Maximum: *Quaternary*, v. 4, 27 pp., <https://doi.org/10.3390/quat4030027>
- Bush, M. A., Horton, B. K., Murphy, M. A., & Stockli, D. F., 2016, Detrital record of initial basement exhumation along the Laramide deformation front, southern Rocky Mountains: *Tectonics*, v. 35, p. 2117–2130, <https://doi.org/10.1002/2016TC004194>

- Burbank, D.W., and Anderson, R.S., 2012, *Tectonic geomorphology*, Second Edition: John Wiley & Sons.
- Byerlee, J., 1978, Friction of rocks: *Pure and Applied Geophysics*, v. 116, p. 615–626.  
<https://doi.org/10.1007/BF00876528>
- Calais, E., Freed, A. M., Van Arsdale, R., & Stein, S., 2010, Triggering of New Madrid seismicity by late-Pleistocene erosion: *Nature*, v. 466, p. 608-611,  
<https://doi.org/10.1038/nature09258>
- Cather, S., 2004, Laramide orogeny in central and northern New Mexico and southern Colorado. *The Geology of New Mexico: A Geologic History*, v. 11, p. 203–248.
- Carlson, G., Shirzaei, M., Werth, S., Zhai, G. and Ojha, C., 2020, Seasonal and long-term groundwater unloading in the Central Valley modifies crustal stress: *Journal of Geophysical Research: Solid Earth*, v. 125(1), p.e2019JB018490.
- Caves, J.K., Sjostrom, D.J., Mix, H.T., Winnick, M.J. and Chamberlain, C.P., 2014, Aridification of Central Asia and uplift of the Altai and Hangay Mountains, Mongolia: Stable isotope evidence: *American Journal of Science*, v. 314, p.1171-1201.
- Champagnac, J.D., Anderson, R., Delacou, B., Molnar, P. and Sue, C., 2007, Pliocene isostatic rebound of the Western Alps inferred from topographic analysis and sediment budget: *Geology*, v. 35, p.195-198.
- Davis, J. K., Hudson, M. R., Grauch, V. J. S., 2017, A paleomagnetic age estimate for the draining of ancient Lake Alamosa, San Luis Valley, south-central Colorado, U.S.A.: *Rocky Mountain Geology*, v. 52, no. 2., p. 107-117, doi:10.24872/rmgjournal.52.2.107
- DiBiase, R.A., Whipple, K.X., Heimsath, A.M., and Ouimet, W.B., 2010, Landscape form and millennial erosion rates in the San Gabriel Mountains, CA: *Earth and Planetary Science Letters*, v. 289, p.134–144, doi:10.1016/j.epsl.2009.10.036.
- Doser, D.I., and Smith, R.B., 1989, An assessment of source parameters of earthquakes in the cordillera of the western United States: *Bulletin of the Seismological Society of America*, v. 79, no. 5, p. 1383–1409.
- Erslev, A. E., and Koenig, N. V., 2009, Three-dimensional kinematics of Laramide, basement-involved Rocky Mountain deformation, USA: Insights from minor faults and GIS-enhanced structure maps, *Geol. Soc. Am. Mem.*, v. 204, p. 125–150.  
[doi.org/10.1130/2009.1204\(06\)](https://doi.org/10.1130/2009.1204(06))
- Finnegan, N.J., Schumer, R. and Finnegan, S., 2014, A signature of transience in bedrock river incision rates over timescales of 104–107 years: *Nature*, v. 505, p.391-394.
- Flint, J.J., 1974, Stream gradient as a function of order, magnitude, and discharge: *Water*

- Resources, Research, v. 10, p. 969–973, doi:10.1029/WR010i005p00969.
- Foster, D., Brocklehurst, S. H. and Gawthorpe, R. L., 2010, Glacial-topographic interactions in the Teton Range, Wyoming: *J. Geophys. Res.*, v. 115, F01007, doi:10.1029/2008JF001135.
- Gallen, S.F. and Fernández-Blanco, D., 2021, A new data-driven Bayesian inversion of fluvial topography clarifies the tectonic history of the Corinth rift and reveals a channel steepness threshold: *Journal of Geophysical Research: Earth Surface*, v. 126(3), p.e2020JF005651.
- Gallen, S.F., Pazzaglia, F.J., Wegmann, K.W., Pederson, J.L. and Gardner, T.W., 2015, The dynamic reference frame of rivers and apparent transience in incision rates: *Geology*, v. 43(7), p.623-626.
- Gallen, S. F. and Thigpen, J. R., 2018, Lithologic Controls on Focused Erosion and Intraplate Earthquakes in the Eastern Tennessee Seismic Zone: *Geophysical Research Letters*, v. 45, p. 9569–9578. <https://doi.org/10.1029/2018GL079157>
- Gallen, S. F. and Wegmann, K. W., 2017, River profile response to normal fault growth and linkage: an example from the Hellenic forearc of south-central Crete, Greece: *Earth Surface Dynamics*, v. 5, p. 161-186, doi: 10.5194/esurf-5-161-2017
- Gardner, T.W., Jorgensen, D.W., Shuman, C. and Lemieux, C.R., 1987, Geomorphic and tectonic process rates: Effects of measured time interval: *Geology*, v. 15(3), pp.259-261.
- Ghamed, O., Singleton, J., Sitar, M., Rahl, J., Wong, M., O'Sullivan, P., Hurtado, C., and Malavarca, S., 2023, Refining the pre- and syn-Rio Grande rift cooling history across the Sangre de Cristo Range and Alvarado fault through application of mid- to low-temperature thermochronometry: *GSA Rocky Mountain Section Meeting*
- Goren, L., Fox, M. and Willett, S.D., 2014, Tectonics from fluvial topography using formal linear inversion: Theory and applications to the Inyo Mountains, California: *Journal of Geophysical Research: Earth Surface*, v. 119(8), p. 1651-1681.
- Gould, S.J., 1984, Smooth curve of evolutionary rate: a psychological and mathematical artifact: *Science*, v. 226(4677), p. 994-996.
- Grauch, V.J.S., and Ruleman, C.A., 2013, Identifying Buried Segments of Active Faults in the Northern Rio Grande rift Using Aeromagnetic, LiDAR, and Gravity Data, South-Central Colorado, USA: *International Journal of Geophysics*, v. 2013, 26 pp.
- Hampel, A., and Hetzel, R., 2006, Response of normal faults to glacial-interglacial fluctuations of ice and water masses on Earth's surface: *Journal of Geophysical Research*, v. 111, doi:10.1029/2005JB004124.

- Harmon, L.J., Pennell, M.W., Henao-Diaz, L.F., Rolland, J., Siple, B.N. and Uyeda, J.C., 2021, Causes and consequences of apparent timescaling across all estimated evolutionary rates: *Annual Review of Ecology, Evolution, and Systematics*, 52, p.587-609.
- Hetzl, R., and Hampel, A., 2005, Slip rate variations on normal faults during glacial-interglacial changes in surface loads: *Nature*, v. 435, p. 81-83
- Hampel, A., Hetzel, R., and Densmore, A. L., 2007, Postglacial slip-rate increase on the Teton normal fault, northern Basin and Range Province, caused by melting of the Yellowstone ice cap and deglaciation of the Teton Range?: *Geology*, v. 35, p. 1107–1110, doi: 10.1130/G24093A.1.
- Hock, R., Bliss, A., Marzeion, B., Giesen, R.H., Hirabayashi, Y., Huss, M., Radic, V., and Slangen, A.B.A., 2019, GlacierMIP – A model intercomparison of global-scale glacier mass-balance models and projections. *J. Glaciol.*, v. 65, p. 453–467, doi:10.1017/jog.2019.22
- Howard, A.D., 1994, A detachment-limited model of drainage basin evolution: *Water Resources Research*, v. 30, p. 2261–2285, doi:10.1029/94WR00757.
- Hoy, R. G., and Ridgway, K. D., 2002, Syndepositional thrust-related deformation and sedimentation in an Ancestral Rocky Mountains basin, Central Colorado trough, Colorado, USA: *GSA Bulletin*, 114(7), 804–828. [https://doi.org/10.1130/0016-7606\(2002\)114<0804:STRDAS>2.0.CO;2](https://doi.org/10.1130/0016-7606(2002)114<0804:STRDAS>2.0.CO;2)
- Hugonnet, R., McNabb, R., Berthier, E., Menounos, B., Nuth, C., Girod, L., Farinotti, D., Huss, M., Dussaillant, I., Brun, F., and Kääb, A., 2021, Accelerated global glacier mass loss in the early twenty-first century: *Nature*, v. 592 p. 726–731, doi:10.1038/s41586-021-03436-z
- Humphreys, E., 1995, Post-Laramide removal of the Farallon slab, western United States: *Geology*, v. 23, p. 987-990, doi.org/10.1130/0091-7613(1995)023<0987:PLROTF>2.3.CO;2
- Humphreys, E., 2009, Relation of flat slab subduction to magmatism and deformation in the western United States, *in* Kay, S.M., Ramos, V.A., and Dickinson, W.R., eds., *Backbone of the Americas: Shallow Subduction, Plateau Uplift, and Ridge and Terrane Collision*: Geological Society of America Memoir 204, p. 85–98, doi:10.1130/2009.1204(04).
- Humphreys, E., Hessler, E., Dueker, K., Erslev, E., Farmer, G.L., and Atwater, T., 2003, How Laramide-age hydration of North America by the Farallon slab controlled subsequent activity in the western U.S.: *International Geology Review*, v. 45, p. 575–595, doi:10.2747/0020-6814.45.7.575
- Huss, M., and Hock, R., 2015, A new model for global glacier change and sea-level rise. *Front. Earth Sci.* 3, doi:10.3389/feart.2015.00054

- Jaeger, J. C., Cook, N. G., & Zimmerman, R., 2009, Fundamentals of rock mechanics (p. 488). Malden, MA: John Wiley.
- Jiskoot, H., 2011, Dynamics of Glaciers, *in*: Singh, V.P., Singh, P., Haritashya, U.K. (eds) Encyclopedia of Snow, Ice and Glaciers. Encyclopedia of Earth Sciences Series. Springer, Dordrecht. [https://doi.org/10.1007/978-90-481-2642-2\\_127](https://doi.org/10.1007/978-90-481-2642-2_127)
- Johnson, C.W., Fu, Y. and Bürgmann, R., 2017. Seasonal water storage, stress modulation, and California seismicity. *Science*, v. 356, pp.1161-1164.
- Kirby, E., and Whipple, K.X., 2012, Expression of active tectonics in erosional landscapes: *Journal of Structural Geology*, v. 44, p. 54–75, doi:10.1016/j.jsg.2012.07.009.
- Kluth, C.F., and Schaftenaar, C.H., 1994, Depth and geometry of the northern Rio Grande rift in the San Luis Basin, south-central Colorado, in Keller, G.R., and Cather, S.M., eds., Basins of the Rio Grande rift—Structure, stratigraphy, and tectonic setting: Geological Society of America Special Paper 291, p. 27-37.
- Lathrop, B. A., Jackson, C. A-L., Bell, R. E., and Rotevatn, A., 2022, Displacement/Length Scaling Relationships for Normal Faults; a Review, Critique, and Revised Compilation. *Front. Earth Sci.* v. 10, 23 pp. doi: 10.3389/feart.2022.907543
- Leonard, E. M., Laabs, B. J. C., Plummer, M. A., Kroner, R. K., Brugger, K. A., Spiess, V. M., Refsnider, K. A., Xia, Y., Caffee, M. W., 2017, Late Pleistocene glaciation and deglaciation in the Crestone Peaks area, Colorado Sangre de Cristo Mountains, USA – chronology and paleoclimate: *Quaternary Science Reviews*, v. 158, p. 127-144, <http://dx.doi.org/10.1016/j.quascirev.2016.11.024>
- Lindsey, D. A., 1998, Laramide structure of the central Sangre de Cristo Mountains and adjacent Raton Basin, southern Colorado: *Mountain Geologist*, v. 35, p. 55–70. USGS Publications Warehouse.
- Lindsey, D.A., 2010, The geologic story of Colorado’s Sangre de Cristo Range: U.S. Geological Survey Circular 1349, 14 p.
- Lindsey, D. A., Andriessen, P. A. M., and Wardlaw, B. R., 1986, Heating, cooling, and uplift during Tertiary time, northern Sangre de Cristo Range, Colorado: *Geological Society of America Bulletin*, v. 97, p. 1133-1143. doi: [https://doi.org/10.1130/0016-7606\(1986\)97<1133:HCAUDT>2.0.CO;2](https://doi.org/10.1130/0016-7606(1986)97<1133:HCAUDT>2.0.CO;2)
- Lindsey, D.A., Johnson, B. R., Soulliere, S.J., Bruce, R. M., and Hafner, K., 1986, Geologic Map of the Beck Mountain, Crestone Peak, and Crestone Quadrangles, Custer, Huerfano, and Saguache Counties, Colorado: U.S. Geological Survey Miscellaneous Field Studies Map MF-1878, scale 1:24,000.
- Lindsey, D.A., and Soulliere, S.J., 1987, Geologic Map and Sections of the Valley View Hot

- Springs Quadrangle, Custer and Saguache Counties, Colorado: U.S. Geological Survey Miscellaneous Field Studies Map MF-1942, scale 1:24,000.
- Lindsey, D.A., Soulliere, Hafner, K., and Flores, R. J., 1985, Geologic Map of the Rito Alto Peak and Northeastern Part of Mirage Quadrangles, Custer and Saguache Counties, Colorado: U.S. Geological Survey Miscellaneous Field Studies Map MF-1787, scale 1:24,000.
- Lipman, P. W., 1989, Oligocene–Miocene San Juan volcanic field, Colorado. In C. E. Chapin & J. Zidek, Field excursions to volcanic terranes in the western United States, Volume I: Southern Rocky Mountain Region. New Mexico Bureau of Geology & Mineral Resources.
- Machette, M. N., 2000, Active, capable, and potentially active faults – a paleoseismic perspective: *Journal of Geodynamics*, v. 29, p. 387-392
- Machette, M.N., Coates, M-M., and Johnson, M.L., 2007, Rocky Mountain Section Friends of the Pleistocene Field Trip–Quaternary geology of the San Luis Basin of Colorado and New Mexico, September 7–9, 2007: U.S. Geological Survey Open-File Report 2007–1193, 197 p.
- Machette, M. N., Thompson, R. A., Machetti, D. W., Smith, R. S. U., 2013, Evolution of ancient Lake Alamosa and integration of the Rio Grande during the Pliocene and Pleistocene, *in* Hudson, M. R., and Grauch, V. J. S., eds., *New Perspectives on Rio Grande rift Basins: From Tectonics to Groundwater: Geological Society of America Special Paper 494*, p. 1-20, doi:10.1130/2013.2494(01)
- McCalpin, J. P., 1982, Quaternary geology and neotectonics of the west flank of the northern Sangre de Cristo Mountains, south-central Colorado: *Colorado School of Mines Quarterly*, v. 77.
- McCalpin, J.P., and Kirkham, R.M., 2006, Refine slip rates and segmentation of the Northern Sangre de Cristo fault, Colorado's largest active fault: Technical report to U.S. Geological Survey, Reston, Virginia, under Contract 03HQGR0076, 42 p., <http://earthquake.usgs.gov/research/external/reports/03HQGR0076.pdf>.
- McCalpin, J. P., Harrison, L. B. J., Berger, G. W., & Tobin, H., 2011, Paleoseismicity of a low-slip-rate normal fault in the Rio Grande rift, USA: The Calabacillas fault, Albuquerque, New Mexico. *Geological Society of America Special Papers*, v. 479, p. 23–46. [https://doi.org/10.1130/2011.2479\(01\)](https://doi.org/10.1130/2011.2479(01))
- McIntosh, W. C., and Chapin, C. E., 2004, Geochronology of the central Colorado volcanic field: *New Mexico Bureau of Geology & Mineral Resources, Bulletin 160*, p. 205-237
- Mey, J., Scherler, D., Wickert, A. D., Egholm, D. L., Tesauro, M., Schildgen, T.F., and Strecker,

- M. R., 2016, Glacial isostatic uplift of the European Alps: *Nature Communications*. v. 7:13382, p. 1-9, doi:10.1038/ncomms13382
- Molnar, P., and England, P., 1990, Late Cenozoic uplift of mountain ranges and global climate change: chicken or egg?: *Nature*, v. 346, p. 29-34, <https://doi.org/10.1038/346029a0>
- Murray, K. D., Murray, M. H., & Sheehan, A. F., 2019, Active deformation near the Rio Grande Rift and Colorado Plateau as inferred from continuous Global Positioning System measurements. *Journal of Geophysical Research: Solid Earth*, v. 124, p. 2166–2183. <https://doi.org/10.1029/2018JB016626>
- Nicovich, S.R., and Schmitt, J.G., 2017, Geological mapping of the Zapata and Blanca sections of the northern Sangre de Cristo range-front fault system, south-central Colorado: NCGMP EDMAP Program, scale: 1:24,000, [https://ngmdb.usgs.gov/Prodesc/proddesc\\_109694.htm](https://ngmdb.usgs.gov/Prodesc/proddesc_109694.htm)
- Olive, J.A., Behn, M.D. and Malatesta, L.C., 2014. Modes of extensional faulting controlled by surface processes. *Geophysical Research Letters*, v. 41(19), p. 6725-6733.
- Paxman, G.J.G., Watts, A.B., Ferraccioli, F., Jordan, T.A., Bell, R.E., Jamieson, S.S.R. and Finn, C.A., 2016. Erosion-driven uplift in the Gamburtsev Subglacial Mountains of East Antarctica. *Earth and Planetary Science Letters*, 452, pp.1-14.
- Pedersen, V.K. and Egholm, D.L., 2013. Glaciations in response to climate variations preconditioned by evolving topography. *Nature*, v. 493(7431), pp.206-210.
- Pellitero, R., Rea, B. R., Spagnolo, M., Bakke, J., Ivy-Ochs, S., Frew, C. R., Hughes, P., Ribolini, A., Lukas, S., Renssen, H., 2016, GlaRe, a GIS tool to reconstruct the 3D surface of palaeoglaciers: *Computers & Geosciences*, v. 94, p.77-85, <http://dx.doi.org/10.1016/j.cageo.2016.06.008>
- Perron, J.T., Royden, L. 2013, An integral approach to bedrock river profile analysis: *Earth Surface Processes and Landforms*, v. 38, p. 570–576, doi:10.1002/esp.3302.
- Personius, S. F., Machette, M. N., & Kelson, K. I., 1999, Quaternary faults in the Albuquerque area—An update, *Geological Society Guidebook, New Mexico: Albuquerque Geology*, v. 50, p. 189–200
- Peterson, C., and Roy, M., 2005, Gravity and Flexure Models of the San Luis, Albuquerque, and Tularosa Basins in the Rio Grande rift, New Mexico, and Southern Colorado: *New Mexico Geological Society, 56<sup>th</sup> Field Conference Guidebook, Geology of the Chama Basin*, p. 105-114.
- Pierce, K. L., 1979, History and dynamics of glaciation in the Northern Yellowstone National Park area. *US Geological Survey Professional Paper*, 729-F.

- Pierce, K.L., 2003, Pleistocene glaciations of the Rocky Mountains: Developments in Quaternary Sciences, v. 1., p. 63-76, doi.org/10.1016/S1571-0866(03)01004-2
- Refsnider, K. A., Brugger, K. A., Leonard, E. M., McCalpin, J. P. & Armstrong, P. P., 2009, Last Glacial Maximum equilibrium-line altitude trends and precipitation patterns in the Sangre de Cristo Mountains, southern Colorado, USA: *Boreas*, v. 38, p. 663–678, doi:10.1111/j.1502-3885.2009.00097.x. ISSN 0300-9483.
- Ricketts, J. W., Kelley, S. A., Karlstrom, K. E., Schmandt, B., Donahue, M. S., & van Wijk, J., 2016, Synchronous opening of the Rio Grande rift along its entire length at 25–10 Ma supported by apatite (U-Th)/He and fission-track thermochronology, and evaluation of possible driving mechanisms. *GSA Bulletin*, v. 128(3–4), p. 397–424. <https://doi.org/10.1130/B31223.1>
- Rounce, D. R., Hock, R., Maussion, F., Hugonnet, R., Kochtitzky, W., Huss, M., Berthier, E., Brinkerhoff, D., Compagno, L., Copland, L., Farinotti, D., Menounos, B., and McNabb, R., 2023, Global glacier change in the 21st century: Every increase in temperature matters: *Science*, v. 379, p. 78-83, doi: 10.1126/science.abo1324
- Ruleman, C.A., and Brandt, T.R., 2021, Surficial geology of the northern San Luis Valley, Saguache, Fremont, Custer, Alamosa, Rio Grande, Conejos, and Costilla Counties, Colorado: U.S. Geological Survey Scientific Investigations Map 3475, 2 sheets, scale 1:75,000, <https://doi.org/10.3133/sim3475>.
- Ruleman, C., and Machette, M., 2007, An overview of the Sangre de Cristo fault system and new insights to interactions between Quaternary faults in the northern Rio Grande rift, in Machette, M.N., Coates, M.M., and Johnson, M.L., eds., 2007 Rocky Mountain Section Friends of the Pleistocene field trip—Quaternary geology of the San Luis Basin of Colorado and New Mexico, September 7–9, 2007: U.S. Geological Survey Open-File Report 2007-1193, p. 187–197.
- Sadler, P. M., 1981, Sediment Accumulation Rates and the Completeness of Stratigraphic Sections: *Journal of Geology*, v. 89, <https://doi.org/10.1086/628623>
- Schwanghart, W., Scherler, D., 2014, TopoToolbox 2 – MATLAB-based software for topographic analysis and modeling in Earth surface sciences. *Earth Surface Dynamics*, 2, 1-7. doi: 10.5194/esurf-2-1-2014
- Schweinsberg, A.D., Shroba, R. R., Licciardi, J. M., Leonard, E. M., Brugger, K.A., and Russel, C. M., 2016, Pinedale glacial history of the upper Arkansas River valley: New moraine chronologies, modeling results, and geologic mapping. *Geological Society of America Field Guide*, v. 44. P. 335-353
- Sepulchre, P., Ramstein, G., Fluteau, F., Schuster, M., Tiercelin, J.J. and Brunet, M., 2006. Tectonic uplift and Eastern Africa aridification. *Science*, v. 313(5792), p. 1419-1423.

- Shilling, D. H., Hollin, J. T., 1981. Numerical reconstructions of valley glaciers and small ice caps. In: Denton, G.H., Hughes, T.J. (Eds.), *The Last Great Ice Sheets*. Wiley, New York, p. 207–220.
- Small, E. E., and Anderson, R. S., 1998, Pleistocene relief productions in Laramide mountain ranges, western United States: *Geology*, v. 26, p. 123-126, [https://doi.org/10.1130/0091-7613\(1998\)026<0123:PRPILM>2.3.CO;2](https://doi.org/10.1130/0091-7613(1998)026<0123:PRPILM>2.3.CO;2)
- Stern, T.A., Baxter, A.K. and Barrett, P.J., 2005. Isostatic rebound due to glacial erosion within the Transantarctic Mountains. *Geology*, v. 33(3), p. 221-224.
- Strecker, M.R., Alonso, R.N., Bookhagen, B., Carrapa, B., Hilley, G.E., Sobel, E.R. and Trauth, M.H., 2007, Tectonics and climate of the southern central Andes. *Annu. Rev. Earth Planet. Sci.*, v. 35, p.747-787.
- Tada, R., Zheng, H. and Clift, P.D., 2016, Evolution and variability of the Asian monsoon and its potential linkage with uplift of the Himalaya and Tibetan Plateau: *Progress in Earth and Planetary Science*, v. 3, pp.1-26.
- Thompson, R.A., Shroba, R.R., Machette, M.N., Fridrich, C.J., Brandt, T.R., and Cosca, M.A., 2015, Geologic map of the Alamosa 30' x 60' quadrangle, south-central Colorado: U.S. Geological Survey Scientific Investigations Map 3342, 23p. scale 1:100,000, <http://dx.doi.org/10.3133/sim3342>
- Tulenko, J. P., Caffee, W., Schweinsberg, A. D., Briner, J. P., and Leonard, E. M., 2020, Delayed and rapid deglaciation of alpine valleys in the Sawatch Range, southern Rocky Mountains, USA, *Geochronology*, 2, 245–255, <https://doi.org/10.5194/gchron-2-245>
- U.S. Geological Survey, 2023, Latest Earthquakes: U.S. Geological Survey database, accessed June 20, 2023, at <https://earthquake.usgs.gov/earthquakes/map/>
- van Wijk, J., Koning, D., Axen, G., Coblenz, D., Gragg, E., & Sion, B., 2018, Tectonic subsidence, geoid analysis, and the Miocene-Pliocene unconformity in the Rio Grande rift, southwestern United States: Implications for mantle upwelling as a driving force for rift opening. *Geosphere*, v. 14(2), p. 684–709. <https://doi.org/10.1130/GES01522.1>
- Vernant, P., Hivert, F., Chery, J., Steer, P., Cattin, R., and Rigo, A., 2013, Erosion-induced isostatic rebound triggers extension in low convergent mountain ranges: *Geology*, v. 41, p. 467-470, doi:10.1130/G33942.1
- Wallace, A. R., 2004, Evolution of the southeastern San Luis Basin margin and the Culebra embayment, Rio Grande rift, southern Colorado. *Geology of the Taos Region*, p. 181–192. <https://doi.org/10.56577/FFC-55.181>
- Watkins, T. A., 1996, *Geology of the northeastern San Luis Basin, Saguache County, Colorado*. Geological Society of America, Field Trip Guide.

- Watts, A. B., 2001, *Isostasy and Flexure of the Lithosphere*, Cambridge, UK, Cambridge University Press.
- Weil, A.B. and Yonkee, A., 2022. The Laramide orogeny: Current understanding of the structural style, timing, and spatial distribution of the classic foreland thick-skinned tectonic system. In *Laurentia: Turning Points in the Evolution of a Continent*. Geological Society of America.
- Whipple, K.X., 2009. The influence of climate on the tectonic evolution of mountain belts. *Nature geoscience*, v. 2(2), p.97-104.
- Whipple, K.X., and Tucker, G.E., 1999, Dynamics of the stream-power river incision model: Implications for height limits of mountain ranges, landscape response timescales, and research needs: *Journal of Geophysical Research: Solid Earth*, v. 104, p. 17661–17674, doi:10.1029/1999JB900120.
- Whipple, K.X., Hancock, G.S., and Anderson, R.S., 2000, River incision into bedrock: Mechanics and relative efficacy of plucking, abrasion and cavitation: *Geological Society of America Bulletin*, p. 18.
- Widmann, B.L., Kirkham, R.M., and Rogers, W.P., 1998, Preliminary Quaternary fault and fold map and database of Colorado: Colorado Geological Survey Open-File Report 98-8, 331 p., 1 pl., scale 1:500,000.
- Willett, S.D., 1999, Orogeny and orography: The effects of erosion on the structure of mountain belts. *Journal of Geophysical Research: Solid Earth*, v. 104(B12), pp.28957-28981.
- Wobus, C., Whipple, K.X., Kirby, E., Snyder, N., Johnson, J., Spyropolou, K., Crosby, B., and Sheehan, D., 2006, Tectonics from topography: Procedures, promise, and pitfalls, in *Tectonics, Climate, and Landscape Evolution*, Geological Society of America, doi:10.1130/2006.2398(04).
- Zhisheng, A., Kutzbach, J.E., Prell, W.L. and Porter, S.C., 2001, Evolution of Asian monsoons and phased uplift of the Himalaya–Tibetan plateau since Late Miocene times: *Nature*, v. 411(6833), p.62-66.

## Appendix A: Supplementary Figures

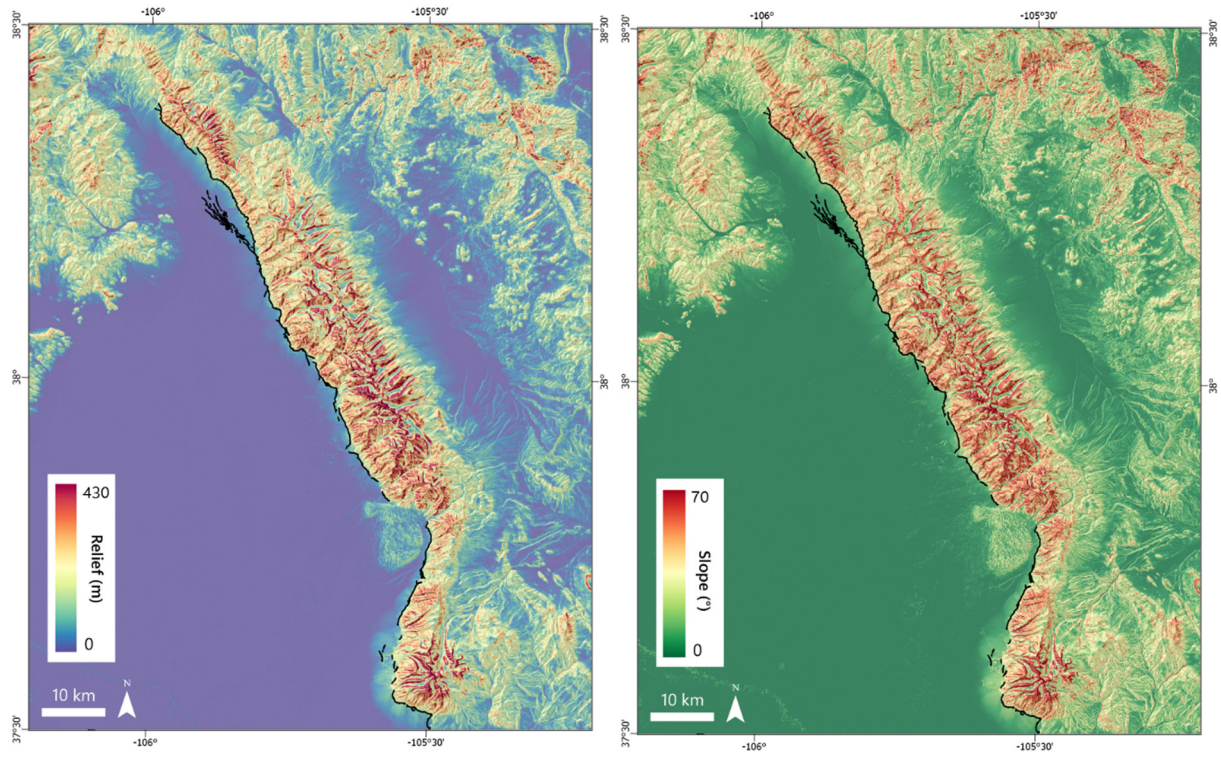


Figure S1. Relief map (left) and slope map (right) of the northern Sangre de Cristo study area. Sangre de Cristo fault indicated in black line along range front.

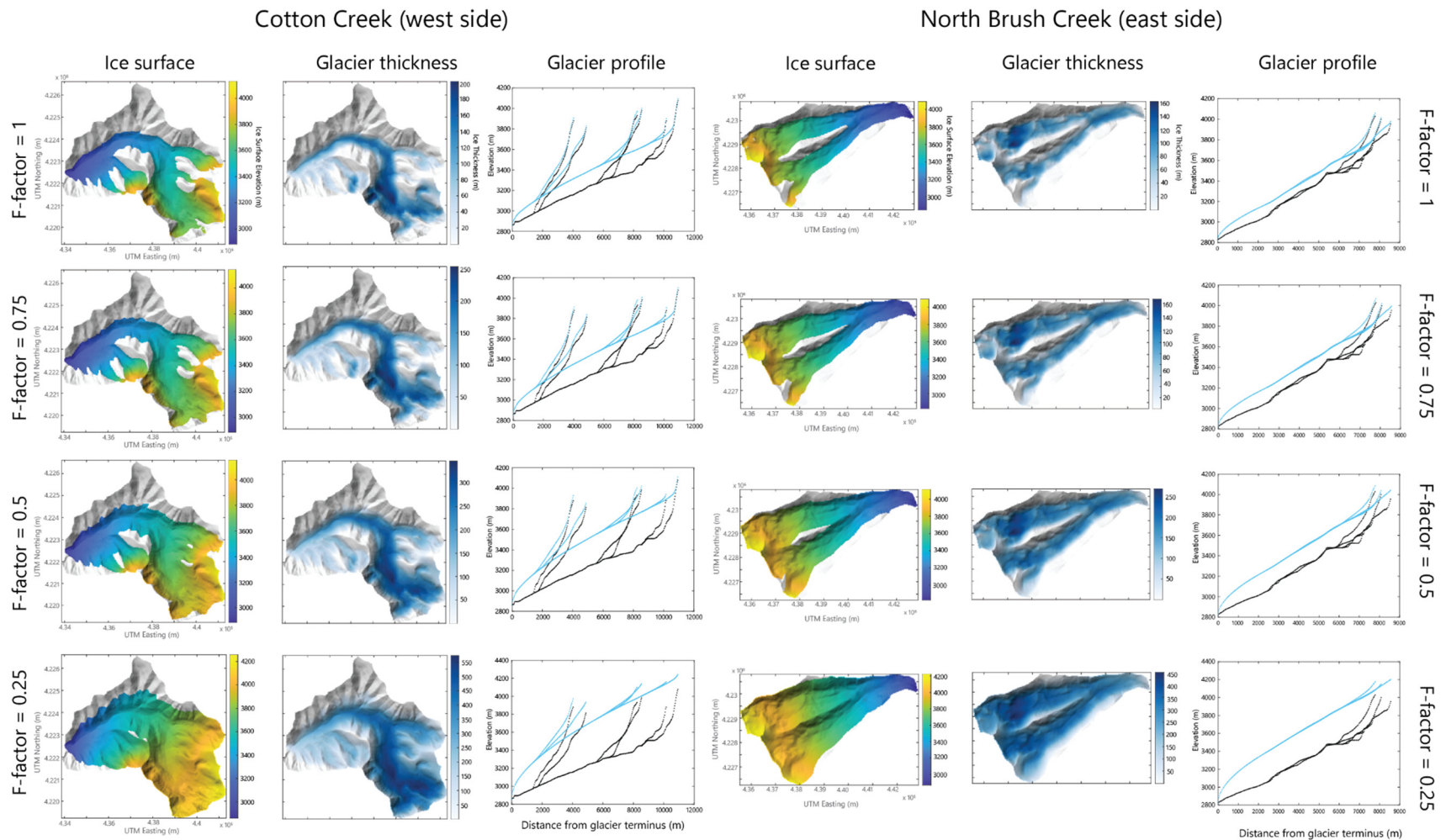


Figure S2. F-Factor rationale figure. F-factor decreases from top to bottom. Left example is reconstruction on Cotton Creek, right example is reconstruction on North Brush Creek. Glacier elevations shown in the left columns, glacier thicknesses shown in middle columns, and profile reconstructions with blue lines indicating glacier elevation and black lines indicating modern topography in right columns.

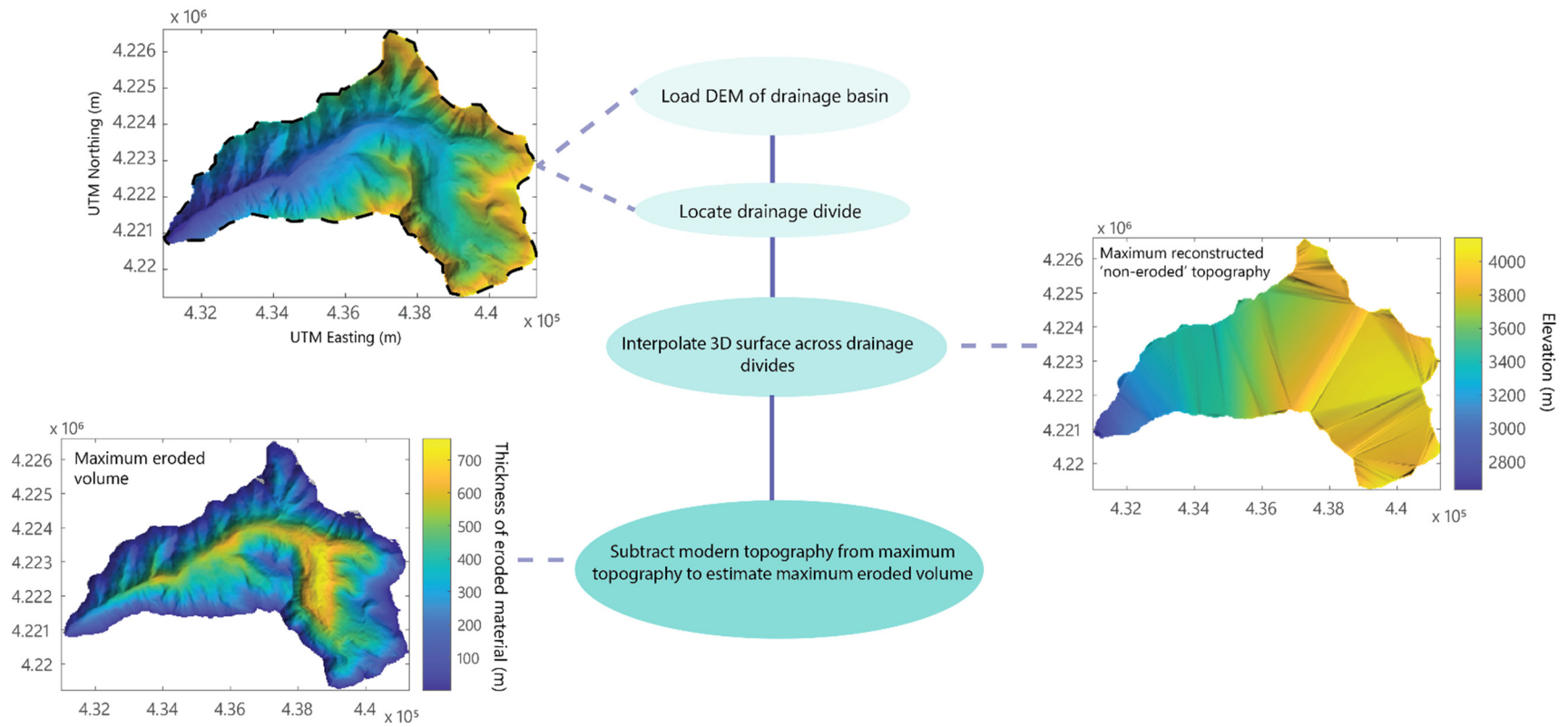


Figure S3. Maximum erosional load reconstruction and volume calculation process flowchart, using an interpolation across the drainage divide to estimate the ‘non-eroded’ volume within each catchment.

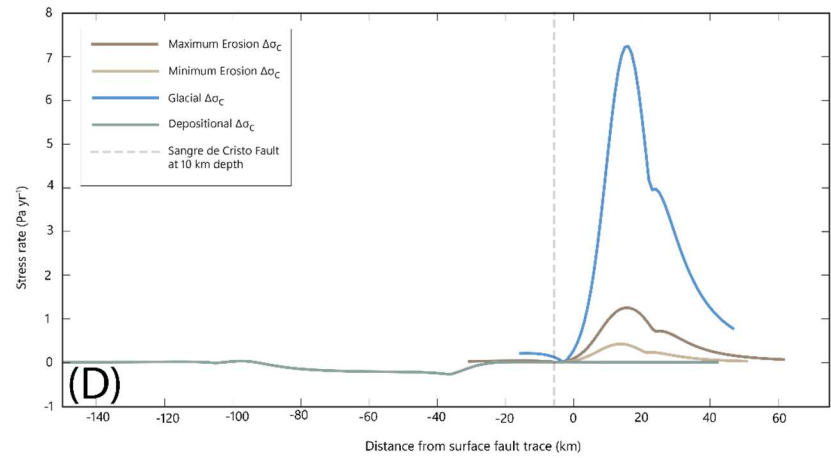
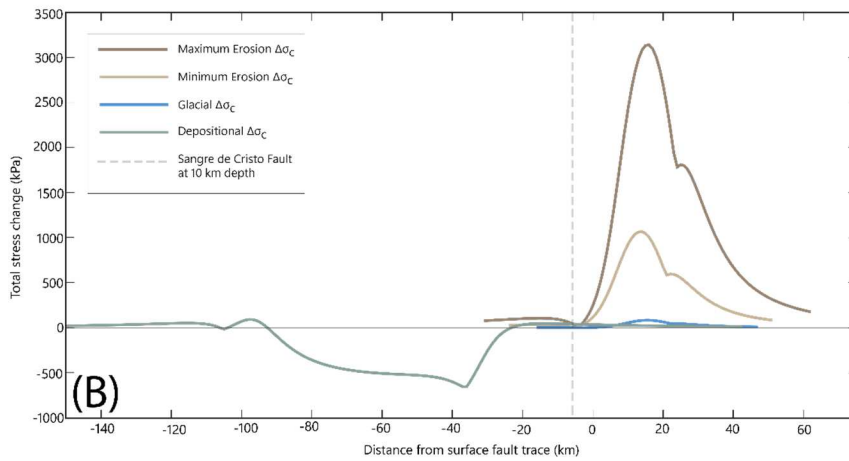
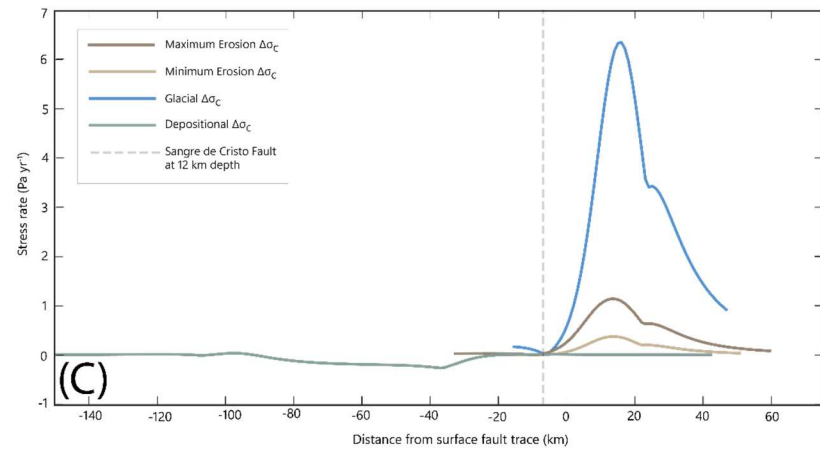
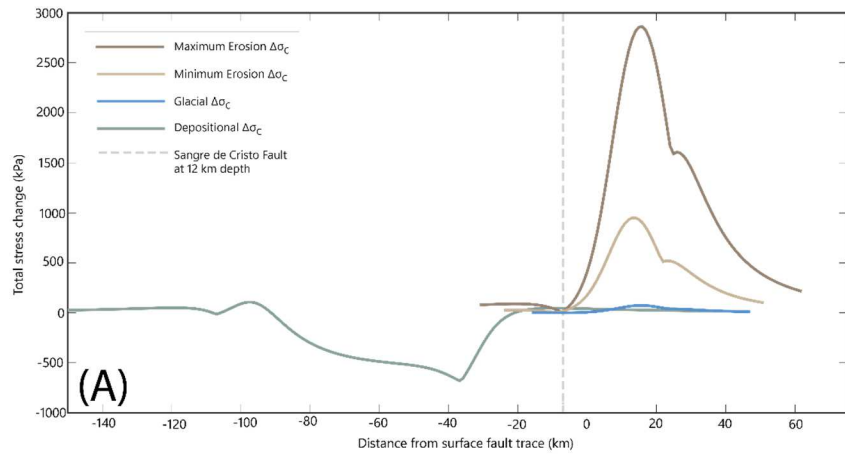


Figure S4. Stress changes for 12 km fault depth (A) and 10 km fault depth (B) based on average eroded material depicted in Figure 21A. (C) Stress rates for 12 km fault depth (C) and 10 km fault depth (D). See Figure 21 for stress changes and rates for 8 km fault depth.